Emerging Colors for Optical Coherence Tomography

By

JUN ZHU
DISSERTATION

Submitted in partial satisfaction of the requirements for the degree of

DOCTOR OF PHILOSOPHY

in

Biomedical Engineering

in the

OFFICE OF GRADUATE STUDIES

of the

UNIVERSITY OF CALIFORNIA

DAVIS

Approved:

Vivek J. Srinivasan, Chair

Jinyi Qi

Lee-Way Jin

Committee in Charge

2022

Abstract

Optical Coherence Tomography (OCT) is a depth-resolved, interferometric technique that enables micron resolution, label-free imaging *in vivo*. OCT is a standard of care in ophthalmology, but has also had an impact in cardiology as well as a number of emerging areas. In OCT, a broadband spectrum facilitates optical depth sectioning by providing a coherence gate. At the same time, this broadband spectrum also provides the ability to decode tissue chromophore content from the differential signal attenuation versus depth. Typically, OCT is performed between 700 nm and 1600 nm. In this thesis, new and emerging OCT "colors," or wavelength ranges, are investigated through a series of demonstrative studies in mice and rats. The introduction describes relevant considerations for selecting the appropriate OCT color. In the visible light range (Chapter 2), which benefits from high hemoglobin absorption, a novel way of estimating vessel hemoglobin and saturation was proposed. In the 1300 nm optical window (Chapter 3), light-blood cell interaction was investigated in the retina to understand the contrast mechanisms of OCT angiography in the retina. Finally, two emerging colors for OCT were investigated *in vivo*. In the 1700 nm optical window (Chapter 4), benefitting from minimal overall ballistic light attenuation, cellular resolution deep brain imaging was achieved. In the 2200 nm optical window (Chapter 5), benefitting from even lower scattering and low attenuation in water-scarce tissues, non-invasive *in vivo* imaging of the brain was achieved for the first time. Conclusions are summarized and future directions are discussed in Chapter 6.

Acknowledgements

In retrospect, it has been a great journey for me to study abroad and join a professional lab to learn to be an independent researcher. First, I would like to express my deepest thanks to my PhD advisor, Professor Vivek Srinivasan, for his mentorship and continuous support to me through the journey. With his extraordinary guidance, I have learnt to analyze and figure out scientific questions critically and systemically. There were tough moments when I felt disoriented, and he inspired me with his optimism to face challenges, wisdom to solve problems, and consistent enthusiasm for science. His passion, creativity, and intelligence always motivate the lab to step forward. If I am an advisor in the future, then I will aim to, and hopefully I can do as well as him! I would also like to thank my dissertation committee members, Professor Jinyi Qi and Professor Lee-Way Jin. I appreciate their valuable suggestions, discussions, and insights into my projects.

Next, I would like to thank both the past and current lab members. I am grateful to be part of the lab where the lab members have created a collaborative and diverse environment. Specifically, I want to thank Dr. Shau Poh Chong, for giving me the initial step-by-step trainings on optical system alignment. The skills and experience I obtained from him accompany me when I touch the optical system. I also want to thank Dr. Conrad Merkle, for teaching me the animal experiments. Whenever I felt stressed during animal experiments, I would think of his operating procedures and ways of dealing with issues. Thanks to Mr. Marcel Bernucci, also for trainings on animal experiments, and generous help when I needed during experiments and as a lab safety manager. Thanks to Dr. Wenjun Zhou, for discussions on system control and fiber optics. Thanks to Dr. Oybek Kholiqov, for beam walking training to me and general support. Thanks to Dr. Tingwei Zhang, for LabVIEW coding and system alignment help. Thanks to Mr. Aaron Kho, my nice same-year buddy, for studying, struggling, making progress, and sharing experiences with me. Thanks to undergraduate interns in the lab, for giving me chances to have mentoring skills. Thanks to other new lab members in NYU for general help. Besides working in the lab, I would also like to thank the lab

members for making my life experience more abundant. With them, I learnt driving skills, unlocked delicious food in Davis, visited hiking places nearby, experienced US family events… These days will never fade.

I want to thank two groups in which I was involved, BESA and the UC Davis Optics Club. I am grateful to have chances to participate in events, promote activities on club social media, develop professional skills, and having fun in the group. I also want to thank BME and COE staff for their general help and work.

During my days in Davis, I have received numerous help and support in life, so I want to thank all my lovely friends. I received guidance to settle down quickly, got help when moving in and out, and viewed beautiful landscapes and spent meaningful days with friends' companion.

Finally, I want to say thanks to my whole family, for their unconditional and endless love and support. I want to thank my beloved parents, who devote both their physical and mental energy to me, so I can be where I am today. I want to continue my journey with them. Lastly, I want to thank myself, for being stronger than yesterday.

Table of Contents

Chapter 1 Introduction

1.1. Introduction

Optical coherence tomography (OCT) is an imaging technique which provides micron-scale tomographic cross-sectional views of tissue both *in vitro* and *in vivo*[1]. With spatial scanning, volumetric tissue structural imaging can be performed[1-3]. With repeated measurements, dynamic information such as angiography[4-7], Doppler signal and blood flow[8-10], and intracellular motility[11-13] can be obtained. With a broadband light source, chromophores can be quantified[14-17]. As a powerful tool to decode tissue information, OCT has been applied widely in ophthalmology, gastroenterology, cancer biology, neuroscience, and other areas. Though OCT is traditionally performed between 700 and 1600 nm, new and emerging visible and infrared wavelength bands have recently become accessible. These emerging bands will be explored in this thesis. In this chapter, we will discuss OCT techniques and principles to select OCT wavelength range or color.

1.2. Optical Coherence Tomography Techniques

Similar to ultrasound (US), OCT measures the light reflected back from the sample. Reflectivity of each layer in the sample generates the OCT image contrast. Different from US which measures time delay of the reflected sound wave directly, OCT differentiates time delay of reflected light wave from each layer indirectly by low-coherence interferometry. Using a fiber-based spectral domain (SD) setup as an example, a typical OCT layout is shown in **Figure 1-1**. The low temporal coherence of the light source helps to achieve micron-level axial resolution. Generally, the broadband source is split into two arms, termed as sample and reference arms. Then by recombining the light reflected from the reference, and light backscattered from the sample, the interference pattern of the whole imaging depth is recorded either simultaneously over the spectral band with a spectrometer (SDOCT), or sequentially through the spectral band with a detector (Swept source OCT, abbreviated as SSOCT). For time domain OCT (TDOCT), the recombined low-coherence light from the reference and sample is detected by a single detector, so interference happens only when optical path length difference is within the coherence length, therefore it

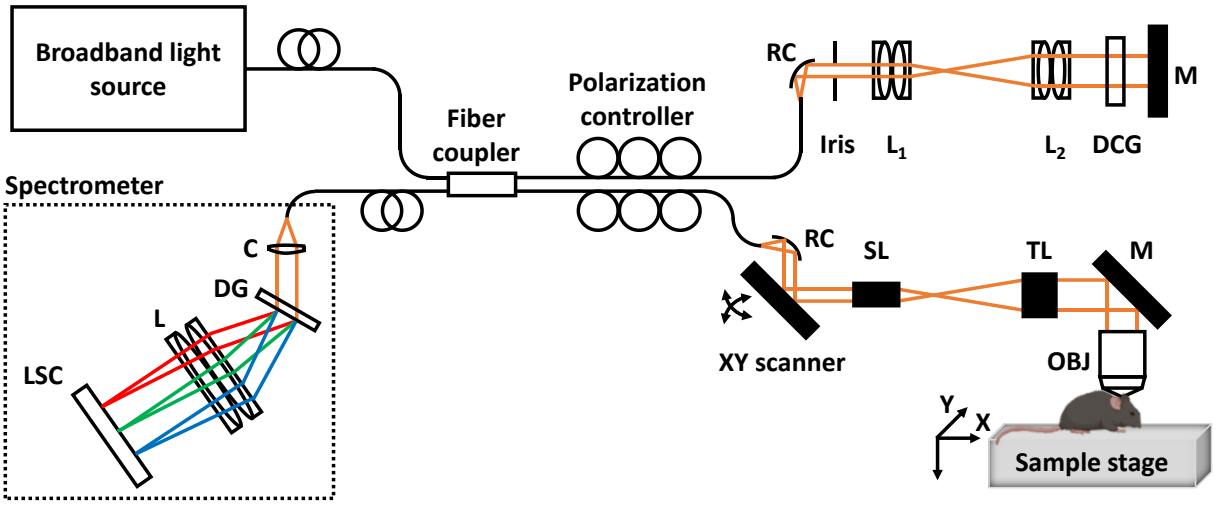

Figure 1-1. OCT system setup. A broadband light source is split into the reference and sample arms. Then the recombined light from two arms is detected by a spectrometer. RC: reflective collimator. $L_{1/2}$: lens. DCG: dispersion compensation glass. M: mirror. SL/TL: scan/tube lens. OBJ: objective. C: collimator. DG: diffraction grating. L: lens. LSC: line scan camera.

requires additional axial scanning of the reference mirror to selectively image specific depths in the sample.

Overall, the detected spectrum is:

$$I(k) = |E_R(k) + E_S(k)|^2 = |E_R(k)|^2 + 2\mathrm{Re}\{E_R(k)E_S^*(k)\} + |E_S(k)|^2, \tag{1.1}$$

where E_R and E_S are the reference and sample arm fields in phasor form, respectively, and k is the medium wavenumber. We assume that the incident field is defined as:

$$E_i(k) = s(k), \tag{1.2}$$

where $s(k)$ is the complex field spectral amplitude[18]. Then the interference term becomes:

$$\begin{aligned} I_{Interf}(k) &= 2\mathrm{Re}\{E_i(k)\sqrt{R_R}e^{i2kz_R}E_i^*(k)\sum_{n=1}^{N}\sqrt{R_{Sn}}e^{-i2kz_{Sn}}e^{i\Phi_n(k)}\} \\ &= 2\mathrm{Re}\{S(k)e^{i2kz_R}\sqrt{R_R}\sum_{n=1}^{N}\sqrt{R_{Sn}}e^{-i2kz_{Sn}}e^{i\Phi_n(k)}\} \\ &= 2S(k)\sum_{n=1}^{N}\sqrt{R_R R_{Sn}}\cos[2k\Delta z_n + \Phi_n(k)]. \end{aligned} \tag{1.3}$$

$S(k) = |s(k)|^2$ is the intensity spectrum[18]. R_R and R_{Sn} denote the reference and sample intensity reflectivity, respectively. Δz_n is the reference and sample depth difference $(z_R - z_{Sn})$, and the factor of 2 accounts for light double pass. The term $\emptyset_n$ contains higher order dispersive terms[19]. Also note that here,

the sample is assumed to consist of discrete backscatterers where R_{Sn}, the backscattering or reflectivity coefficient of each scatterer, is the desired OCT imaging contrast. To extract R_{Sn}, the inverse Fourier transform is performed on the interferogram. Assuming a Gaussian spectrum $S(k)$ is used[18] with an inverse Fourier transform of $\gamma(z)$, and assuming dispersion is compensated so $\emptyset_n(k) = \emptyset_{n0}$, then:

$$\begin{aligned} i(z) &= \gamma(z) \otimes \sum_{n=1}^{N} \sqrt{R_R R_{Sn}} [\delta(z + 2\Delta z_n) e^{i\phi_{n0}} + \delta(z - 2\Delta z_n) e^{-i\phi_{n0}}], \\ S(k) &= \frac{2\sqrt{\pi}}{\Delta k} e^{-[\frac{k-k_0}{\Delta k}]^2}, \\ \gamma(z) &= e^{-z^2 \Delta k^2 / 4}. \end{aligned} \tag{1.4}$$

Note that k_0 is the central source wavenumber, and Δk is the $1/e$ spectral half width. $\otimes$ represents convolution, so:

$$i(z) = \sum_{n=1}^{N} \sqrt{R_R R_{Sn}} [\gamma(z + 2\Delta z_n) e^{i\phi_{n0}} + \gamma(z - 2\Delta z_n) e^{-i\phi_{n0}}]. \tag{1.5}$$

Now R_{Sn} is extracted, albeit with the broadening or blurring by function $\gamma(z)$. In addition, the expression shifts each layer n by twice the distance from the reference position, $2\Delta z_n$, due to round-trip measurement of the optical path. The OCT axial resolution (δz) is defined as the FWHM of $\gamma(2z)$, i.e. the coherence function modified for single pass z. The axial resolution is half of the coherence length (l_c):

$$\delta z = \frac{1}{2} l_c = \frac{2\sqrt{\ln(2)}}{\Delta k} = \frac{2\ln(2)}{\pi} \frac{\lambda_0^2}{\Delta \lambda}. \tag{1.6}$$

λ_0 is the central wavelength corresponding to k_0, and $\Delta\lambda$ is the spectrum full-with-half-maximum (FWHM). Note that a refractive index of 1 has been assumed, corresponding to free space. In practice, for SDOCT, the CCD or CMOS array detector samples the interferogram, and the sampling density or spectral resolution is limited by the number of pixel number (N) and spectral range. To satisfy the Nyquist sampling theory, then the oscillation period of **Equation (1.3)** should be larger than twice the sampling period (δk_s):

$$\frac{2\pi}{2\Delta z_n} \geq 2\delta k_s. \tag{1.7}$$

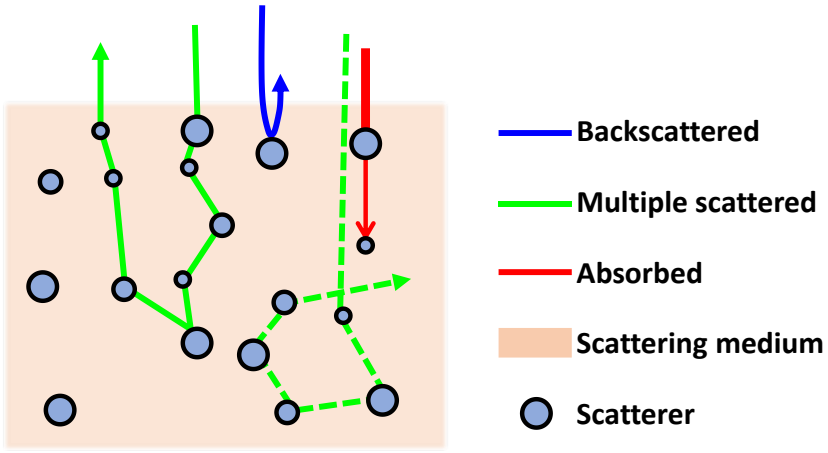

Figure 1-2. Light tissue interactions. When an OCT beam impinges on a scattering medium, some of the photons are singly backscattered (blue), these carry spatial information and reach the detector; most of the photons are multiply scattered or get absorbed during the scattering path, and do not reach the detector (green dash); some multiply scattered photons (green) lose part of the spatial information but can still reach the detector; the remaining photons are absorbed on the light path (red) and they cannot reach the detector.

Therefore,

$$\Delta z_{\max} = \frac{\pi}{2\delta k_s}. \tag{1.8}$$

Again, assuming a refractive index of 1, δk_s is given by:

$$\delta k_s = \frac{2\pi}{\lambda_0^2}\delta\lambda = \frac{2\pi}{\lambda_0^2}\frac{2\Delta\lambda}{N}. \tag{1.9}$$

1.3. OCT Color Selection Considerations

1.3.1. Axial Resolution

As shown in **Equation (1.6)**, OCT axial resolution is proportional to the central wavelength squared and is inversely proportional to the spectral bandwidth. Therefore, to achieve a similar axial resolution to visible light, a much broader bandwidth is needed for the near-infrared (NIR) wavelength range. However, problems of dispersion arise with a broad spectrum. In the visible light range, with high axial resolution, fine structures in retina[20-24], rodent/human brain[25-27], and mouse superficial skin[14] have been visualized. The confocal gate of a tightly focused beam can further improve the axial resolution[16,28], however, such a setup will require correction of aberration.

1.3.2. Tissue Optical Properties

Tissue interacts with the incident beam through scattering and absorption (**Figure 1-2**). The main source of the OCT signal is backscattered photons (blue path in **Figure 1-2**) that travel to and back from the coherence volume. Backscattered photons provide information about local tissue backscattering properties. However, most photons are scattered and do not reach the detector (green dash in **Figure 1-2**). A portion of multiply scattered photons that deviate from the original traveling path and lose some spatial specificity (green path in **Figure 1-2**) may still reach the detector. The contribution of detected multiply scattered photons blurs the OCT image. Photons that get absorbed directly (red path in **Figure 1-2**) or scattered at large angles cannot reach the detector and therefore do not contribute to the OCT signal. Scattering and absorption attenuate the OCT signal by reducing the number of purely backscattered photons. Ballistic attenuation ($\mu_{bal,t}$) is defined as:

$$\mu_{bal,t}(\lambda) = \mu_s(\lambda) + \sum_i f_i \mu_{a,i}(\lambda), \tag{1.10}$$

where μ_s is the scattering coefficient, f_i is the volume fraction of chromophore i and μ_a is the absorption coefficient. Note that experimentally, the total tissue ballistic attenuation coefficient ($\mu_{bal,t}$) is not equivalent to the OCT signal decay slope (μ_t) due to detection of multiply scattered light. To differentiate from the above attenuation model, the experimental attenuation is:

$$\mu_t(\lambda) = \mu_{t,s}(\lambda) + \sum_i f_i \mu_{a,i}(\lambda), \tag{1.11}$$

where $\mu_{bal,t}$ is replaced by $\mu_{t,s}$, which is the effective attenuation accounting for multiple scattering effects[29]. Depending on the tissue scattering and absorption properties, OCT spectral range can be chosen. For instance, as shown in **Figure 1-3** (data references: water absorption[30], lipid absorption[31], hemoglobin absorption[32], and scattering[33]), hemoglobin is typically measured in the visible light range where its absorption is relatively higher than in the NIR range[17,34-36], while lipid is measured in the NIR range where its absorption peaks[16,37].

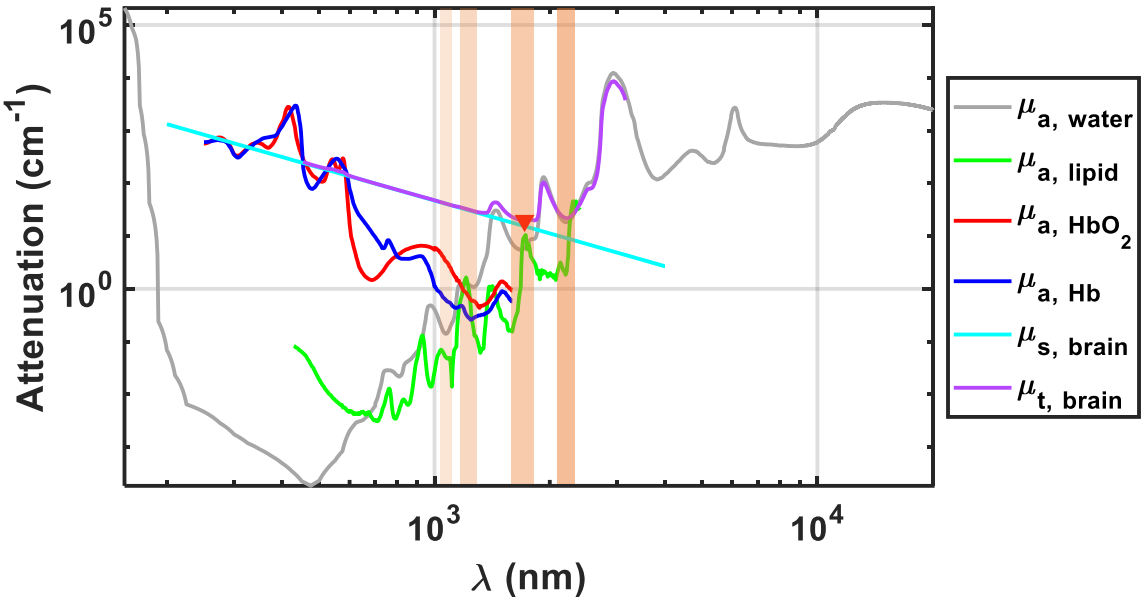

Figure 1-3. Tissue attenuation due to water absorption (gray), lipid absorption (green), oxyhemoglobin absorption (red), deoxyhemoglobin absorption (blue), and scattering (cyan). For mouse brain, total attenuation (magenta) is minimized at around 1700 nm (red triangle). Orange shaded regions represent NIR optical windows centered at 1050, 1300, 1700, and 2200 nm.

1.3.3. Penetration Depth

Optical properties also determine the penetration depth into the tissue. As shown in **Figure 1-3**, tissue scattering generally decreases with wavelength, while chromophore absorption has peaks and valleys as wavelength changes. Moreover optical components and detector technologies differ according to wavelength range. Therefore, researchers typically divide the spectrum into optical windows for tissue imaging. In the visible light and short NIR range, where tissue scattering and hemoglobin absorption dominate, small thickness samples are typically imaged, such as retina and *ex vivo* slices[22,38,39]. In the NIR range, where water absorption increases substantially, deep tissue imaging is typically performed in optical windows[33,40,41] centered at 1050 nm, 1300 nm and 1700 nm where water absorption (and tissue absorption, given that tissue water content is generally larger than 70%[42]) is locally minimized. 2200 nm is the fourth NIR window, where tissue scattering decreases further and water absorption is also locally minimized. It might be the longest wavelength NIR window suitable for tissue imaging[43], if possible, because water absorption is orders-of-magnitude higher beyond it (**Figure 1-3**).

1.3.4. Technical/Engineering Challenges

On top of the needs of OCT imaging, such as desirable resolution and tissue property quantification, technical limitations set the boundary of colors that can be employed. Note that implementation of OCT in one wavelength range is not simply transferrable to another wavelength range[44]. The light source, detector, and other components have to be carefully optimized for the target wavelength range. For instance, longer NIR imaging which employs the third (centered at 1700 nm) or fourth (centered at 2200 nm) optical window, or the mid-IR range is much limited by system sensitivity due to lack of high-performance components[16,43,45]. As an example, typically the 1700 nm window is used partially due to the cutoff of InGaAs detector[37], therefore, the system sensitivity, spectral range and consequent axial resolution are limited.

1.4. OCT Colors

1.4.1. Established Colors for *In Vivo* Imaging: Visible Light Range

Visible light range is attractive due to high axial resolution and the hemoglobin absorption contrast.

The first visible light OCT demonstrated by Považay et al.[46] in 2002 achieved an axial resolution of ~0.9 μm in air. This ultrahigh resolution was made possible by employing a photonic crystal fiber based light source. Once commercial supercontinuum (SC) sources became more widely available, a number of groups applied visible light OCT to image fine tissue structures *in vivo* and obtain chromophore information[14,15,47,48]. Typical spectroscopic OCT is performed by windowed Fourier transform (WFT) or short time Fourier transform (STFT) to get spectral information at different depths, therefore, there are always tradeoffs between depth and spectral resolution[49,50]. To potentially resolve this, Robles et al.[14,47,48] proposed the dual window (DW) method which incorporates two complementary spectral windows of different sizes. Spectral and spatial information obtained with the two different windows were combined to generate the final structural and spectroscopic images. As approaches such as noise reduction and reference normalization were introduced, the WFT method remains popular when performing spectroscopic OCT. Yi

et al. quantified microvessel oxygen saturation (sO_2) in the rat retina[15] and mouse skin[51] by fitting the OCT signal from the vessel bottom wall which double-passed the vessel lumen. They also validated the results through hypoxia and hyperoxia challenges. Chong et al. quantified microvessel sO_2 and hemoglobin concentration in the rat[17] and human[20] retina in cross-section, and validated their method with *ex vivo* phantom measurements. Pi et al.[35] quantified sO_2 in capillaries of the rat retina with reflections from the vessel bottom wall, and validated the results with known perfusion pathways by verifying decreasing sO_2 with arteriole branching order.

Recent progress in visible light OCT, aided in part by approaches that address chromatic dispersion[52], has revealed finer structures of retina and brain tissues. Chong et al.[20] demonstrated a fiber-based visible light OCT with less than 2 μm axial resolution. They showed high-resolution spectroscopic layered reflectance of retina; hemoglobin saturation and concentration mapping in retinal vessels are also measured. Recently, with laser-excess-noise enabled improvements in system sensitivity and resolution approaching one micron, Kho et al.[21] visualized a hyporeflective band inner to the external limiting membrane (ELM) in the mouse retina, and Zhang et al.[22] quantified inner plexiform layer (IPL) stratification in the human retina. Both of these studies were aided by speckle reduction. Alternative speckle reduction approaches have enabled high contrast imaging of both mouse and human retinas[23], and quantifying structural changes of the mouse retina after eye-opening[24]. For *ex vivo* brain imaging, using optical clearing to aid deeper penetration, Lichtenegger et al.[25,26,39] visualized pathological features such as amyloid-beta plaques and 5-aminolevulinic acid (5-ALA) positive regions in Alzheimer's disease (AD) brain tissue. In combination with improved transverse resolution by asymmetric overfilled illumination and Gaussian detection, Merkle et al.[27] imaged details of meningeal layers, the intravascular red blood cell-free layer, and myelinated axons in the mouse brain *in vivo*.

1.4.2. Established Colors for *In Vivo* Imaging: Shorter NIR Range

Shorter NIR wavelengths of 850, 1050, 1300 and 1500 nm generally penetrate deeper into the tissue than visible light and can use available high-performance off-the-shelf optical components. Deeper structures

such as the choroid[53-56], deeper dermal layers[57-59], and deep rodent cortical layers[60,61], can be visualized with shorter NIR ranges. In addition, dynamic information about blood flow[62-64] can also be obtained. Note that for human retinal imaging, 850 and 1050 nm wavelengths are more appropriate, while the 1300 nm window can only image the anterior segment (AS), not the human retina, due to higher water absorption and relatively long traveling distance through aqueous and vitreous humors in the human eye[65]. 1500 nm has been also reported for visualizing blood vessels[66] *in vivo*, and has been shown to have deeper penetration than shorter wavelengths in *ex vivo* samples[67]. However, we anticipate a shallower penetration in this window than the 1700 nm window, because water absorption at 1500 nm is not as low as at 1700 nm.

1.4.3. Emerging Color for *In Vivo* Imaging: the 1700 nm Optical Window

1700 nm optical window has been proved to be the wavelength range that attenuates minimally in the mouse brain due to lower scattering and minimized water absorption[41,68], therefore, it merits attention for deep tissue imaging. In addition, lipid has high absorption in this window[31], which facilitates plaque detection and quantification.

Early work of 1700 nm OCT focused on technical innovations in light sources and detector for this window, dating back to 2008, when Sharma et al.[69] demonstrated *in vivo* swept source OCT imaging using the 1700 nm window for the first time. They built a polygon mirror based swept source laser and used the InGaAs detector, and showed less attenuation in the 1700 nm window than the 1300 nm window. Later, Ishida et al.[70,71] implemented a broadband 1700 nm supercontinuum source generated by a normal-dispersion highly nonlinear fiber (ND-HNLF), in combination with a balanced detection using two InGaAs photodiodes, in a time domain OCT setup. They demonstrated universally lower scattering properties of the 1700 nm window in tissue by imaging multiple phantoms and *ex vivo* samples. In 2012, papers about InAs/InP(100) quantum dot waveguide photodetectors[72] and a tunable quantum dot laser[73] were published, providing alternative approaches for implementing OCT in the 1700 nm window. In 2014, Kawagoe et al.[74] developed a single-wall carbon nanotube based broadband supercontinuum source, and built a 1700 nm OCT system in time domain with balanced extended InGaAs detection. They compared tissue properties in the 1700

window and the 1300 nm window, and found higher penetration depth with the 1700 nm window in low-water-absorption samples. As an alternative approach for the light source, in 2015, Tanaka et al.[75] combined three SLDs and imaged distribution of lipids in the artery *ex vivo* with spectral domain OCT.

As commercial optical components, especially the light sources and the extended InGaAs detectors, became more readily available, recent efforts in the 1700 nm window focused on improving image resolution, getting structural and spectral information, and applications in living tissue. In 2015, Chong et al.[76] used a commercial supercontinuum light source to demonstrate spectral domain 1700 nm deep cortical and sub-cortical mouse brain imaging *in vivo* for the first time. The superior penetration depth and details visualized *in vivo* in the mouse brain achieved by this window have drawn attention for deep tissue imaging. Later, Yamanaka et al.[77] and Kawagoe et al.[78,79] demonstrated high axial resolution imaging *ex vivo* in both time and spectral domain. In 2017[37] and 2019[80], Li et al. did *ex vivo* and *in vivo* intraluminal imaging with a commercial swept source, which extended applications of the 1700 nm window for human subjects. In 2018, Park et al.[81] showed *in vivo* mouse brain sub-cortical angiography with a commercial swept source. In 2019, Yamanaka et al.[82,83] did spectral domain 1700 nm *ex vivo* imaging, with high transverse imaging. In 2021, as shown in Chapter 4 of this thesis, Zhu et al.[16] implemented a 1700 nm OCM system in spectral domain, and performed *in vivo* cortical and sub-cortical mouse brain imaging with cellular-level transverse and axial resolutions.

1.4.4. Novel Color for *In Vivo* Imaging: the 2200 nm Optical Window

2200 nm optical window has been rarely used for *in vivo* imaging, due to high water absorption, though scattering should be reduced compared to shorter wavelengths. Until recently, the 2200 nm window has been used mainly for dry paintings. In 2013, Liang et al.[45] demonstrated that the optimum spectral range for art imaging is around 2200 nm because pigments of historical arts have maximum transmission in the window. Later, Cheung et al.[84,85] showed better visualization of highly scattering painting layers with the OCT system centered at 1960 nm than at 1310 or 930 nm, aided by low water content in the painting sample. Note that the spectrum center applied in these studies is closer to 2000 nm because of the light source

design. In 2019, as shown in Chapter 5 of this thesis, Zhu et al.[43] explored potential benefits of 2200 nm window for *in vivo* imaging, for the first time. They showed rat brain superficial cortical vasculature map through the ~400 μm thick intact skull and presented water content quantification of tissue.

1.4.5. Mid IR Range

To further reduce multiple scattering to detect deep features of the sample, it is natural to move upon even longer wavelength range, the mid-IR range. Due to high water absorption, here we only consider this range for low water content or dry sample imaging. In 2007, Colley et al.[44] built a 7 μm time domain OCT system, with the quantum cascade laser (QCL) and a liquid nitrogen cooled photoconductive mercury cadmium telluride (MCT) detector. They showed images of a CaF_2 window and 3D collagen lattice. However, the system sensitivity is limited due to severe side lobes caused by discrete nature of the spectrum. In addition, detection in this range is also challenging because of the noisy thermal detectors. To alleviate problems of detection, in 2019, Israelsen et al.[86] showed a 4 μm OCT system with upconversion from the broad mid-IR range to narrower NIR range for detection. The 4 μm OCT system is superior to the 1300 nm system in terms of deep penetration and reduced multiple scattering in non-destructive testing (NDT) of dry samples. Nevertheless, sensitivity of the 4 μm OCT system is limited by the upconversion efficiency. Furthermore, a more than 1 μm broad spectrum is implemented, which might challenge the performance of optical components used in the system.

1.5. Dissertation scope

As described in the above sections, OCT color selection requires consideration of axial resolution, tissue optical contrast, imaging depth, and technical hurdles. Benefits and limitations of each window need to be investigated and understood thoroughly. In this thesis, as shown in **Table 1-1**, a range of OCT colors are investigated through a series of demonstrative studies in mice and rats. Chapters 2 and 3 aim to understand light tissue interactions within the popular OCT windows. In Chapter 2, a novel method of hemoglobin concentration and oxygen saturation quantification is explored in the visible light range, enabled by high

axial resolution and contrast. In Chapter 3, retinal vessel signal angular dependence is explored in the 1300 nm window, where attenuation by blood is smaller so scattering effects can be better visualized. Chapter 4 and 5 explore *in vivo* imaging advantages and disadvantages of emerging colors in the 1700 nm and 2200 nm windows. In Chapter 4, the 1700 nm optical window is investigated with an OCT system that covers the entire window, and consequent problems of light source noise, detector noise, chromatic dispersion and resolution-speckle tradeoff are characterized and optimized. In Chapter 5, the 2200 nm optical window is used for *in vivo* tissue imaging, for the first time.

Table 1-1. Dissertation Scope.

OCT Color	Visible light (575 nm)	1300 nm window	1700 nm window	2200 nm window
Axial resolution in tissue (field FWHM)	1.0 μm	5.2 μm	Coherence gate achieves 7.8 μm and further aided with confocal gate	14.0 μm
Structural imaging	Mouse retina	Rat retina	Mouse cortex and sub-cortex with thinned skull	Rat superficial cortex with intact skull
Sample illumination power	300 μW	1.5 mW	3.5 mW	3.5 mW
Camera linerate	30 kHz	91 kHz	47 kHz	47 kHz
Maximum sensitivity	_	92 dB	95 dB	84 dB
Total penetration depth in tissue	0.25 mm	0.8 mm	1.6 mm (<0.05 mm thinned skull + cortex + sub-cortex)	0.6 mm (0.4 mm intact skill + 0.2 mm superficial cortex)
Main contrast	Hemoglobin absorption; tissue scattering	Tissue scattering	Water and lipid absorption; tissue scattering	Water absorption; tissue scattering
Chromophore quantification	sO_2 and hemoglobin concentration	RBC signal angular dependence (no chromophores)	Water and lipid content	Water content
System cost	$75,000	$68,000	$130,000	$100,000
Potential clinical applications	Retinal pathology	Retinal pathology in small animals	Neuropathology, cardiology, dermatology	Neuropathology, bone tissue engineering

Chapter 2 *In Vivo* Autocorrelation Spectroscopy with Optical Coherence Tomography

2.1. Abstract

Spectroscopic Optical Coherence Tomography (OCT) enables measurement of depth-resolved spectra or spectral features, which can be used to directly or indirectly assess chromophore concentration *in vivo*. Since spectroscopic OCT was first demonstrated over two decades ago, studies have been based on the windowed Fourier transform. Here, we present a spectroscopic method of assessing hemoglobin in OCT which, rather than determine a depth-resolved spectrum, determines a depth-resolved autocorrelation function. All or part of this complex-valued autocorrelation function is then fit with a model that incorporates the spectral absorption characteristics of different chromophores assumed to be present in tissue. Though related to the conventional windowed Fourier transform method through the Wiener–Khinchin theorem, the proposed method does not use windowed Fourier transforms of the OCT data. Also, conveniently, the depth resolution of autocorrelation spectroscopy can be modified by adjusting the number of lags used for fitting. Furthermore, autocorrelation spectroscopy is well-suited for assessing chromophores in dynamic scattering environments such as in blood vessels *in vivo*. In this work, the new autocorrelation spectroscopy method is introduced and compared against the conventional windowed Fourier transform method in visible light OCT of the mouse retina.

2.2. Introduction

Spectroscopic Optical Coherence Tomography (OCT) enables measurement of depth-resolved spectra or spectral features[50,87,88]. In contrast to conventional absorption spectroscopy, which only operates in transmission, spectroscopic OCT can assess samples in reflectance mode, thus facilitating new applications. The original spectroscopic analysis methods assumed direct access to the depth-resolved point spread function[50,87] via a well-defined, single, spectrally-flat reflection at the distal end of the sample. Thus, the

original spectroscopic analysis methods are similar to those used in standard absorbance spectrophotometry, albeit assuming two passes through the sample.

Scattering from blood vessels, without resolvable specular reflections, precludes direct measurement of the point spread function and interference spectrum. On the contrary, the complex OCT signal in a voxel comprises multiple light reflections with different amplitudes that sum coherently with random phases. The resulting speckle pattern modulates spectral information, potentially confounding attempts at extracting absorption. Proposed solutions to this problem involve ensemble averaging over independent speckles either in space or in time[17,35]. Statistically, these approaches can be described as estimating the power spectrum, which describes the second order speckle statistics. Most, if not all, spectroscopic OCT works estimate a depth-resolved spectrum as an intermediate step in the analysis[14,47,48,89,90], which is achieved by a so-called windowed or short-time Fourier transform (though strictly, it is applied in depth). Therefore, these works are subject to an uncertainty relationship depending on the window chosen for Fourier transformation, where a finer spectral resolution and accuracy in spectral estimation is balanced against a finer depth resolution and accuracy in depth localization. Window sizes are chosen to optimize this tradeoff, depending on the application[47].

According to the Wiener-Khinchin theorem, the autocorrelation function is given by the inverse Fourier transform of the power spectrum. As such, the autocorrelation function should represent an alternative method of extracting spectroscopic information. Here we propose to estimate the complex autocorrelation function directly and fit it with a parameterized model. Though at first glance this proposal may seem similar to conventional power spectrum estimation, autocorrelation spectroscopy has the important distinction that it does not require explicit spectral estimation, and as such, does not require a windowed Fourier transform. In this pilot study, we demonstrate the feasibility of extracting spectroscopic information from the complex autocorrelation function *in vivo* in the mouse retina.

2.3. Methods and Materials

Oxygen saturation (sO_2), the fraction of oxygen-bound hemoglobin relative to total hemoglobin in the blood vessel, is a crucial physiological parameter. Due to higher absorption at short wavelengths, hemoglobin concentration can be reliably measured with visible light OCT spectroscopy. Spectroscopic OCT determines depth-resolved spectra, from which sO_2 is determined, resulting in spatial-spectral resolution tradeoffs. Here, we present a novel spectroscopy method, which uses the depth-resolved, complex-valued autocorrelation function for assessing sO_2 and hemoglobin concentration.

The spectroscopic optical coherence tomography (OCT) signal attenuation with depth is denoted as:

$$I_{Interf}(k,z) = I_{Interf}(k, z = z_0) e^{C + \frac{-2.303[sO_2 \varepsilon_{HbO_2} + (1-sO_2)\varepsilon_{Hb}]CM_{HbT}L}{MW_{Hb}}}, \quad (2.1)$$

where $I_{Interf}(k,z)$ [simplified henceforth as $I(k,z)$ if not mentioned] represents the interference spectrum (proportional to $\sqrt{I_R I_S}$) as a function of wavenumber k, at the tissue depth z. Note that I is proportional to the square root of the sample spectrum ($\sqrt{I_S}$, or the sample field amplitude). The spectrum at the top of the vessel at depth z_0, $I(k, z_0)$, changes as light travels through the blood where different wavelengths are attenuated to different degrees. CM_{HbT} is the total hemoglobin mass concentration, which has units of g/l, and ε denotes chromophore extinction coefficient with units of $l/mol/cm$. MW_{Hb} is the molecular weight of hemoglobin, which is 64500 g/mol. Hemoglobin molecular concentration, C_{HbT}, given by CM_{HbT}/MW_{Hb}, then has units of mol/l. An additional term C, accounts for the scattering effects, which are approximated as being wavelength-independent. To analyze localized spectral information, the conventional spectroscopic OCT method[17] performs a windowed Fourier transform (WFT) on the complex OCT signal $s(z)$ before fitting by **Equation (2.1)**:

$$I_w(k,z) = WFT[s(z)] = \sum_{z'} s(z') w(z' - z) e^{-i2kz'}, \quad (2.2)$$

where the width (Δz) of the windowing function $w(z)$ induces a tradeoff between the spatial (i.e., depth) and spectral resolutions.

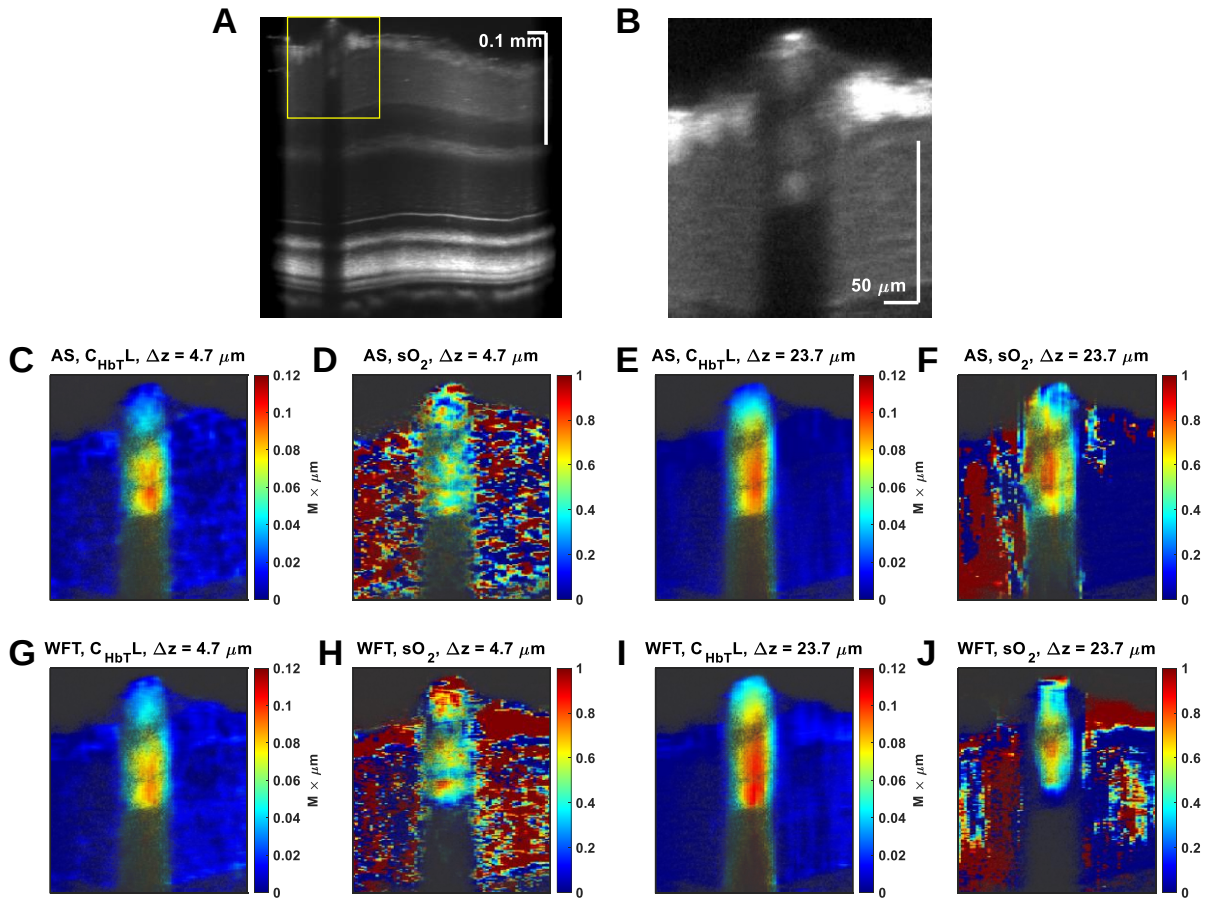

Figure 2-1. ***In vivo*** **retinal spectroscopy of a 19-month-old mouse. Amplitude image of the retina (A) with the region-of-interest (yellow box) shown in (B). Images showing estimates of of $C_{HbT}L$ and sO_2 by the autocorrelation spectroscopy (AS, C-F) and the short-time Fourier transform (STFT, G-J) methods, with different window sizes (Δz).**

The autocorrelation spectroscopy (AS) is based on the Wiener-Khinchin theorem[91], which states that the autocorrelation function $R(\zeta, z)$ of the complex OCT signal $s(z)$ and its power spectral density $|I(k,z)|^2$ are a Fourier transform pair:

$$R(\zeta, z) = \Im^{-1}[|\, I_{Interf}\,(k, z = z_0)\,|^2] * \Im^{-1}[|\, e^{C + \frac{-2.303[sO_2\varepsilon_{HbO_2} + (1-sO_2)\varepsilon_{Hb}]CM_{HbT}}{MW_{Hb}} 2L}\,|]. \qquad (2.3)$$

The spectrum attenuation, represented in the wavenumber domain as a multiplication, is thus represented in ζ as a convolution, and a fitting procedure can be applied to yield sO_2 and C_{HbT}.

A previously-described visible light OCT system[21] was employed for this study. Repeated B scans were performed across a vessel in the mouse retina. Complex OCT data was reconstructed from the raw

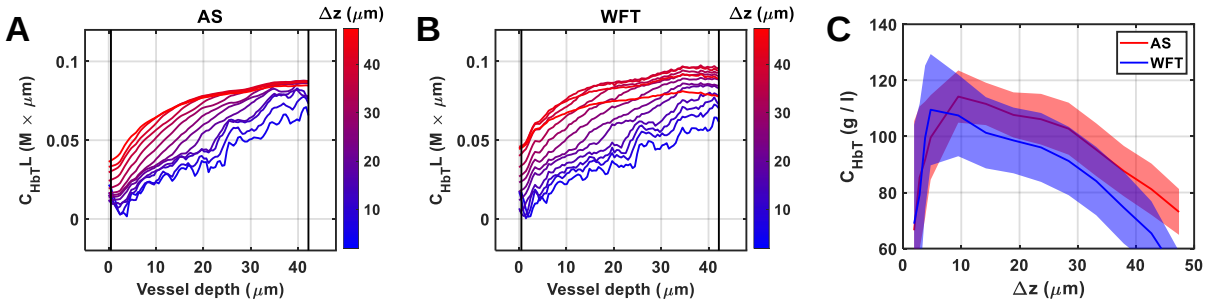

Figure 2-2. Depth-dependence of $C_{HbT}L$ (averaged transversely over 28.1 μm within the vessel) as the window size (Δz) varies, for both autocorrelation spectroscopy (AS, A) and windowed Fourier transform (WFT, B) methods. Black lines denote the vessel boundaries. (C) Estimated C_{HbT} (from the derivative of data in A-B with respect to vessel depth) for the STFT method (blue) shows a larger standard error (shaded area) than the AS method (red). Standard errors are calculated over the intravessel depth range. Note that accuracy is compromised as Δz increases in (C). Autocorrelation fitting lag range Δζ equals to Δz.

interference fringes by background subtraction, resampling, dispersion compensation, and Fourier transform. Spectrally-dependent attenuation by blood is a key source of information for hemoglobin quantification. Therefore, high-pass and low-pass filtering was performed along the temporal dimension to separate the dynamic vessel from the static tissue. The first term in **Equation (2.3)** was estimated from static tissue. Then, the complex-valued autocorrelation function was calculated in the axial direction by averaging in transverse direction (Δx = 14 μm) and in time (Δt = 1.6 s):

$$R(\zeta, z_0, x_0, t_0) = \frac{1}{\Delta t}\frac{1}{\Delta x}\frac{1}{\Delta z - \zeta}\sum_{t=t_0-\Delta t/2}^{t=t_0+\Delta t/2}\sum_{x=x_0-\Delta x/2}^{x=x_0+\Delta x/2}\sum_{z=z_0-\Delta z/2}^{z=z_0+\Delta z/2-\zeta} s^*(z,x,t)s(z+\zeta,x,t), \quad (2.4)$$

Note that averaging with width Δz in depth is also incorporated in the calculation. Before fitting the model in **Equation (2.3)**, autocorrelations are bias subtracted. The noise bias is calculated from a background region. Autocorrelation data from 8 repeated volumes with 32 consecutive B-scans (total offset of 62.5 μm) each were averaged before fitting.

2.4. Results and Conclusion

By fitting the model in **Equation (2.3)** in the ζ domain, here we show that the AS method works as an alternative approach for obtaining information about chromophores. A large superficial vessel from the mouse retina was selected (**Figure 2-1A-B**), and then was analyzed by both the AS (**Figure 2-1C-F**) and WFT (**Figure 2-1G-J**) methods. As the window size (Δz) increases from 4.7 μm (**Figure 2-1C-D**, **G-H**) to

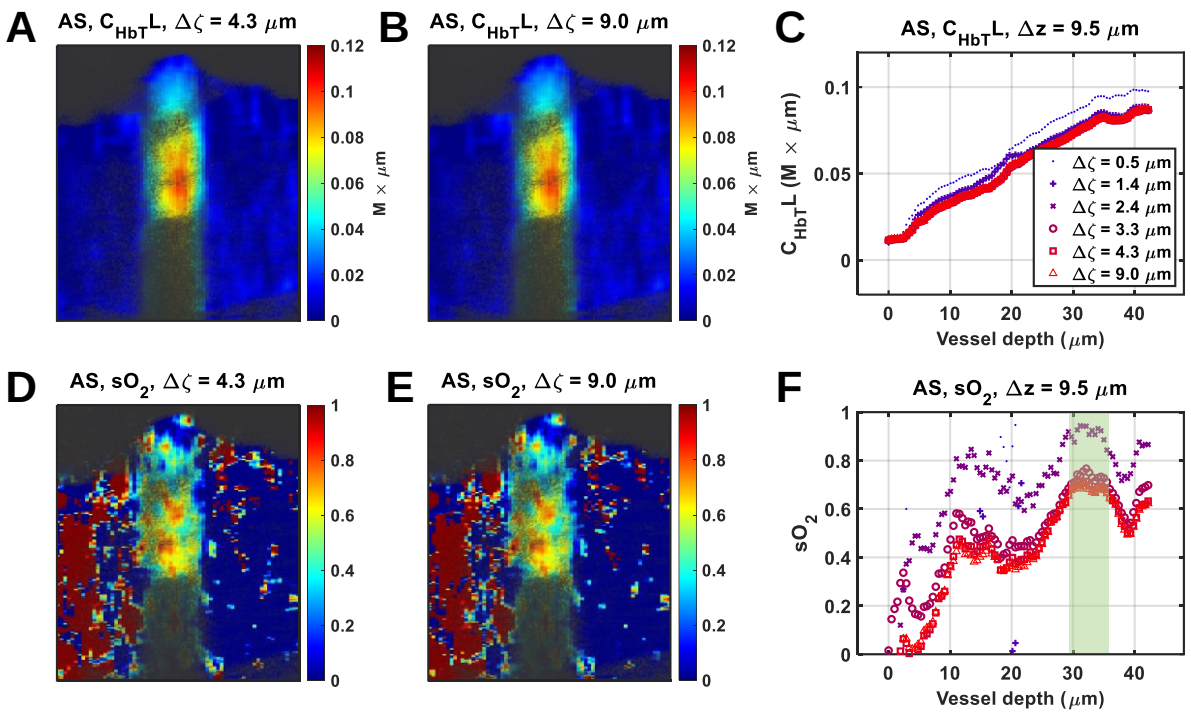

Figure 2-3. AS method provides reasonable estimates of chromophores when fitting lag range (Δζ) is reduced. Consistent estimates of $C_{HbT}L$ (A-B) and sO_2 (D-E) are observed when the autocorrelation fitting lag range is reduced to 4.3 μm (A and D) from 9.0 μm (B and E). This result is reinforced in plots versus depth (C and F). Green shaded area represents the region where sO_2 values are deemed to be most reliable (high $C_{HbT}L$ and R^2). Window size (Δz) is 9.5 μm for all plots.

23.7 μm (**Figure 2-1E-F**, **I-J**), the map of $C_{HbT}L$ is smoother, and sO_2 values are more spatially consistent towards the bottom of the vessel. Note that the AS method shows consistency with the WFT method. The trends of $C_{HbT}L$ are visualized more in detail in **Figure 2-2A-B**. Notably, the AS method achieves a less noisy estimate of C_{HbT}, calculated as the derivative of $C_{HbT}L$ with respect to vessel depth, indicated by the smaller standard error (red shaded area in **Figure 2-2C**). Note that besides fitting-related error, the standard error also includes spatial changes of C_{HbT} estimates within the vessel. Nonetheless, a smaller estimation error bodes well for obtaining chromophore information within highly scattering blood vessels. In addition, the AS method gives reasonable estimation of $C_{HbT}L$ (**Figure 2-3A-B**) and sO_2 (**Figure 2-3D-E**) even when the autocorrelation fitting lag range (Δζ) is reduced to 3.3 μm (**Figure 2-3C** and **F**).

In conclusion, the autocorrelation spectroscopy (AS) approach provides an alternative for obtaining the chromophore information within highly scattering vessels. Preliminary results confirmed the ability of AS

to estimate sO_2 and hemoglobin concentration, even when the autocorrelation fitting lag range was reduced to 3.3 μm. Future work will systematically investigate the accuracy, precision, and spatial-spectral resolution tradeoffs of both approaches experimentally and theoretically.

Chapter 3 Visibility of microvessels in Optical Coherence Tomography Angiography depends on angular orientation

3.1. Abstract

Optical coherence tomography angiography (OCTA) is a widespread tool for depth-resolved imaging of chorioretinal vasculature with single microvessel resolution. To improve the clinical interpretation of OCTA, the conditions affecting visualization of microvessels must be defined. Here we start from the OCTA basics. We take a broader view of OCTA in the context of microvascular hemodynamics and light scattering. Paying particular attention to the unique challenges presented by capillaries versus larger supplying and draining vessels, we critically assess opportunities and challenges in making OCTA a quantitative tool. We then perform experimental investigation of vessel visibility in the 1300 nm window. We inject a scattering plasma tracer (Intralipid) during OCTA imaging of the anesthetized rat eye. In the retina, we find that interlaminar (vertical) vessels that connect laminae have one-fourth to one-third the OCTA red blood cell to tracer (RBC-to-tracer) signal ratio of intralaminar (horizontal) vessels. This finding suggests that the OCTA signal from microvessels depends on angular orientation, making vertically-oriented vessels more difficult to visualize using intrinsic contrast alone. Clinicians should be aware of this potential artefact when interpreting OCTA.

3.2. Introduction

Optical coherence tomography angiography (OCTA) is widely used in ophthalmology to image chorioretinal vasculature[92,93]. OCTA forms images based on intrinsic contrast, arising mainly from the motion of scattering red blood cells (RBCs)[94,95], as well as other scattering cells and particles in blood[96]. Correct interpretation of OCTA requires defining the conditions under which OCTA detects microvessels. To this end, in ophthalmology, OCTA has been validated against fluorescence angiography[97], which is not depth-resolved, and endothelial labelling and *ex vivo* histology[98], which cannot assess RBC perfusion, the

basis of OCTA contrast. Importantly, rheological phenomena are known to affect the OCTA signal. For instance, in OCTA of macrovessels, an "hourglass" pattern can be attributed to the orientation-dependent backscattering of RBCs and their alignment under external stress[99,100], both of which are a consequence of particle asymmetry. Likewise, in OCTA of microvessels, the orientation of elongated RBCs could affect visualization; however, to date, validation studies have been unable to assess this possibility. Therefore, a depth-resolved, co-registered, and *in vivo* validation of OCTA is needed.

Here, we review the relevant basic hemodynamic principles, fundamentals of OCTA, categories of OCTA scanning protocols, and classes of OCTA algorithms. We argue that a rigorous and model-based relationship between hemodynamic parameters, light scattering theory, and measurement observables[101] in OCT angiography will pave the way towards more *quantitative* imaging of hemodynamics by OCTA and related methods, with the potential to enhance all applications. We then provide a validation, by injecting a highly scattering plasma tracer that fills and visualizes perfused retinal and choroidal vessels of rats in OCTA. The tracer provides a useful reference signal that enables us to assess RBC signals more quantitatively. By comparing OCTA before and after tracer filling, we assess the ability of conventional OCTA to visualize microvessels with different angular orientations. Since we use a single imaging system and contrast mechanism to validate OCTA *in vivo,* we avoid limitations of other complex validation studies that must co-register multiple modalities.

3.3. OCTA Fundamentals

The microcirculation comprises a network of blood vessels that delivers oxygen and nutrients to surrounding tissues, removes waste products and heat, and otherwise supports tissue viability[102-104]. Red blood cells (RBCs) are the main carriers of oxygen in blood. By enabling the visualization of cell-perfused vasculature without an exogenous contrast agent, OCT angiography has generated enormous interest in ophthalmology[92,105-111], gastroenterology[112,113], cancer biology[4,114], and neuroscience[5,115] over the past decade. It has been particularly useful in studying diseases where the microvascular morphology or presence of perfusion changes over time.

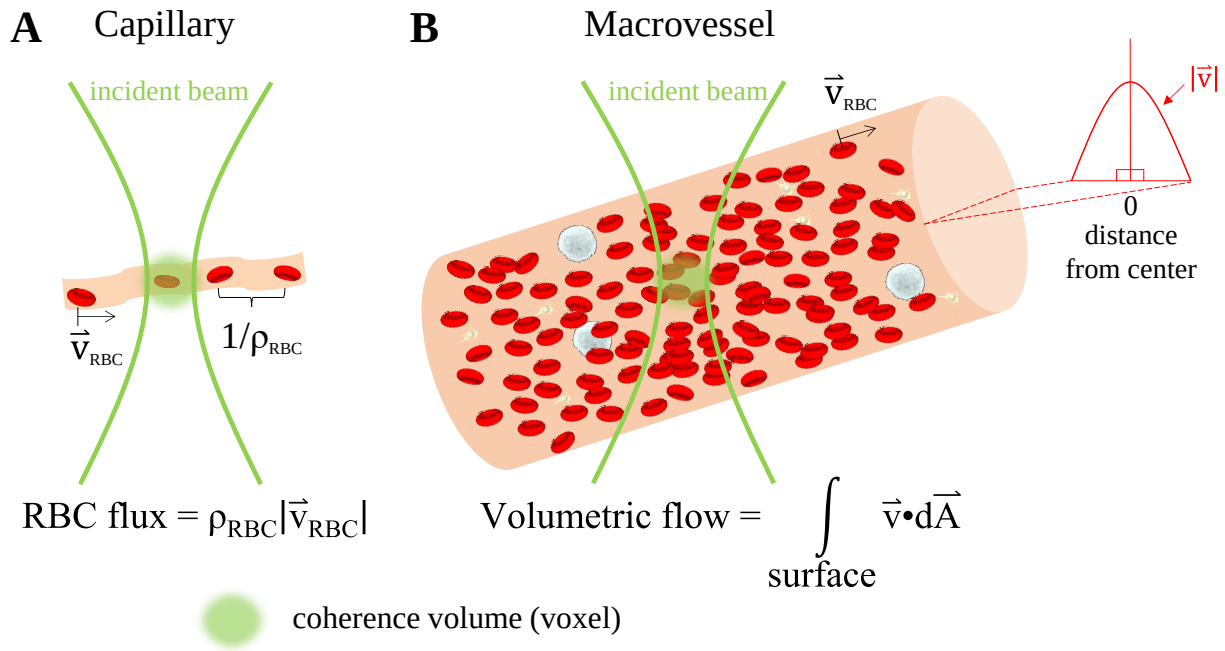

Figure 3-1. (A) Flow in capillaries (microvessels with diameters of <10 µm) is single-file, usually with highly variable hematocrits that fall below systemic levels; (B) On the other hand, macrovascular flow often follows a blunted laminar profile at near-systemic hematocrits. Consequently, different approaches are required to quantify microvascular versus macrovascular hemodynamics via OCTA (Optical Coherence Tomography Angiography) imaging.

A unifying feature of all OCTA algorithms is that they visualize objects that are both moving and backscattering. Hence, we begin our review with a discussion of hemodynamics and light scattering properties of blood. Importantly, we distinguish between capillaries (<10 µm in diameter), where RBCs flow in a line and hematocrits are low, and macrovasculature, where RBCs flow side-by-side and hematocrits approach systemic levels, with the understanding that non-capillary microvessels (10–100 µm in diameter) represent an intermediate case between the two extremes discussed here[103,104].

3.3.1. Hemodynamic Parameters

What are the hemodynamic main parameters that impact observed OCTA signals? In capillaries (**Figure 3-1A**), the RBC flow is single-file, with plasma gaps in between[116,117]. RBC speed (distance/time), flux (#/time), and linear density (#/distance) are thus primary hemodynamic parameters in capillaries. Due to the plasma gaps between cells, flux can often be determined by imaging individual capillaries and counting RBCs traversing a single location[117]. Assuming single-file capillary flow, microvascular tube hematocrit

(H_{tube}), or RBC volume fraction, is related to linear density (ρ) by $\rho=H_{tube}A/V_{RBC}$, where V_{RBC} is the red blood cell volume and A is the vessel cross-sectional area. Capillary tube hematocrit is generally a factor of ~2–3× lower than systemic levels[118], but hematocrit can vary considerably between capillaries. In macrovessels (**Figure 3-1B**), which include supplying arteries and draining veins, the blood velocity varies across the vessel cross-section. In contrast to microvessels, macrovascular hematocrit approaches systemic levels of ~40%–45%[119]. Flow is typically laminar with some degree of blunting[118], with the largest shear rate, or velocity gradient, at the edge of the vessel. In macrovessels, RBC velocity or speed (distance/time), flow rate (volume/time), and hematocrit (volume/volume) are the primary hemodynamic parameters. All hemodynamic parameters vary over time with respiration and the heartbeat of the subject[120].

3.3.2. Light Scattering from Red Blood Cells

What are the physical properties of RBCs that enable their detection by OCTA? RBC scattering and absorption properties derive from the presence of hemoglobin and its complex refractive index[121]. Major absorption bands of hemoglobin, related to the imaginary part of the complex refractive index, predominate at visible and shorter wavelengths, while hemoglobin absorption becomes negligible at near-infrared wavelengths, where scattering dominates. The light scattering properties of individual RBCs are determined by the refractive index contrast with respect to the surrounding plasma, as well as their shape and size relative to the medium wavelength. The real part of the complex refractive index, or refractive index, of hemoglobin is larger by ~3%-6% relative to the surrounding plasma[121-123]. RBCs are biconcave disks (**Figure 3-2**), with a diameter of 6-8 μm and thickness of ~2 μm, although their shape changes under external stress. Due to the large volume fraction of RBCs and their refractive index mismatch relative to plasma, RBCs are the main scattering constituent in blood[122,124,125].

The scattering properties of both individual RBCs and ensembles of RBCs are important in OCTA. Due to their irregular shape, the probability of light scattering in a given direction for a particular RBC depends on both its orientation and the direction of incident light. An ensemble of RBCs with different orientations can be characterized by a scattering coefficient (μ_s), the scattering probability per unit distance; a scattering

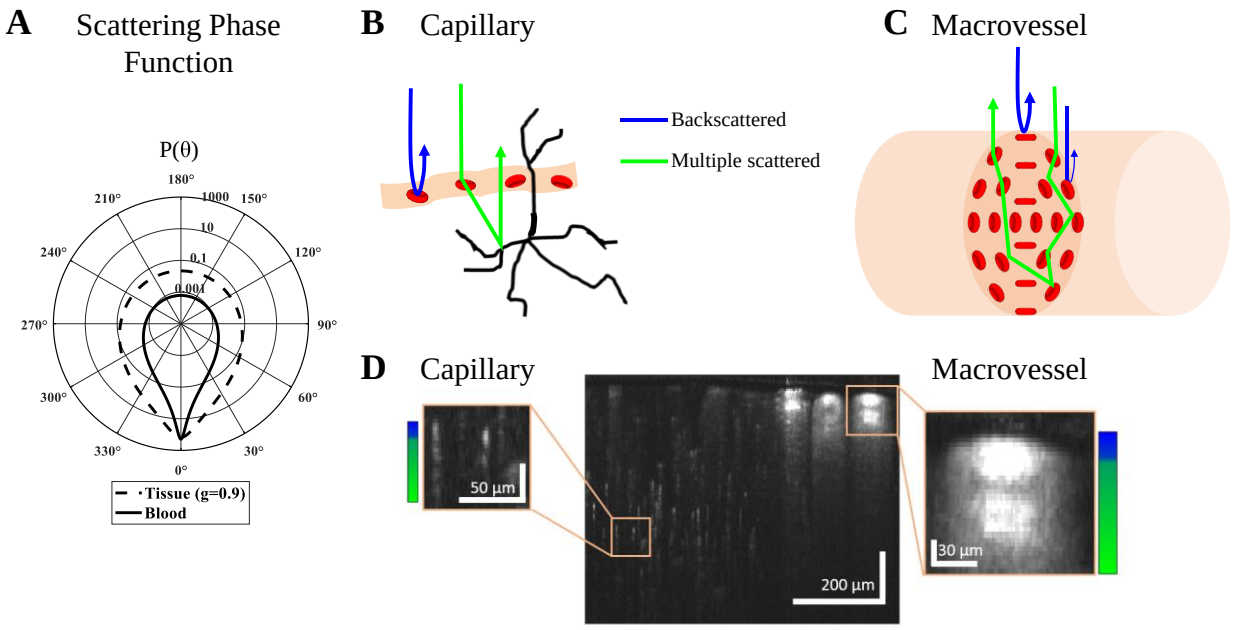

Figure 3-2. Single and multiple scattering in the OCTA of capillaries versus macrovasculature. (A) Blood has a high scattering anisotropy, leading to a high probability of detecting multiple scattered light paths; (B) For capillaries, dynamic RBC (red blood cell) forward scattering precedes or follows static tissue backscattering, which leads to "multiple scattering" tails; (C) In large vessels, the backscattering cross-section is determined by the shear-induced orientation of RBCs with their flat face parallel to the shear force. If the vessel lumen exceeds a scattering length, multiple intravascular dynamic scattering events (green) before detection are likely; (D) Cross-sectional OCT (Optical Coherence Tomography) angiogram of the mouse brain at 1300 nm (complex interframe subtraction method) with a qualitative colorbar showing the balance of backscattered light (blue) and multiple scattered light (green) in a capillary (left) and macrovessel (right).

phase function (P(θ)), the probability of scattering in a given elevation direction θ per unit solid angle; and a scattering anisotropy (g = E[cos(θ)]), the expectation or average (E[ ]) of cos(θ) over solid angle. These parameters characterize scattering of whole blood, which comprises an ensemble volume of RBCs with random orientations. In whole blood, empirically measured g and μ_s include dependent and multiple scattering effects[126]. With a hematocrit of around 45%, whole blood is found to be highly forward scattering between 750 and 950 nm, with a scattering coefficient (μ_s) between 65 and 80 mm^{-1}, and anisotropy (g) between 0.97 and 0.99[124,127-129]. Exemplary phase functions[125,127,130] for tissue (Henyey-Greenstein with g = 0.9) and blood (Gegenbauer-Kernel with g = 0.972 and $\alpha = 0.49$[131]) are shown in **Figure 3-2A** on a logarithmic scale. Tissue has a higher probability of back scattering than blood, while blood is considerably more forward scattering.

In OCTA (**Figure 3-2B-C**), detected light ideally results from paths with single RBC backscattering (θ = 180°) events (blue). However, the high RBC anisotropy (**Figure 3-2A**) makes detection of multiple scattered light (green) likely. Probable light paths can be understood through the principles of radiative transport. In capillaries, where RBC flow is single-file, light forward scattered from RBCs is also backscattered from extravascular tissue (**Figure 3-2B**), creating axial multiple scattering tails (**Figure 3-2D** left box). In macrovessels, there are two important effects. First, RBCs tend to align their flat face parallel to the shear force, i.e., facing outwards along the vessel circumference (**Figure 3-2C**). The largest backscattering cross-section occurs when the shortest RBC dimension is aligned with the incident light. Therefore, the signal is enhanced at the top and bottom of the vessel lumen and reduced at the side (**Figure 3-2D** right box)[99]. At higher shear rates, RBCs elongate and the backscattering pattern disappears[132]. Second, for vessel lumens larger than a scattering length ($1/\mu_s$), multiple intravascular dynamic scattering events (green) can occur before detection.

As OCTA images are created by post-processing OCT data, OCTA has an image penetration depth comparable to or less than OCT. This is typically ~0.5–1.5 mm in most tissues, depending on the source wavelength and the sample optical properties[133,134]. It is important to note that while OCTA visualizes blood vessels, the penetration depth of OCTA may be determined by the attenuation of both intravascular and extravascular tissue.

3.4. OCTA Signal

In this section, we provide a unifying framework for the OCT signal to facilitate the discussion of OCTA algorithms in **Section 3.5**. Commonly-used symbols or variables and their definitions are summarized in **Table 3-1**, while other symbols are defined in the text.

Table 3-1. Symbols or variables used and their meaning.

Symbol	Meaning
S	Complex OCT signal/field
$\|S\|$	Amplitude of the OCT signal
$I=\|S\|^2$	Intensity of the OCT signal

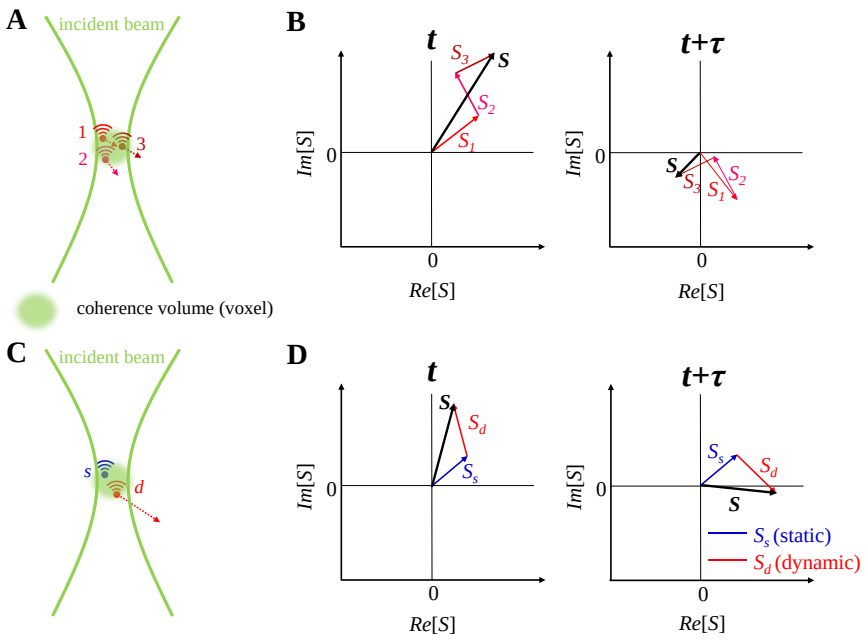

Figure 3-3. The motion of scatterers in a coherence volume gives rise to complex field fluctuations that form the basis for OCTA signals. The contributions to the complex field are shown at two different points in time (t and t + τ). (A, B) Field fluctuations due to dynamic scatterers in a coherence volume. (C, D) Field fluctuations due to a combination of static (blue) and dynamic (red) scatterers in a coherence volume.

∅	Phase of the OCT signal
S_m	OCT field from one scatterer
SV	Speckle variance
cmOCT	Correlation mapping OCT signal
PV	Phase variance
Δ∅	Phase difference
ΔS	Complex field difference
CDV	Complex differential variance
R	Autocorrelation function
P	Power spectral density

All standard OCTA algorithms[135,136] start from the complex OCT signal. The complex, depth-resolved OCT signal can be expressed as:

$$S(x,z,t) = |S(x,z,t)| \exp\{i\phi(x,z,t)\}. \quad (3.1)$$

Note that S(x,z,t) is related to the depth-resolved optical field, integrated over a resolution element (coherence volume). Therefore, the depth-resolved intensity, I(x,z,t), is equivalent to the magnitude square of the field, i.e., $I(x,z,t)=|S(x,z,t)|^2$. OCTA algorithms may operate on either S(x,z,t), ∅(x,z,t), or I(x,z,t) as the "signal", and accordingly, can be categorized into complex field-based techniques, phase-based

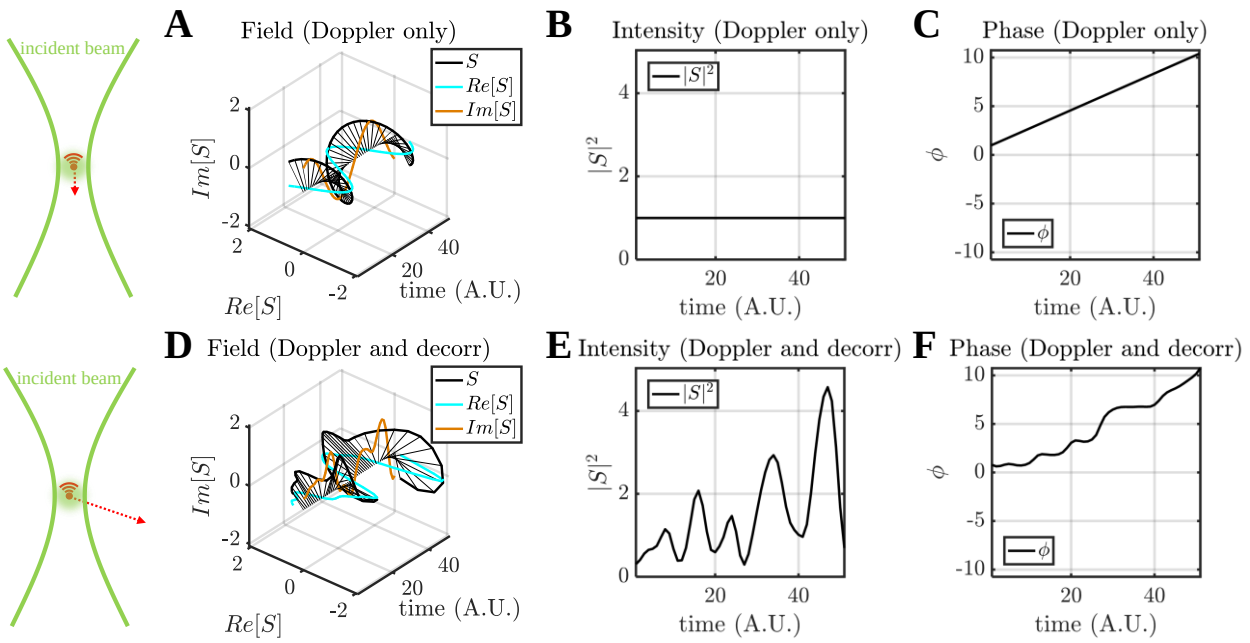

Figure 3-4. The major categories of OCT signal fluctuations are Doppler shifts and decorrelation. Comparison of complex field, intensity, and phase time courses, for the case of a pure Doppler shift (A-C) and a Doppler shift with decorrelation (D-F). For a pure Doppler shift, the field traces out a helical pattern (A), whereas decorrelation introduces random deviations from this pattern (D).

techniques, and intensity-based techniques. In its simplest form, OCTA employs differences between OCT signals at the same spatial position over a series of time points to highlight scatterer motion. As discussed in **Section 3.3.2**, RBCs are the main blood scattering component. Due to the dynamic motion of RBCs, the overall field, phase, and intensity fluctuate. For the field, these variations are determined, in a statistical sense, by the first-order field autocorrelation function, $r(\tau)$, in which $r(\tau) = R(\tau)/R(0)$ and $R(\tau) = E[S(x,z,t+\tau)S^*(x,z,t)]$, where $E[\,]$ represents expectation and τ is the time lag. Under some circumstances, all other signal variations, including those of the intensity and phase, derive their statistical properties from the field autocorrelation[137].

OCT complex signal dynamics are illustrated in **Figure 3-3**. The complex signal is treated as a complex summation of backscattered fields from individual scatterers within the coherence volume. The coherence volume is defined by the beam waist in the transverse direction and the coherence length in the axial direction. Changes in the fields from individual scatterers over time leads to changes in the total signal over time (**Figure 3-3A-B**). In many practical situations, scatterers may be further classified as “dynamic” and

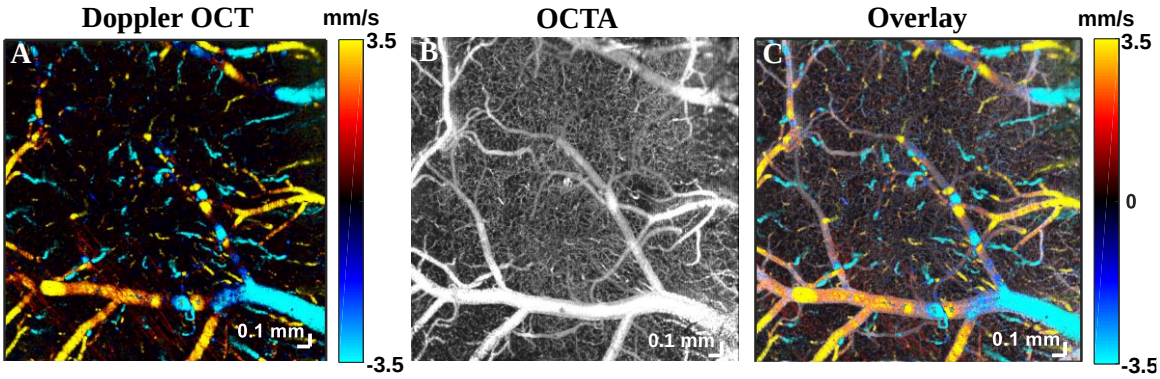

Figure 3-5. Doppler OCT and OCTA in the mouse brain. (A) Doppler OCT can visualize flow based on Doppler shifts, caused by motion in the axial direction, towards or away from the probe beam. On the other hand, OCTA visualizes flow based on decorrelation, usually caused by translational motion through the coherence volume, as well as Doppler shifts. The overlay of both methods (C) shows that Doppler OCT is mainly limited to ascending venules or descending arterioles, where Doppler shifts dominate. On the other hand, OCTA, which is sensitive to decorrelation, more comprehensively shows vasculature, including regions with predominantly transverse flow. A standard Kasai algorithm was used on transversally oversampled images for (A) and a complex interframe subtraction method was used on rapidly acquired repeated cross-sectional images for (B).

"static" depending on whether they move or not, with both scatterer types contributing to the signal in the same coherence volume (**Figure 3-3C-D**).

The nature of scatterer dynamics plays a major role in determining the OCT signal changes (**Figure 3-4**). Generally, scatterer motion is accompanied by both a Doppler shift and decorrelation[138]. When the scatterer has an axial velocity component, moving towards or away from the incident beam, the complex field rotates, tracing a helix over time (**Figure 3-4A-C**). This effect can be described as a linear phase shift over time due to the Doppler effect, or a "Doppler phase shift". When the scatterer is undergoing a dynamic conformational change, rotation, or translational motion through the coherence volume, both the OCT signal intensity and phase change randomly (**Figure 3-4D-F**). This random change of the complex field is known as decorrelation. Doppler shifts are associated with a change in the phase of the complex field autocorrelation, while decorrelation is associated with a decrease in the magnitude of the complex field autocorrelation, $|R(\tau)|$, with increasing τ.

Both Doppler shifts and decorrelation are present to varying degrees in all vasculature. Note that a Doppler shift due to translational axial motion through the coherence volume implies decorrelation. On the other hand, decorrelation occurs even for transverse motion or rotation, and does not necessarily imply a Doppler

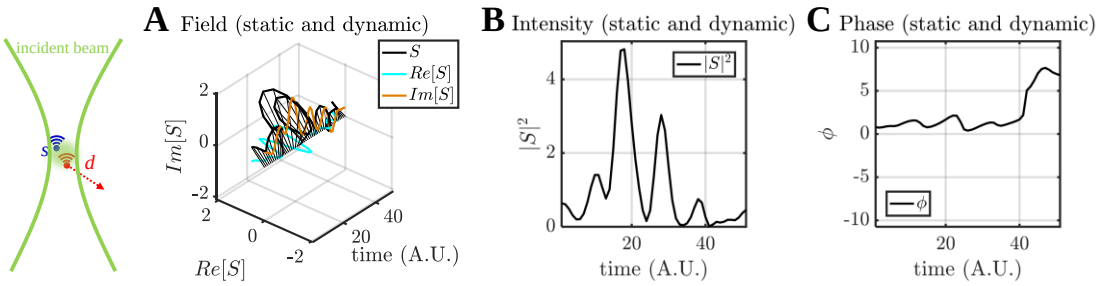

Figure 3-6. Comparison of complex field (A), intensity (B), and phase (C) time courses when both static and dynamic scattering are present in a coherence volume (with Doppler shift and decorrelation of the dynamic component). Such coherence volumes are present at the edges of vessels.

shift. To illustrate this, **Figure 3-5** shows a comparison between Doppler OCT and OCTA of mouse brain microvasculature. Doppler OCT detects phase changes caused by translational axial motion[139]. The requirement for axial phase shifts renders Doppler OCT only sensitive to motion parallel to the incident beam. Doppler shifts predominate in larger microvessels which are ascending or descending (**Figure 3-5A**); hence when used for angiography, the Doppler effect provides only a partial microvascular map. By comparison, decorrelation involves random deviations of the complex field and predominates in vessels with transverse flow. Thus, OCTA, which senses decorrelation via intensity and/or phase, more comprehensively shows the vasculature (**Figure 3-5B-C**).

Finally, it should be noted that the presence of static scattering can significantly alter time courses. The OCT field, intensity, and phase time courses due to dynamic scattering in the presence of a static scatterer are shown in **Figure 3-6**. As suggested by **Figure 3-3D**, the presence of static scattering confines the field fluctuations to a portion of the complex plane (**Figure 3-6A**). As will be discussed in **Section 3.8.1**, the possible presence of static scatterer(s) must be considered in order to recover quantitative information about the Doppler phase shift or the decorrelation rate in OCTA.

3.5. OCTA Algorithms

The previous section showed that OCTA signals depend on the type of dynamics (Doppler shift or decorrelation), the observed parameter (intensity, phase, or field), and the possible presence of static

scattering in the coherence volume. With this discussion in mind, we now present the main classes of angiography algorithms.

3.5.1. Intensity- or Amplitude-Based OCTA Algorithms

Intensity-based OCTA algorithms use $I(x,z,t)=|S(x,z,t)|^2$, while amplitude-based OCTA algorithms use $|S(x,z,t)|$ in **Equation (3.1)**.

The first class of intensity-based OCTA algorithms is the speckle variance method. Speckle[140] can be described as the random interference of scattering fields (indexed by m) that cannot be resolved within a coherence volume:

$$S(z) = \sum_m S_m(z), \tag{3.2}$$

S_m represents the fields within a coherence volume, each weighted according to the point spread function at the scatterer location (**Figure 3-3**). The intensity (as well as the phase and field) changes over time as the configuration of scatterers changes, causing decorrelation (**Figure 3-4D-F**). Decorrelation can occur as RBCs pass through a coherence volume, but may also occur due to rotational motion or diffusion. In 2005, Barton and Stromski showed the feasibility of flow speed measurement without phase information by evaluating speckle pattern changes[141]. In 2008, Mariampillai et al.[142] used interframe speckle variance to visualize microcirculation. In Mariampillai et al.[142], speckle variance was defined as:

$$SV(x,z) = \frac{1}{N} \sum_{t=0}^{(N-1)T} [I(x,z,t) - \overline{I(x,z)}]^2, \tag{3.3}$$

where t = 0, T, 2T, …, (N-1)T represents the OCT acquisition time; T is the time interval; N is the total number of acquisitions at the same position; x and z denote lateral and depth indices, respectively; and $\overline{I(x,z)}=\overline{|S(x,z)|^2}$ is the time-averaged intensity at position (x,z). This is a temporally averaged, variance-based algorithm without normalization. By ignoring the phase in **Equation (3.1)**, the method is not sensitive to pure Doppler shifts. Consequently, speckle variance is not susceptible to phase noise. However, the

speckle variance method may be compromised due to interframe bulk tissue motion. While in-plane (xz) motion can be compensated in principle, out-of-plane motion is more challenging to correct. To minimize motion effects, later in 2010, Mariampillai et al.[143] optimized the frame number and frame rate for a given level of bulk tissue motion, through maximizing the speckle variance signal-to-noise ratio (SNR) between a "dynamic" and "static" pixel. Speckle variance SNR is calculated as:

$$SV_{SNR}(N,\overline{I(x,z)}) = \frac{SV_{Dynamic}(N,\overline{I(x,z)}) - SV_{Static}(N,\overline{I(x,z)})}{\sqrt{\sigma^2{}_{Dynamic}(N,\overline{I(x,z)}) + \sigma^2{}_{Static}(N,\overline{I(x,z)})}}, \tag{3.4}$$

where $\overline{I(x,z)}$ is the time-averaged intensity for both "dynamic" and "static" pixels, $SV_{Dynamic}$ and SV_{Static} are speckle variances calculated from **Equation (3.3)**, and $\sigma^2_{Dynamic}$ and σ^2_{Static} are variances of $SV_{Dynamic}$ and SV_{Static}, respectively. By optimizing the frame number under conditions of low tissue bulk motion, capillaries can be reliably detected[143].

As the dynamic tissue signal has a lower temporal correlation, at a given time lag, than static tissue, correlation has been investigated as a parameter for angiography. In 2011, Enfield et al.[144] demonstrated *in vivo* human volar forearm imaging of the capillary density and vessel diameter with correlation mapping optical coherence tomography (cmOCT). The correlation between OCT frames acquired at time t and t+T at the same position is:

$$cmOCT(x,z) = \sum_{p=0}^{V}\sum_{q=0}^{W} \frac{[I(x+p,z+q,t)-\overline{I(t)}][I(x+p,z+q,t+T)-\overline{I(t+T)}]}{\sqrt{[I(x+p,z+q,t)-\overline{I(t)}]^2+[I(x+p,z+q,t+T)-\overline{I(t+T)}]^2}}, \tag{3.5}$$

where V and W define the extent of the spatial region for correlation calculation, and $\overline{I(t)}$ denotes the spatially averaged intensity over this region. This is a spatially averaged, correlation-based algorithm with normalization. After this calculation, a 2D correlation map can be formed by applying a threshold to binarize the image into static and dynamic regions. In 2012, Jia et al.[145] proposed split-spectrum amplitude-decorrelation angiography (SSADA) to image the human macula and optic nerve head. Ensuring a nearly

isotropic coherence volume size by splitting the spectrum to degrade the axial resolution to equal the transverse resolution, they then applied a method similar to cmOCT.

3.5.2. Phase-Based OCTA Algorithms

Phase-based OCTA algorithms rely on ∅(x,z,t) in **Equation (3.1)** to distinguish dynamic and static tissue. Doppler OCT, a category of phase-based OCTA, uses a deterministic Doppler phase shift for *in vivo* blood flow measurements[146,147]. While Doppler OCT can quantify flow, visualization applications are limited due to its angle dependence (**Figure 3-5A**). For instance, retinal blood vessels are nearly perpendicular to the optic axis, particularly outside of the optic nerve head, yielding insufficient phase shifts for Doppler measurements[136]. Power Doppler[148,149] and phase variance imaging[150] represent alternative approaches that are sensitive to decorrelation, or random non-deterministic Doppler shifts. In 2007, Fingler et al.[151] proposed phase variance for motion contrast. In Kim et al.[152], the phase variance at position (x,*z*) is defined as:

$$PV(x,z) = \frac{1}{N-1} \sum_{t=0}^{(N-2)T} [\Delta\phi(x,z,t) - \overline{\Delta\phi(x,z)}]^2. \quad (3.6)$$

The phase difference at a given location is given by:

$$\Delta\phi(x,z,t) = \phi(x,z,t+T) - \phi(x,z,t), \quad (3.7)$$

where T is the time lag. **Equation (3.6)** is a temporally averaged, variance-based algorithm without normalization. Phase-based OCTA algorithms are advantageous over amplitude- and intensity-based algorithms if phase changes but intensity and amplitude do not. However, phase-based OCTA loses information about the OCT signal amplitude and intensity. Moreover, phase-based OCTA may not detect changes in the presence of a large static scattering component. Similar to amplitude- and intensity-based algorithms, phase-based OCTA is sensitive to decorrelation (**Figure 3-4E-F**). However, as phase is particularly sensitive to axial motion, additional bulk motion phase correction is typically required. In their work[151], before phase variance analysis, Fingler et al. removed the bulk motion phase change:

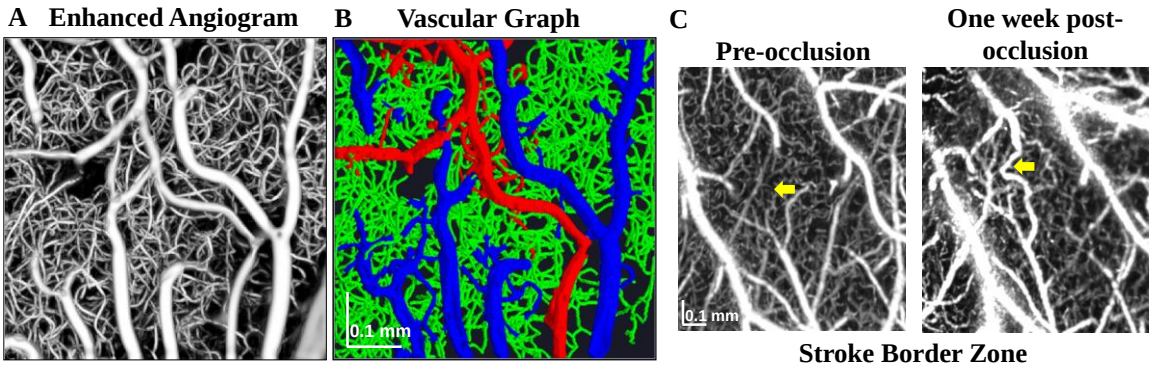

Figure 3-7. OCTA microscopy of the mouse brain enables an assessment of vascular connectivity (A, B) and longitudinal monitoring of microvascular remodeling (C) one week after distal middle cerebral artery occlusion (yellow arrow).

$$\Delta\phi^{corr}(x,z,t) = \Delta\phi(x,z,t) - \Delta\phi^{bulk}(x,t), \tag{3.8}$$

where $\Delta\phi^{corr}(x,z,t)$ denotes the corrected phase change, and $\Delta\phi^{bulk}(x,t)$ represents the phase change due to bulk motion, estimated as:

$$\Delta\phi^{bulk}(x,t) = \sum_{z=a}^{b}[|S(x,z,t)\Delta\phi(x,z,t)|] \Big/ \sum_{z=a}^{b}[|S(x,z,t)|]. \tag{3.9}$$

The phase change due to bulk motion is thus calculated by a weighted mean from $z = a$ to $z = b$ in one A-scan. Note that bulk phase change estimation based on cross-correlation is also possible[5,153].

3.5.3. Complex Signal-Based OCTA Algorithms

Complex signal-based OCTA algorithms use $S(x,z,t)$, the complex field, which includes both the intensity/amplitude and phase in **Equation (3.1)**. As both intensity and phase fluctuations (**Figure 3-4B-C,**

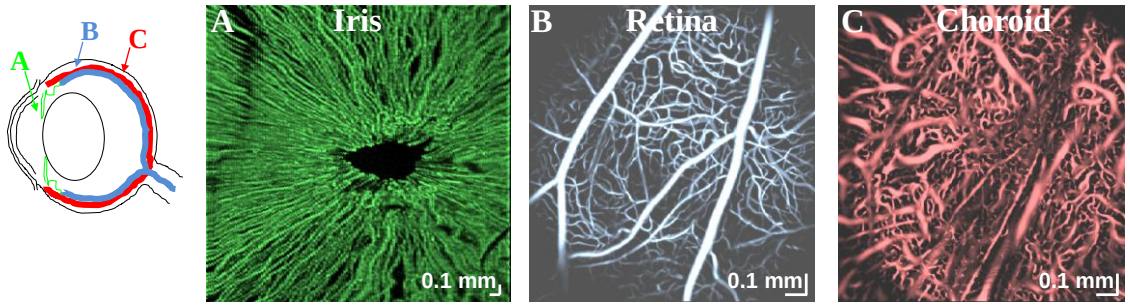

Figure 3-8. Ocular OCTA of iris (A), retina (B), and choroid (C). Hessian vesselness enhancement was applied to retinal and choroidal vasculature before display. Note that the pupil was dilated prior to OCTA acquisition for (B,C).

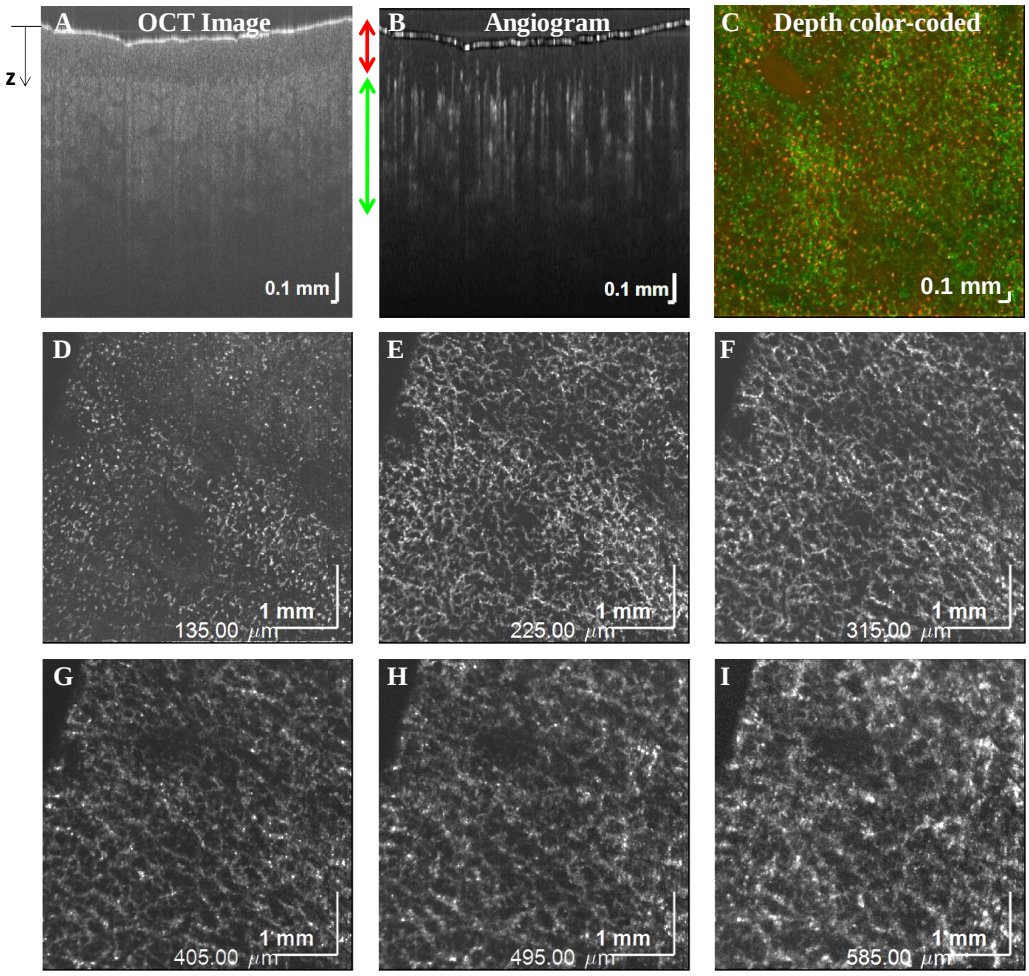

Figure 3-9. OCTA of the skin on a pig ear. OCT cross-sectional intensity image (A) and angiogram (B) determined by complex subtraction. (C) Overlay of superficial vessels in the epidermis (red) with deeper vasculature in the dermis (green). (D–I) Maximum intensity projections centered at different axial (z) positions relative to the surface.

E-F) arise from field fluctuations (**Figure 3-4A, D**), we assert that the complex field is more fundamental than either the intensity or phase. In particular, the static component can be readily handled in the complex domain (**Figure 3-6**). Also, unlike intensity-based OCTA, complex signal-based OCTA is sensitive to slow flow with only phase changes[154]. In 2007, Wang et al.[6] demonstrated complex signal-based OCT angiography, also called optical microangiography (OMAG), for the first time, while interframe complex OCTA was introduced later[5,155]. The most basic complex OCTA algorithm is based on subtraction,

$$\Delta S(x,z,t) = |S(x,z,t+T) - S(x,z,t)|, \tag{3.10}$$

where S(x,z,t+T) and S(x,z,t) are complex OCT signals acquired at the same position separated by a time lag T. This is a difference-based algorithm without normalization. Spatial or temporal averaging may be applied as needed. This expression may also be generalized as a variance calculation (or high-pass filter[5]) that eliminates static scattering:

$$\Delta S(x,z) = \frac{1}{N}\sum_{t=0}^{(N-1)T} |S(x,z,t) - \overline{S(x,z)}|^2 . \quad (3.11)$$

This is a temporally averaged, variance-based algorithm without normalization. As static and dynamic scatterer fields add in the complex domain (**Figure 3-6**), the above expression correctly eliminates static scattering to quantify the dynamic scattering signal.

Using a complex signal-based algorithm, several applications of OCTA are demonstrated here. **Figure 3-7A-B** shows OCTA graphing of the mouse brain vasculature *in vivo*. Longitudinal monitoring of recovery in the mouse brain, one week after an experimental ischemic stroke, is shown in **Figure 3-7C**. Note the presence of vascular remodeling (yellow arrows). **Figure 3-8** shows OCTA of a rodent eye *in vivo*. **Figure 3-9** presents OCTA of pig ear skin, including a cross-sectional intensity image (**Figure 3-9A**), cross-sectional angiogram image (**Figure 3-9B**), color-coded angiogram of superficial and deep vasculature (**Figure 3-9C**), and angiograms centered at different depths (**Figure 3-9D-I**). All figures employ a complex interframe subtraction algorithm for angiography.

In 2014, Nam et al. [156] proposed a complex differential variance (CDV) algorithm. This differential variance algorithm, applied to the OCT signal at a position (x,z), is:

$$CDV(x,z) = \sqrt{1 - \frac{\sum_{t=0}^{(N-2)T} |\sum_{k=-L}^{L} w_k S(x,z-k,t) S^*(x,z-k,t+T)|}{\sum_{t=0}^{(N-2)T} \sum_{k=-L}^{L} w_k \frac{1}{2}[I(x,z-k,t) + I(x,z-k,t+T)]}}, \quad (3.12)$$

where w_k is a depth-dependent window function of length 2L+1. Though it is referred to as a "variance" method, this algorithm is actually a spatially and temporally averaged, correlation-based method with

normalization (see the discussion of variance versus correlation in **Section 3.5.4**). The correlation is estimated by averaging on a complex basis axially (in z) and a magnitude basis over time. Also note that the correlation definition is the complex conjugate of that used elsewhere in this paper, though due to the absolute value operation, this minor discrepancy has no effect on the final CDV.

3.5.4. Classification of Present OCTA Algorithms

Historically, all of the OCTA algorithms described above were novel at the time they were introduced. However, with the benefit of hindsight, we propose basic categories to classify OCTA algorithms in **Table 3-2**.

Table 3-2. Classification of OCTA algorithms.

Category	Classification
OCT signal	Field vs. Intensity/Amplitude vs. Phase
Calculation	Variance/Difference vs. Correlation
Averaging method	Temporal vs. Spatial vs. Spectral
Normalization	Normalized vs. Non-normalized

The primary distinction between algorithms, discussed in **Sections 3.5.1** to **3.5.3**, is the OCT signal(s) employed. The second distinction, which is emphasized in the literature, is between variance/difference-based methods and correlation-based methods. However, here we argue that in some cases, this distinction is meaningless. Difference-based methods are actually estimating the following:

$$D(T) = E[|X_{t+T} - X_t|^2], \tag{3.13}$$

where D(T) denotes the difference at a time lag of T and X_t can be the OCT field, intensity, or amplitude at time t. Variance-based methods are estimating the following:

$$V = E[|X_t - E(X_t)|^2]. \tag{3.14}$$

On the other hand, the un-normalized autocorrelation is defined as:

$$R(T) = E[X_t^* X_{t+T}]. \tag{3.15}$$

Further expanding **Equation (3.13)**, the difference can be written in terms of the autocorrelation:

$$D(T) = E[|X_{t+T}|^2] + E[|X_t|^2] - 2\,\mathrm{Re}\{E[X_t^* X_{t+T}]\} = 2R(0) - 2\,\mathrm{Re}\{R(T)\}. \quad (3.16)$$

Therefore, difference and correlation methods are very closely connected if R(T) is real. If R(T) is complex, as would be the case if X_t represented the field and Doppler shifting were present, the difference D(T) depends only on the real part of R(T). From **Equation (3.14)** and **(3.15)**, it can be readily shown that R(0)=V if $E[X_t]=0$. Thus, every difference method corresponds to an equivalent correlation method via **Equation (3.16)**.

The third distinction between algorithms is the way that the expectation, E[ ], is realized in practice. One method of realizing the expectation is by averaging over time. Another way is by averaging over space, at different tissue locations. Yet another way is spectral or optical wavelength averaging, employed in split-spectrum methods[145]. Under the assumption of ergodicity[91], all averaging methods are asymptotically equivalent, and in practice, all can be used to some degree. However, note that averaging over one dimension will automatically degrade the resolution in that dimension.

Fourth, OCTA methods can be distinguished by the use of normalization. The normalized correlation is divided by the signal power, R(0):

$$r(T) = R(T) / E[|X_t|^2] = R(T) / R(0). \quad (3.17)$$

For the complex signal, the power R(0) is related to the total scattering within a coherence volume. In a vessel, this depends on the backscattering cross-section of RBCs (which depends on orientation according to **Section 3.3.2**), and the RBC density (hematocrit). As discussed further in **Section 3.8.1**, $|R(\tau)|$ is a monotonically decreasing function under certain conditions, with the decorrelation rate, or rate of autocorrelation decay, being proportional to speed. As difference methods depend on R(0) and R(T), there are two regimes to consider in understanding **Equation (3.16)**. The first is when T is much longer than the intrinsic decorrelation time. In this case, $R(T) \ll R(0)$, and D(T) is proportional to the signal power R(0), typically related to backscattering (RBC density and orientation). If T is on the order of the intrinsic

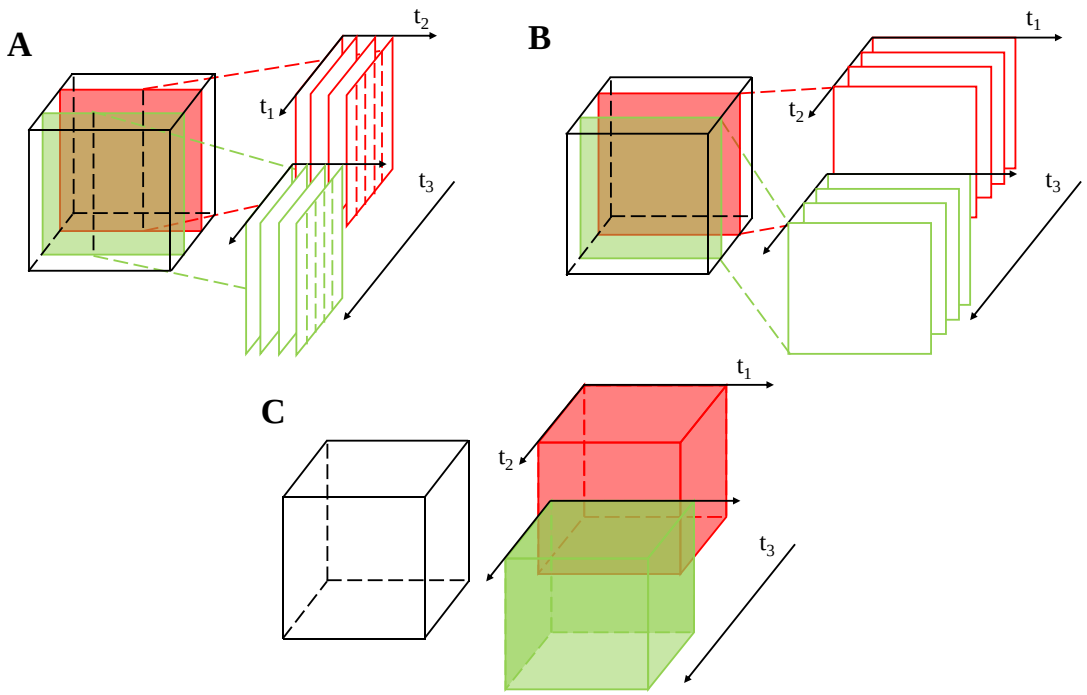

Figure 3-10. Volumetric OCTA scanning protocols can operate with respect to A-scan (A), frame (B), or volume (C). A cubic volume is scanned with time scales t_1, t_2, and t_3. Data acquired sequentially along time scale t_3 are shown in red and green. (A) MB-scan: multiple A-scans are obtained at one lateral position before switching to the next lateral position; (B) BM-scan or interframe scan: multiple B-scans are obtained at one cross-sectional location before switching to the next location; (C) intervolume scan: successive scans of the whole volume. Each scan achieves a progressively larger observation time for a single spatial position ($t_3 > t_2 > t_1$).

decorrelation time, the difference D(T) depends on both the signal power R(0) and the decorrelation rate. In this case, the interpretation of the difference D(T) becomes more ambiguous, and it can be affected by the signal power or decorrelation rate, which can be impacted by the RBC density, orientation, and speed. With the normalization in **Equation (3.17)**, r(T) is more directly related to the rate of decorrelation, and hence, the RBC speed. However, to rigorously account for the possible presence of static scattering, measurements at several time lags[9] are required.

3.6. OCTA Scanning Protocols

The efficiency and sensitivity of OCTA measurements are determined by the OCTA scanning protocol. At a fundamental level, scanning protocols can be categorized based on whether the analysis is performed on consecutive A-scans, frames, or volumes. **Figure 3-10** shows the so-called MB-scan, BM-scan and intervolume scanning methods. In **Figure 3-10**, the cube represents the imaged object, and t_1, t_2, t_3 are the

first, second, and third OCT scanning time scales, respectively, with $t_3 > t_2 > t_1$. Each protocol can be characterized by the time duration for which a single location is observed.

To our knowledge, Fingler et al.[151] were the first to rigorously compare different OCTA scanning patterns. They compared the MB-scan (**Figure 3-10A**) and the BM-scan (**Figure 3-10B**), using a phase contrast algorithm. An M-scan is a repeated zero-dimensional scan at a single position, while a B-scan is a one-dimensional scan along a single axis. An MB-scan comprises multiple A-scans taken at one lateral position before switching to the next position (**Figure 3-10A**), while a BM-scan comprises repetitive B-scans taken along the same cross-section (**Figure 3-10B**). According to Fingler et al.[151], the advantages and disadvantages of the two scanning methods are described here.

The MB-scan is an extension of Doppler OCT protocols. By increasing N, the number of A-scans per M-scan, the dynamic range for the measurement increases. However, the MB-scan is not time-efficient, because the total observation time for a single location is $\sim t_1$. Unless the dwell time is very long, $|r(t_1)| \sim 1$; thus it is challenging to observe decorrelation. However, due to the rapid repeated sampling of the same position, the MB-scan can sample fast Doppler velocities[151] without aliasing.

On the contrary, a BM-scan compares consecutive frames, thereby more efficiently utilizing the total acquisition time. With a BM-scan, the total observation time for a single location is $\sim t_2$. In Fingler et al.[151], the BM-scan was able to acquire data 200 times faster than an MB-scan of the same size. Even when using fast systems, the BM-scan may suffer from aliasing of fast Doppler velocities; however, the decorrelation rate can be obtained if the interframe time is short enough, i.e. $|r(t_1)| > 0$, and provided that t_2 exceeds the intrinsic decorrelation time.

In a logical extension of the above two scanning methods, in 2016, Wei et al.[157] proposed a volumetric optical microangiography method (**Figure 3-10C**) which used intervolume OCT scans to extract dynamic changes. The total observation time for a single location is $\sim t_3$. However, in this volumetric protocol, all information about the decorrelation rate is lost as speckles decorrelate between volumes (i.e., $|r(t_2)| \sim 0$) for

all but the slowest flows. Nevertheless, the volumetric OCTA is likely to become more prevalent as imaging speeds continue to improve[158].

3.7. Empirical Validation of OCTA

A major question in quantitative OCTA is the degree to which the measured signals are affected by the RBC speed versus density or orientation. Several authors have attempted to answer this question empirically. In 2016, Choi et al.[159] investigated the relationship between OMAG (complex difference OCTA) signals and capillary flow. They proposed an analytic model that expressed OMAG signals as a function of time interval between successive B-scan frames, particle speed, and concentration (the last two determine flux). Based on this model, they performed simulations, as well as phantom experiments, using microfluidic channels filled with diluted Intralipid solution to model blood vessels. It was shown that OMAG signal increases with flow speed within a certain range that depends on the time interval between successive B-scan frames, as expected based on **Equation (3.16)**. Furthermore, OMAG signal increased with particle concentration, but was not strictly linear. One limitation of this study is that the Intralipid solution and blood possess very different scattering properties[160,161]. Su et al.[162] used blood samples in microfluidic channels to demonstrate the relationship between SSADA decorrelation signal and the flow speed and channel width. They concluded that before saturation, the decorrelation rate was proportional to the blood flow speed when the channel width was fixed.

Even if flow velocities, channel widths, and particle/cell concentrations are realistic, controlled *ex vivo* experiments are limited in how well they can model the range of phenomena that are present *in vivo*. These include effects such as static scattering and multiple scattering involving extravascular tissue (**Figure 3-2B**), RBC orientation and transit deformation, vascular compliance, and cell-endothelium interactions. So, *in vitro* experiments may verify algorithms under model conditions, but the model might only partially capture the range of rheological and hemodynamic phenomena present *in vivo*.

One proposed *in vivo* benchmark for OCTA is fluorescence angiography (FA), which is a gold standard method for perfusion imaging[108,136]. Comparative OCTA-FA studies[108,149] have suggested that the presence of moving blood cells is a prerequisite for detection by OCTA. The threshold red blood cell density and speed required for OCTA detection are usually determined by the algorithm sensitivity. While FA shows plasma perfusion, limited depth resolution and lack of three-dimensional data and quantitative flow information make FA a less-than-ideal technique for OCTA validation.

The gold standard for single vessel hemodynamic imaging in deep tissue is multiphoton microscopy (MPM)[163,164]. In the simplest implementation, a fluorescent label is injected into the bloodstream and volumetric two-photon microscopy (TPM) is performed to acquire an angiogram. Vakoc et al.[4] showed that OCTA and two-photon microscopy angiogram morphologies correlate well for vessels larger than capillaries, and that OCTA is not confounded by dye leakage, which can impair TPM. Aside from morphology, TPM line scans enable red blood cell imaging in individual capillaries[116], measuring *in vivo* speed, flux, and linear density quantitatively. In 2012, Srinivasan et al.[9] performed OCTA and TPM line scans sequentially in the same vessels *in vivo*, showing that OCTA decorrelation rate increases with RBC speed measured by TPM. Later in 2014, Wang et al.[165] validated OMAG (complex difference OCTA) with TPM, finding no significant difference between the respective vessel densities derived from OMAG and TPM, up to the penetration depth of TPM.

When comparing OCTA and TPM, it is important to recognize that their contrast mechanisms are complementary. As OCTA measures RBC scattering and TPM measures plasma tracer fluorescence, measurements of vessel diameter must disagree in small vessels due to the plasma only, cell-free layer[103]. Moreover, typically, OCTA has a worse volumetric resolution than TPM, and asynchrony in measurements[9] can additionally confound comparisons between modalities unless physiology is carefully maintained. Thus, rigorous verification of OCTA with simultaneous TPM is a promising topic for further investigation.

The most appealing and direct validation approach is to use another OCT modality or algorithm to cross-validate OCTA. In 2012, Ren et al.[166] noticed that the passage of a red blood cell through the OCT coherence

volume led to phase and intensity transients. Based on this insight, they developed a particle counting method for measuring the flux, speed, and linear density in a capillary. Using particle counting, they developed and validated a phase intensity mapping (PIM) algorithm for measuring quantitative cerebral blood flow (CBF)[167]. It remains unclear whether individual red blood cell passage can be measured at all locations in an image, or whether these results are merely anecdotal. Moreover, the intensity pattern created by decorrelation can create random transients that could be easily mistaken for RBC passage (e.g., **Figure 3-4E** and **Figure 3-6B**). Still, particle counting remains an attractive approach for validating OCTA in stable preparations.

3.8. OCTA Measurements of Hemodynamics

Based on dynamic changes in intensity, phase, or complex signal, OCTA algorithms can distinguish dynamic tissue from static tissue. Thus, while OCTA can answer the question "where is there flow?", it cannot yet reliably answer the question "how much flow is there?". In recent years, several attempts have been made to further quantify OCTA signals. Many of these efforts are based on estimating the autocorrelation function. While the autocorrelation function can be estimated, to date, there is no rigorous theory or model for recovering RBC flow or speed from OCTA signals. Here, we summarize some promising work towards these goals.

3.8.1. Flow Quantification

In 2010, Wang et al.[10] made an early effort at providing an autocorrelation model to measure transverse particle flow speed. Though they focused on intensity transients, here we generalize their initial work. The basic principle of their model is that when particles pass through the imaging beam, they create OCT signal transients that may provide information about the speed of the underlying particles. However, with a large coherence volume, the individual transients may overlap in time. The complex signal at position (x,z) is expressed as a superposition of particle contributions:

$$S(x,z,t) = \sum_{k=1}^{G(x,z)} M_k(x,z) REC(x,z,t-t_k), \tag{3.18}$$

$$REC(x,z,t) = \begin{cases} 1, 0 \le t \le \tau_0(x,z) \\ 0, otherwise \end{cases}, \tag{3.19}$$

where k is index of the kth particle, G(x,z) is the total number of particles passing through the imaging beam within the signal acquisition period, $M_k(x,z)$ is the complex amplitude of the kth particle transient, t_k denotes the time when a particle begins to pass through the beam, and $\tau_0(x, z)$ is the position-dependent transit time of the particle.

After expressing the complex OCT signal in terms of particle contributions, the normalized autocorrelation function of S(x,z,t) is given by:

$$\frac{R(x,z,\tau)}{R(x,z,0)} = \begin{cases} 1 - \dfrac{\tau}{\tau_0(x,z)}, \tau \le \tau_0(x,z) \\ 0, \tau > \tau_0(x,z) \end{cases}, \tag{3.20}$$

where $R(x,z,\tau)$ is the autocorrelation function of S(x,z,t) with time lag τ. Note that this is equivalent to the normalized autocorrelation of REC(t). The slope of the normalized autocorrelation function in **Equation (3.20)** is proportional to the transverse speed ($\sim 1/\tau_0$). Note that **Equation (3.20)** can be further generalized to accommodate other transient shapes.

In 2012, Srinivasan et al.[9] proposed an alternative model to relate the autocorrelation to speed. For small particles undergoing isotropic motion through a coherence volume, they proposed that the autocorrelation decay is determined by axial and transverse point spread functions, while for large particles, the spatial characteristics of the particles themselves dominate the autocorrelation as described above. In Chan et al.[168], for small particles, the autocorrelation function at time lag τ in cylindrical coordinates (ρ,φ,z) is:

$$R_d(\tau) = \frac{2|K|^2}{\pi^2 w_\rho^{\,4}} \sqrt{\frac{\pi}{\left(\frac{v_\rho^{\,2}}{w_\rho^{\,2}} + \frac{v_z^{\,2}}{w_z^{\,2}}\right)}} P_A \exp\left[-\frac{(v_\rho \tau)^2}{w_\rho^{\,2}} - \frac{(v_z \tau)^2}{w_z^{\,2}}\right] \exp\left[i\left(\frac{4\pi n}{\lambda_0}\right) v_z \tau\right], \tag{3.21}$$

where w_ρ is the transverse beam profile, w_z is the axial resolution, K is an arbitrary complex constant[62], P_A is the power in the random process which describes the field, v is the particle's speed, n denotes the refractive index, and λ_0 is the central wavelength. The power spectral density, P_d, derived from the temporal autocorrelation function, is expressed as:

$$P_d(f) = \frac{2|K|^2}{\pi w_\rho{}^4 \left(\frac{v_\rho{}^2}{w_\rho{}^2} + \frac{v_z{}^2}{w_z{}^2}\right)} P_A \exp\left[-\frac{\pi^2 \left(f - \frac{2nv_z}{\lambda_0}\right)^2}{\left(\frac{v_\rho{}^2}{w_\rho{}^2} + \frac{v_z{}^2}{w_z{}^2}\right)}\right]. \quad (3.22)$$

In the presence of static scattering (**Figure 3-6**), the autocorrelation takes the form:

$$R(\tau) = R_d(\tau) + R_s(\tau), \quad (3.23)$$

where $R_s(\tau)$ is the autocorrelation of the static component, with a much longer decorrelation time than the autocorrelation of the dynamic component, $R_d(\tau)$. In practice, $R_s(\tau)$ is usually constant over time scales of interest. Aside from the Doppler shift, the un-normalized autocorrelation $R_d(\tau)$ provides two essential observables: the decorrelation rate, which is sensitive to speed, and power (P_A), which is sensitive to the RBC density. Recent work has proposed to quantify OCTA using difference algorithms measured at several time delays[169,170], providing the ability to measure blood flow speed. Since difference and correlation algorithms are related by **Equation (3.16)**, these algorithms essentially estimate the un-normalized autocorrelation. As highlighted in **Equation (3.23)**, static scattering, if present, must also be taken into account in parametric estimations based on the autocorrelation.

Finally, a major limitation of existing models is that they do not account for multiple scattering. In particular, multiple dynamic scattering events (**Figure 3-2C**, green) increase the decorrelation rate relative to the single scattering models described above, as each dynamic scattering event causes momentum transfer[171]. In such cases, the decorrelation rate depends on the number of scattering events, which in turn is impacted by the RBC density. Thus, with multiple intravascular scattering events, decorrelation rate is not a "pure" metric of speed. Therefore, decorrelation rate is not a good metric of speed within macrovessels

where multiple scattering dominates, but may perform better in capillaries where hematocrits are lower and singly backscattered light prevails (**Figure 3-2B**).

3.8.2. Hematocrit Quantification

Since OCTA signal depends on the RBC density, can OCTA be used to quantify hematocrit? The differences in rheology, geometry, and light scattering in capillaries versus macrovessels suggest different approaches for each. In macrovessels, backscattering or attenuation (signal slope) are possible observables which may help to determine hematocrit. However, due to the high scattering coefficient and anisotropy of RBCs, multiple scattering events are very likely, except at superficial path lengths (**Figure 3-2C-D**). In particular, at physiological hematocrits, dependent scattering and shadowing effects lead to a highly nonlinear relationship between the RBC concentration and scattering coefficient[172,173]. This nonlinear relationship hampers efforts at quantifying hematocrit based on light scattering and the signal slope alone. Additionally, the oxygen saturation dependence of hemoglobin refractive index and RBC scattering further complicate efforts to measure hematocrit based on attenuation[121]. The orientation-dependence of light scattering from RBCs (**Figure 3-2C**) makes quantifying hematocrit from backscattering alone challenging. Thus, quantification is challenging in macrovessels.

The single file flow and relatively lower hematocrit in capillaries makes multiple scattering within these vessels less problematic. However, RBCs may re-orient themselves and possibly deform as they squeeze through the smallest diameter capillaries, thereby changing their backscattering cross-sections. Moreover, measuring backscattering directly would need absolute calibration, which can be difficult *in vivo*. However, backscattering may still measure relative changes in the red blood cell content in capillaries[174] and, possibly, at the surfaces of macrovessels over time. Thus, while quantification of hematocrit changes is possible in capillaries, absolute measurements of hematocrit with conventional OCTA are currently challenging.

3.9. Can OCTA Be Made a Quantitative Tool?

OCTA systems can observe dynamic signal power (variance) and decorrelation rate[10,175], based on the dynamics of light scattering. As algorithms, imaging system performance, and motion tracking/compensation continue to improve, OCTA observables, particularly decorrelation rate, can be precisely and accurately measured. These observables may generate useful diagnostic information, even if their underlying hemodynamic correlates remain unclear. However, if OCTA observables can be directly linked to hemodynamic parameters such as blood flow, volume, hematocrit, and speed, OCTA diagnostics could aid understanding of pathogenesis. This effort requires an appropriate model to describe OCTA signals. The model may be empirical (**Section 3.7**), but ideally, should have a theoretical foundation (**Section 3.8.1**). Current theoretical models are very simple, and only account for single scattering[9,10,175,176]. Improvements in OCTA theory to include multiple scattering[177] and orientation effects[99] are needed. Empirical models have been developed for flow phantoms[159], but they may be limited to *in vitro* conditions, and their applicability *in vivo* remains uncertain. Better *in vivo* validation experiments, perhaps in well-controlled and stable animal preparations, are needed. Last, due to differences in light scattering and hemodynamics (**Figure 3-1** and **Figure 3-2**), models for capillaries and macrovessels must be developed independently.

In spite of these proposed efforts, the inherent complexity of the rheology and light transport in microvasculature may prevent reliable quantification of OCTA. Therefore, we propose that alternative optical properties (aside from light scattering) may enable more quantitative OCTA. For instance, visible light OCTA[51] enables direct absorption-based measurements of hemoglobin concentration, which is expected to correlate well with hematocrit (RBC volume fraction) under most conditions[17]. Yet another way to circumvent the pitfalls of RBC scattering is to introduce an exogenous contrast agent with more desirable scattering properties into the bloodstream[178]. If a more isotropically scattering contrast agent such as Intralipid®[64,179] is used, angiograms derived from the contrast agent signal alone do not suffer from multiple scattering tails[64,179]. Microbubbles[180,181] are promising for enhancing intravascular scattering signals, and may present more well-defined decorrelation characteristics than blood. Moreover, if the

contrast agent behaves like plasma and the signal can be calibrated and related to concentration[64,179], plasma flow, transit time, and volume can all be measured.

Despite recent strides in OCTA imaging speed, field-of-view, and measurement of OCTA observables, OCTA remains a qualitative tool at present. The obstacles to quantification include the irregular shape of RBCs, the consequent orientation-dependence of RBC backscattering, and the high anisotropy of the RBC scattering phase function, which leads to multiple scattering in large vessels. Quantification of OCTA signals can be achieved only through a rigorous understanding of the relationship between hemodynamics, rheology, and light scattering of RBCs. Improvements in theoretical models, validated in microvasculature *in vivo* against gold standard techniques and possibly in simulation, may help to improve this understanding. Finally, alternative measurements, based on absorption or exogenous contrast agents, may help to alleviate some of the confounds associated with RBC scattering and enhance the quantitative information provided by OCTA. More quantitative interpretation of OCTA would aid the application of this promising technique to study pathophysiology, and also potentially enhance the clinical impact of OCTA, making this endeavor well worth the effort.

3.10. Experimental Investigation of Visibility of Microvessels with OCTA

3.10.1. Animal Experiments and Data Acquisition

One Sprague-Dawley (#1) and two Long-Evans (#2, #3) rats (male, 8 weeks, Charles River) were imaged under isoflurane anesthesia by an OCTA ophthalmoscope with a center wavelength of 1300 nm, an axial resolution of 5.2 μm in tissue, and a $1/e^2$ beam diameter of 1.1 mm on the pupil[54]. Intralipid-20% (IL-20), a highly scattering fat emulsion which can serve as a plasma tracer[179], was injected intravenously via the tail vein (3 mL/kg)[178,179]. RBCs form the largest cellular component of blood by volume and are assumed to account for most of the intrinsic OCTA signal. Unlike RBCs, Intralipid particles are spherically symmetric, and do not produce orientation-dependent OCTA signal[54]. Volumes were acquired both before injection and at steady state (3-4 minutes after injection), at an A-scan rate of 91 kHz with 1500 axial scans

at 1500 y-locations with 3 repeats per y-location, over a 2.9 mm (X) by 2.9 mm (Y) field. This protocol enabled us to compare OCTA images before and after contrast enhancement, by analyzing an enhancement factor (EF), to characterize the orientation-dependent OCTA signal. All animal experimental procedures and protocols were approved by the Institutional Animal Care and Use Committee at UC Davis.

3.10.2. OCT Angiogram Processing

OCTA was performed by complex OCT signal subtraction, with subsequent angiogram intensity averaging[5]. Angiograms were then layer segmented. For the choriocapillaris, the OCT angiogram data was masked with a Gaussian function in the axial direction, centered on the choriocapillaris, with a width approximately equal to the choriocapillaris layer thickness. Angiograms were weighted by the similarly masked OCT intensity data (i.e. the conventional OCT image)[5]. Then, the mean value of the weighted angiogram along the axial direction was taken as the *en face* projection. For the inner retina, a maximum intensity projection (MIP) of the angiogram was taken along the axial direction as the *en face* projection. For the enhancement factor analysis (see below), which focused on the inner retina, the background was corrected by subtracting the mean value of the lowest 20 percent of voxels in the inner retina.

3.10.3. Vessel Angle Calculation

To investigate the relationship between tracer vessel enhancement and vessel orientation in the inner retina, angiograms were processed using the Frangi filter[182,183]. Vesselness, a voxel-wise metric of likeness to a vessel lumen, was calculated in three dimensions (3D). Vessel orientation was determined by multi-scale eigen-decomposition of the local Hessian matrix, which yielded three eigenvalues (λ_1, λ_2 and λ_3) for each angiogram voxel, with $|\lambda_1| \leq |\lambda_2| \leq |\lambda_3|$. Eigenvector $\mathbf{v_1}=[v_{1x},v_{1y},v_{1z}]$, which corresponds to eigenvalue λ_1, was regarded as the local vessel orientation, where the orientation angle relative to the incident beam (Θ_Z,

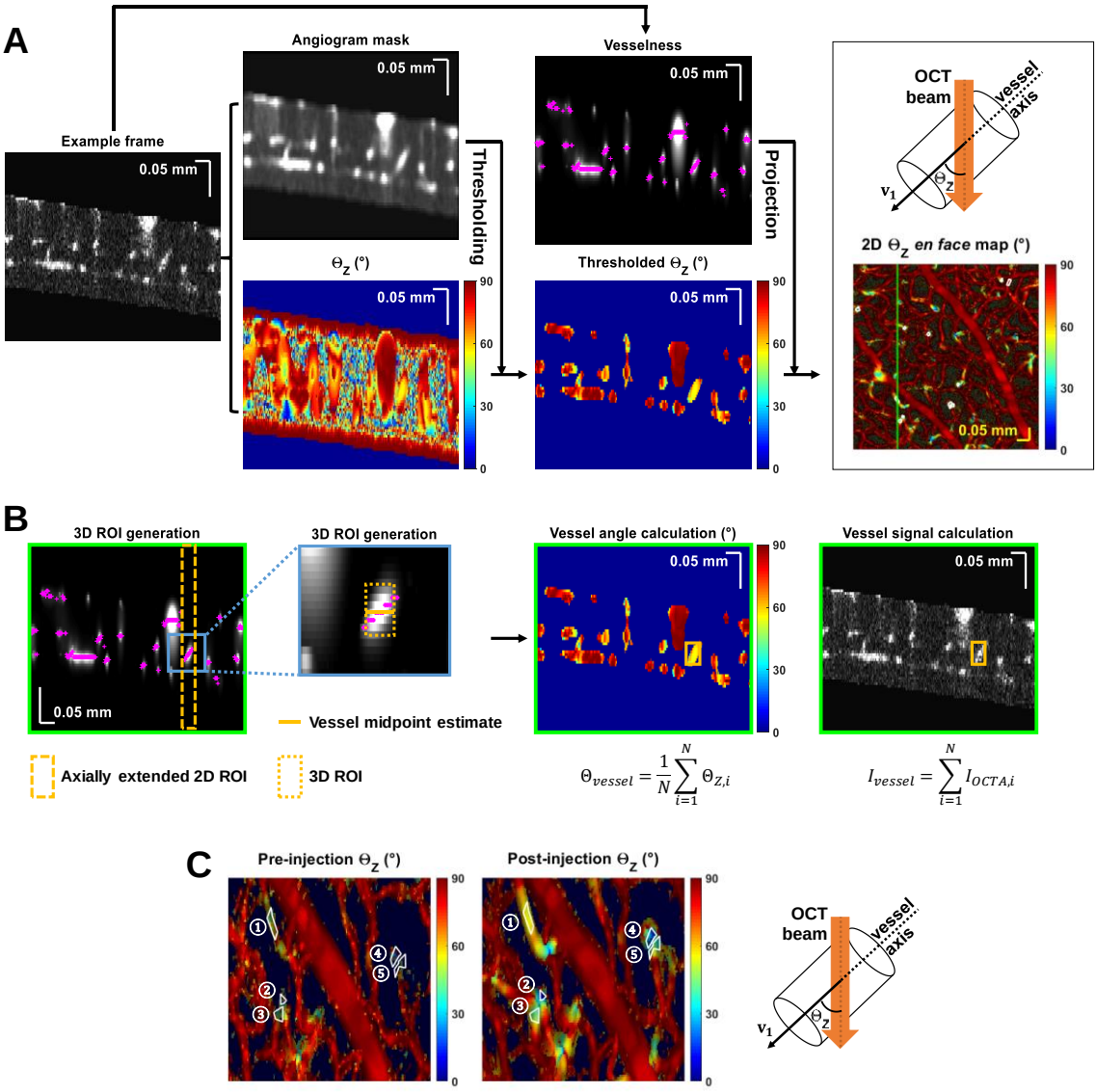

Figure 3-11. Data processing. (A) 2D Θ_Z *en face* map generation. An example frame from the inner retina angiogram volume is shown, after background correction and elimination of non-inner retinal tissue. The volume is blurred to generate the angiogram mask volume, eigen-decomposed to generate vessel orientation relative to the incident OCT beam, Θ_Z, and Frangi filtered to generate the vesselness volume. Vessel angle Θ_Z (top right) is defined as the angle between OCT incident beam (Z axis) and vessel axis (eigenvector). The Θ_Z volume is thresholded by the angiogram mask volume to remove static tissue. Θ_Z values at maximum vesselness locations (magenta crosses) are projected to create the 2D *en face* (X and Y) Θ_Z map. A 2D ROI (white polygon), selected from the *en face* Θ_Z map (A), is then converted to a 3D ROI. (B) Starting from the vesselness frames, the axial positions (magenta crosses) of the maximum vesselness values within the 2D ROI are averaged to estimate the vessel midpoint (gold line). Then, a 7 pixel range (+/- 3 pixels, ~25.8 µm, gold box) centered on this midpoint, is used as the depth (Z) range for the final 3D ROI (the original 2D ROI delimits the 3D ROI in X and Y). Within this 3D ROI, thresholded Θ_Z and angiogram values for each voxel (indexed by i) are averaged and summed, respectively, to yield the vessel orientation (Θ_{vessel}) and vessel signal (I_{vessel}). (C) Zoom showing corresponding 2D ROIs on pre- and post-injection *en face* Θ_Z maps.

Figure 3-11A top right) was calculated as $\Theta_Z=\cos^{-1}(|v_{1z}|/|\mathbf{v_1}|)$. Note that Θ_Z is noisy in regions with low OCTA signal (static tissue); therefore, Θ_Z volumes were thresholded based on a blurred angiogram mask

to confine analysis of Θ_Z values to vessel lumens (**Figure 3-11A**).

3.10.4. Quantifying a Tracer-referenced RBC Signal through the Enhancement Factor

In order to quantify RBC-specific OCTA signal in microvessels of varying orientation, an enhancement factor due to Intralipid was extracted from individual microvessels in the inner retina. Specifically, two dimensional (2D) regions of interest (ROIs), shown as white polygons in **Figure 3-11A**, were drawn to select vessels from 2D Θ_Z *en face* maps, which displayed Θ_Z values at maximum intensity locations (Z, magenta crosses in **Figure 3-11A**) of vesselness at each (X, Y) coordinate. Next, the 2D ROIs were converted to 3D ROIs. First, the average of the MIP depths across the 2D ROI was designated as the vessel midpoint. Next, the 2D ROI was extended axially 3 pixels above and below the midpoint (7 pixels in total, corresponding to ~25.8 μm) to create a 3D ROI (**Figure 3-11B**). Vessel signal (I_{vessel}) within the 3D ROI was obtained by summing the background corrected angiogram over all voxels, and vessel orientation (Θ_{vessel}) was obtained by averaging thresholded Θ_Z over all voxels. Identical 2D ROIs at corresponding locations were selected in pre- and post-Θ_Z *en face* maps (**Figure 3-11C**). The raw enhancement factor (EF_{Raw}), defined as the ratio of the post- ($I_{vessel,Post}$) to pre- ($I_{vessel,Pre}$) injection vessel signal, was computed:

$$EF_{Raw} = \frac{I_{vessel,Post}}{I_{vessel,Pre}}. \tag{3.24}$$

To remove EF modulation due to floater shadowing or alignment changes that were not a direct consequence of the injection, the raw enhancement factor was then locally normalized by a "reference" OCT inner retinal intensity (I_{ref}) ratio:

$$EF = EF_{Raw}\frac{I_{ref,Pre}}{I_{ref,Post}} = \frac{RBC + Tracer}{RBC}. \tag{3.25}$$

The "reference" inner retinal intensity was assumed to represent mostly nonvascular tissue, whose intrinsic reflectance is not expected to change after injection. After this normalization, we assumed that the enhancement factor provided an accurate relative measurement of backscattering after and before the injection. The EF was plotted versus vessel angle to assess the impact of orientation on microvessel

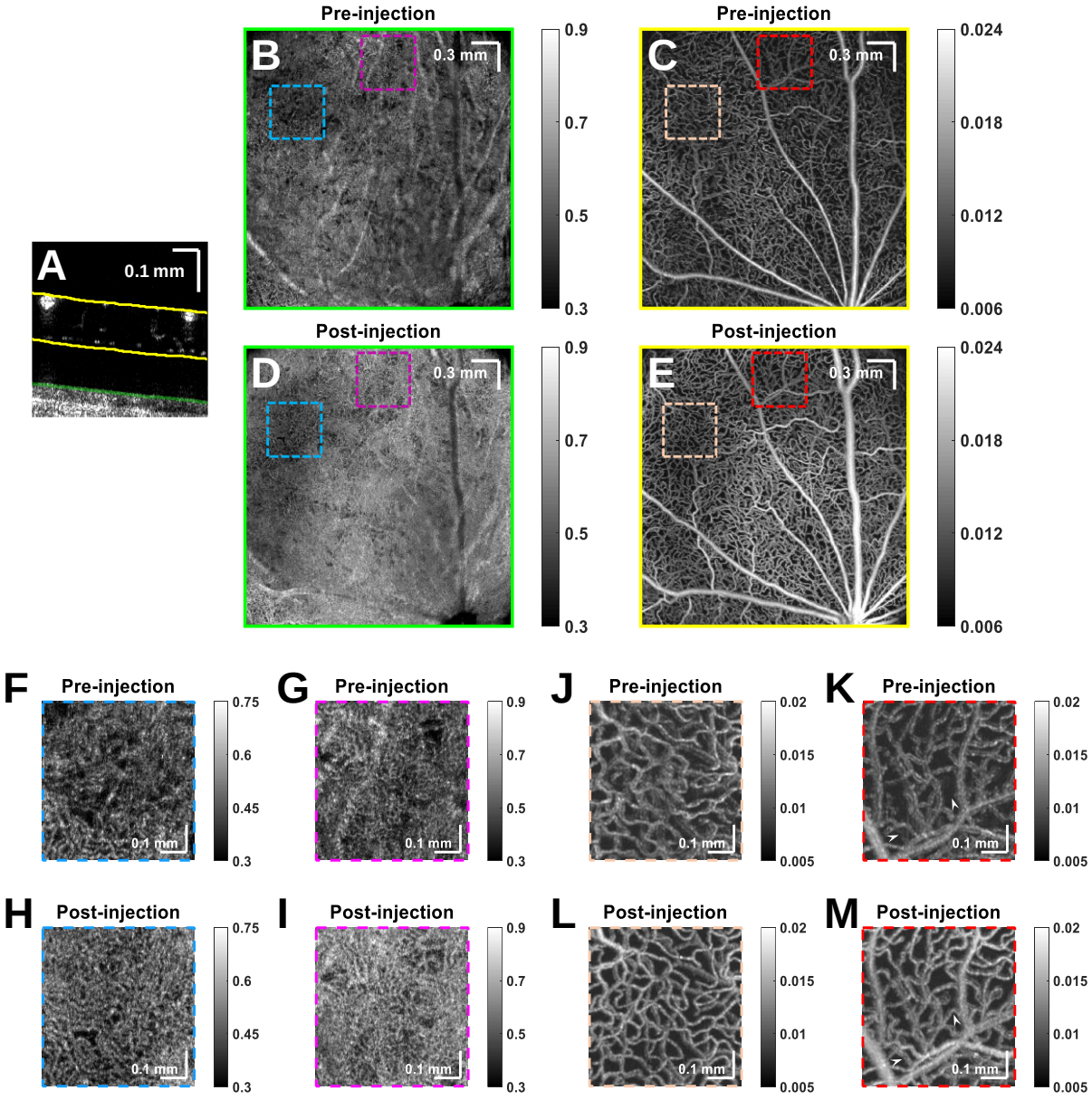

Figure 3-12. Tracer injection improves visualization of microvessels. OCTA depicts the choriocapillaris and retinal microvasculature (projection depths shown in A) in rat #1 before (B, C) and after (D, E) Intralipid tracer injection, respectively. Comparison of choriocapillaris (F-I) and inner retina (J-M) before and after injection. Arrowheads point to microvessels that are only visualized after Intralipid tracer injection.

visibility in OCTA. To directly assess the ratio of RBC and tracer signals, an RBC-to-tracer backscattering signal ratio was computed as follows and plotted versus vessel angle:

$$\frac{RBC}{Tracer} = \frac{1}{EF - 1}. \tag{3.26}$$

3.10.5. Tracer Injection Aids Visualization of Retinal and Choriocapillary Microvessels

OCTA images of the choriocapillaris and inner retina (with projections based on segmentation lines in **Figure 3-12A**) of rat #1 before (**Figure 3-12B-C**) and after (**Figure 3-12D-E**) Intralipid tracer injection are shown. Detailed comparisons of regions of choriocapillaris and the inner retina (delimited by colored boxes) are shown in **Figure 3-12F-I** and **Figure 3-12J-M**. Note that dynamic range varied for **Figure 3-12B-M**, but remained consistent between pre- and post-injection images.

Though not the focus of our study, we first remark on the choriocapillaris. Clearly, the overall choriocapillaris signal increased after the injection. While in some regions, more vasculature was visualized (**Figure 3-12F** and **H**), in others, vasculature was less clearly delineated (**Figure 3-12G** and **I**). Differences between RBC and plasma perfusion, physiological changes, and segmentation differences may all contribute to these divergent observations. We also cannot exclude the possibility of extravasation of smaller tracer particles from the fenestrated choriocapillaris.

In the inner retina, the main focus of this study, signal from microvessels increased after the injection and remained well-localized to the lumen (**Figure 3-12J-M**). Upon close inspection, some microvessel segments which lacked signal prior to injection were visualized only after the injection (**Figure 3-12K** and **M**, arrowheads).

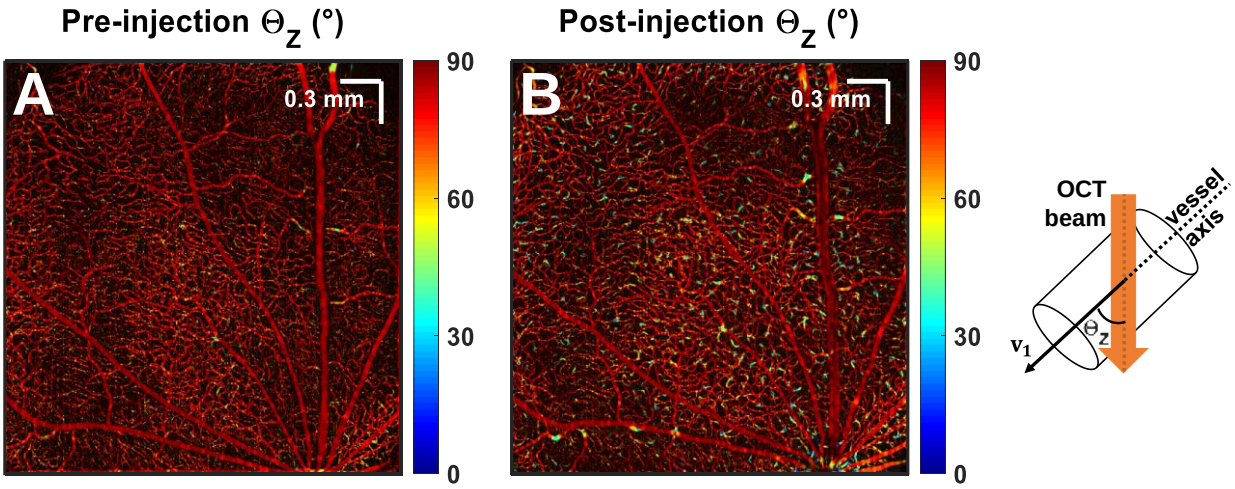

Figure 3-13. Tracer injection reveals more ascending or diving vessels in inner retina. Vessel orientations relative to the OCT incident beam are color-coded and shown pre- (A) and post- (B) Intralipid injection. Angles range from 0° (parallel to the incident beam) to 90° (perpendicular to the incident beam).

3.10.6. Tracer Injection Reveals Connecting (Ascending or Diving) Vessels in Retina

To assess the orientation dependence of the OCTA signal on RBC back scattering, microvessel angles were color-coded from Θ_Z=0° (parallel to the incident OCT beam) to 90° (*en face*), and shown before and after Intralipid injection (**Figure 3-13**). Microvessels mainly lie in *en face* laminae (red), while diving or ascending microvessels connect layers (yellow and blue). Importantly, connecting vessels were better visualized after Intralipid injection, and some were only seen afterwards (i.e. they were below the noise level before injection).

3.10.7. Vessel Angular Orientation Determines Angiogram Enhancement

Enhancement factor was assessed versus microvessel angle to quantify the observations in the previous section. For all rats, enhancement factor consistently increased with decreasing vessel angle relative to the incident light (**Figure 3-14A-C**). Specifically, for rat #1, EF was ~2.0 for an ~80° vessel angle, and increased to ~5.0 for a 20-30° vessel angle. For rat #2 and #3, EF increased from 1.5 to 2.3, and 1.6 to 3.3,

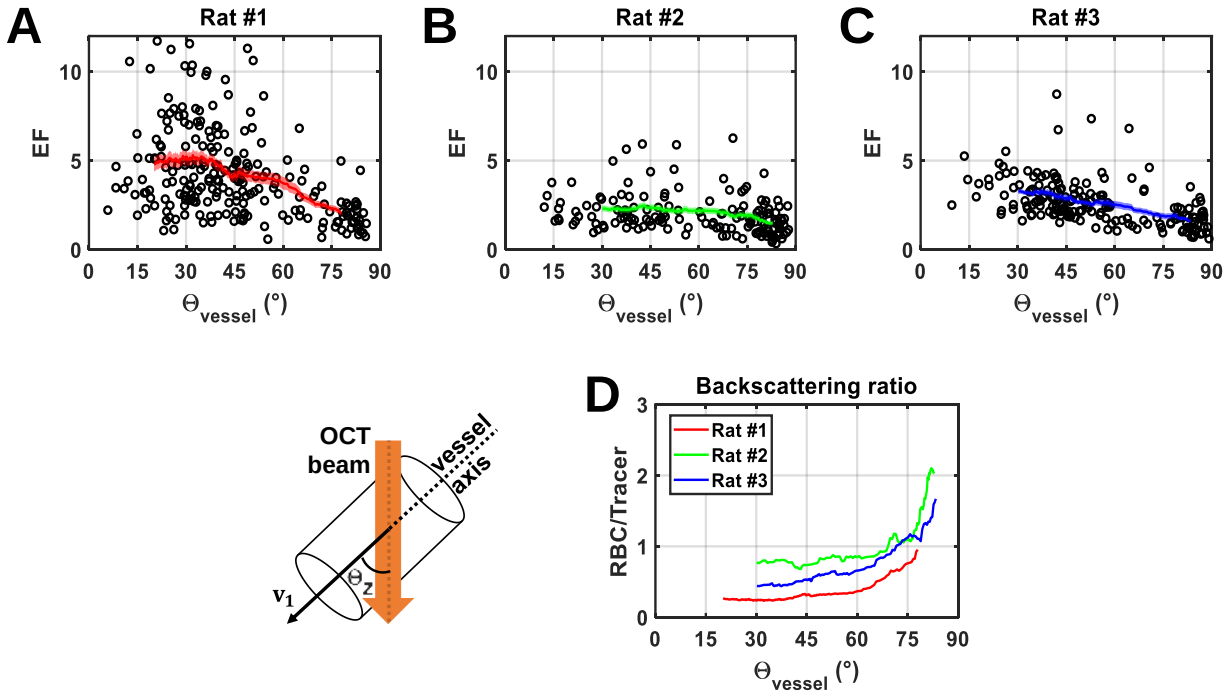

Figure 3-14. Vessel angular orientation determines angiogram enhancement. (A-C) Enhancement factor versus vessel orientation. The line in each panel depicts a rolling average over 45 angles, and the shaded area represents the corresponding standard error. (D) RBC-to-tracer backscattering ratio changes with vessel orientation are consistent across animals.

respectively, for a similar decrease in angle. Consequently, the RBC-to-tracer backscattering ratio [**Equation (3.26)**] also increased with vessel angle (**Figure 3-14D**). Assuming equal concentration of Intralipid filled vessels at different orientations and no RBC shadowing effects, the increased backscattering ratio indicates that ascending or diving microvessels have less "intrinsic" OCTA RBC signal than *en face* microvessels. The absolute RBC-to-tracer ratio differs between rats, likely due to variable dosages and imaging time points relative to the injection. However, trends with microvessel angle are consistent across animals (**Figure 3-14D**). Based on the backscattering ratio, assuming tracer contributions are independent of angle, our results imply signal from RBCs in 80-90° vessels is 3.4 ± 0.6 (mean ± standard deviation) times that of 20-30° connecting vessels.

3.10.8. Discussion and Conclusion

Ascending and descending microvessels connecting laminae are rarely visualized[183] and have not been rigorously studied with OCTA. Our results suggest that the orientation of these microvessels with respect to the incident light may render them intrinsically more challenging to visualize with intrinsic contrast in OCTA.

To show our results in the context of previous findings[64] and to provide a physical explanation, we refer to **Figure 3-15**, which overlays signal contributions of tracer (green) and RBCs (red) in cross-section (**Figure 3-15D**). In the macrovessels, as previously described, RBCs align with respect to the shear direction, orienting their flat face parallel to the vessel wall[99]. The orientation dependence of RBC backscattering leads to higher signal at the top and bottom of vessels relative to the sides. Intralipid tracer particles are ~3000-5000 times smaller by volume, on average, and spherically symmetric[54,184], leading to relatively orientation independent tracer backscattering. This explains the hourglass appearance of macrovessels; red (dominated by RBC backscattering) on top and bottom transitioning to green (dominated by tracer backscattering) on the sides, as described previously[64].

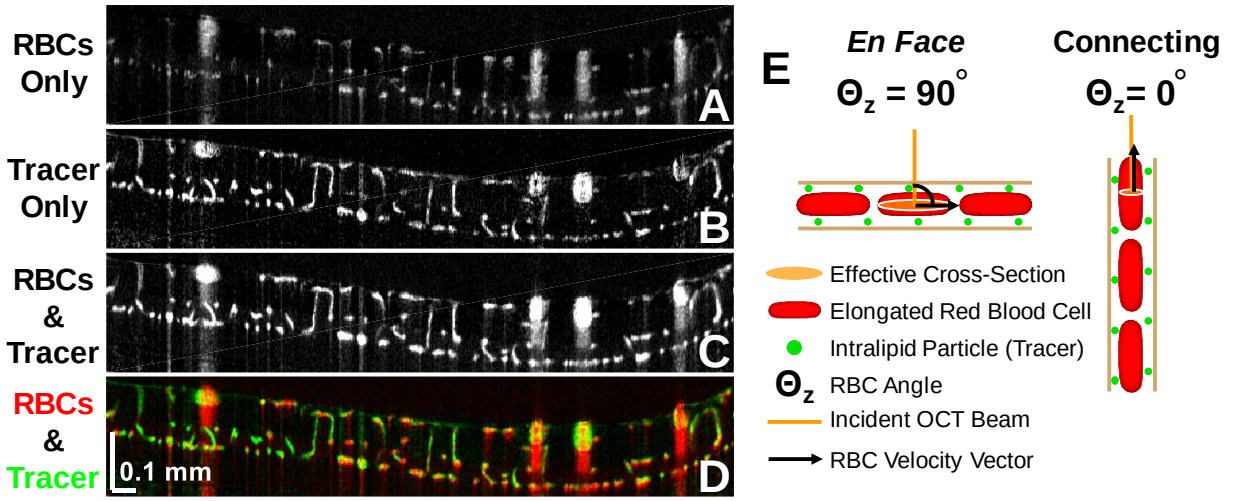

Figure 3-15. Visual summary (A-D) and proposed explanation (E) for study results. (A-D) After Intralipid injection, signals in connecting microvessels are preferentially enhanced, as shown in overlay (D) of signal contributions from RBCs (red) and Intralipid tracer (green). (E) Intralipid particles are smaller than RBCs and spherically symmetric. Thus, Intralipid backscattering in OCTA does not depend on microvessel orientation, and Intralipid signal serves as a convenient reference. We propose that longitudinal RBC elongation contributes to the lower relative RBC signal in connecting microvessels. Due to this elongation, incident light sees a smaller effective cross-section for RBCs in diving or ascending microvessels than for RBCs in *en face* capillaries, resulting in relatively less OCTA signal.

Turning attention to the inner retinal microvessels, the focus of the present study, the overlay illustrates that connecting vessels (green) enhance more than *en face* capillaries (red and yellow). Assuming no differences in tracer signal, these vertical microvessels must possess less baseline OCTA signal. We propose that this microvascular finding is also explained by the orientation dependence of RBC backscattering, though the rheological explanation for RBC deformation in microvessels is different from that of macrovessels. In microvessels, theoretical[185] and experimental[186,187] studies have shown that RBCs elongate longitudinally. Therefore, we propose that RBCs in connecting microvessels present a smaller effective cross-section to the incident light than RBCs in perpendicular microvessels (**Figure 3-15E**), resulting in lower backscattering and rendering these vessels less visible in OCTA. Thus, while some microvessels connecting laminae can be detected by intrinsic contrast OCTA (**Figure 3-13A** and **Figure 3-15A**), these diving or ascending microvessels are generally less visible than *en face* capillaries (**Figure 3-14A-C**) and more likely to fall below the OCTA detection limit (**Figure 3-15A and D**). Increased averaging[183,188] could help in visualizing these vessels.

Across rats (**Figure 3-14A-C**), different absolute EF values and RBC-to-tracer signal ratios are observed. This might be due to differences in Intralipid tracer dosages, or variable elapsed time between injection and post-injection data acquisition. However, allowing for potential differences in baseline tracer signal, the RBC-to-tracer signal ratio changes with vessel angle were remarkably consistent between animals. For a given animal, we assume that the tracer can serve as an orientation independent reference to quantify orientation dependent RBC signal (**Figure 3-15E**). Thus, we attribute 2.8- to 4-fold higher RBC-to-tracer signal ratio at large angles relative to small angles to differences in RBC backscattering. The Born approximation, which relates the scattering amplitude to the Fourier transform of the scattering potential, implies that an oblong scattering particle should be oriented perpendicular to the incident light to maximize backscattering[189]. Finite difference time domain simulations should be performed in the future to provide more accurate orientation-dependent backscattering calculations for elongated RBCs.

While this work is primarily intended to draw attention to the orientation dependence of OCTA signal from RBCs, it also suggests potential approaches to overcome this problem. The most obvious approach, employed here, is tracer injection. If tracer injection is not possible, more aggressive averaging strategies might detect weak RBC backscattering signal in vertical vessels[183]. Yet another potential solution is multi-angle illumination and detection[190].

Finally, we note that while orientation dependence of RBC backscattering can explain our observations (**Figure 3-14A-C**, **Figure 3-15A** and **D**), hematocrit differences and sporadic RBC flow through capillaries may also contribute. In fact, in a different study[191] we attributed enhancement factor differences among different microvessel populations, all with similar angular orientation distributions, to haematocrit differences. Of note, we found no evidence either for or against hematocrit differences (or variations in any hemodynamic parameter, for that matter) in interlaminar and intralaminar retinal vessels in the literature. Another limitation of this study is the ROI selection bias; only ROIs with sufficiently high signals in both pre- and post-injection data were selected, which rules out small angle connecting vessels that only show up after injection. However, we hypothesize that inclusion of such high enhancement factor vessels at small

angles would actually have strengthened the main study conclusion. Other limitations of this study are the longer OCTA wavelength compared to clinical practice, isoflurance anesthesia, and differences in RBC size, microvessel diameter, and rheology between rats and humans.

In spite of these limitations, this study clearly demonstrates and quantifies the orientation dependence of microvessels in OCTA for the first time. This orientation dependence should always be considered when interpreting OCTA in ophthalmology.

3.11. Acknowledgements

We acknowledge support from the National Institutes of Health (EB023591, AG010129, NS094681. NS105043, EY028287 and EY030361) and the Glaucoma Research Foundation Catalyst for a Cure. The "Experimental Investigation of Visibility of Microvessels with OCTA" section was conducted jointly with equal contribution with Mr. Marcel T. Bernucci.

Chapter 4 1700 nm optical coherence microscopy enables minimally invasive, label-free, *in vivo* optical biopsy deep in the mouse brain

4.1. Abstract

In vivo, minimally invasive microscopy in deep cortical and sub-cortical regions of the mouse brain has been challenging. To address this challenge, we present an *in vivo* high numerical aperture optical coherence microscopy (OCM) approach that fully utilizes the water absorption window around 1700 nm, where ballistic attenuation in the brain is minimized. Key issues, including detector noise, excess light source noise, chromatic dispersion, and the resolution-speckle tradeoff, are analyzed and optimized. Imaging through a thinned-skull preparation that preserves intracranial space, we present volumetric imaging of cytoarchitecture and myeloarchitecture across the entire depth of the mouse neocortex, and some sub-cortical regions. In an Alzheimer's disease model, we report that findings in superficial and deep cortical layers diverge, highlighting the importance of deep optical biopsy. Compared to other microscopic techniques, our 1700 nm OCM approach achieves a unique combination of intrinsic contrast, minimal invasiveness, and high resolution for deep brain imaging.

4.2. Introduction

Central nervous system (CNS) diseases such as Alzheimer's disease (AD) manifest early at the microscopic (i.e. cellular) level[192,193] deep in the brain. However, high-resolution, *in vivo* brain imaging has been a long-standing challenge. Macroscale imaging techniques such as magnetic resonance imaging (MRI) and positron emission tomography (PET) enable structural and functional imaging at the whole brain level[194,195]. However, achievable PET resolution is limited to the millimeter or sub-millimeter scale[196,197], and cellular resolution is not yet feasible in MRI[198]. Optical methods such as multi-photon microscopy (MPM) can achieve micron-scale resolution[192,199], which facilitates cellular imaging, but usually require exogenous fluorescence labeling or transgenic models. Additionally, the signal-to-background ratio of MPM degrades

in deep tissue. Imaging of deep cortical layers with two-photon microscopy, even via invasive cranial windows, is challenging[200]. Three-photon microscopy improves upon the signal-to-background ratio of two-photon microscopy[201] and provides sub-cortical imaging through invasive cranial windows[202] and mid-cortical imaging through the intact skull[203]. Optical coherence microscopy (OCM), which is a label-free imaging technology based on backscattered light, images cellular architecture up to layer V in the rodent brain at 1300 nm[60] through an invasive cranial window. Yet, invasive preparations that remove overlying turbid tissue such as the skull and dura enable imaging deeper, but significantly perturb brain physiology[204,205]. The goal of cellular-level imaging in the deep cortical layers and beyond, through a minimally invasive preparation, remains elusive.

With this goal in mind, here we design and demonstrate the first OCM system for *in vivo* imaging of brain cellular architecture in the 1700 nm optical window, where ballistic attenuation in the brain is minimal[41,76,81,82,202]. Technical challenges of this emerging wavelength range are addressed through the system design, including the choice of light source, dispersion compensation method, and optical components. Coherence gating is shown to complement confocal gating[206], while post-processing is optimized to reduce speckle while also rejecting multiply scattered light. Cytoarchitecture and myeloarchitecture are imaged across the neocortex and some sub-cortical regions, through a minimally invasive, thinned-skull surgical preparation. Laminar variations in neuropathology are investigated in a mouse model of Alzheimer's disease, with corresponding histology for comparison. Amongst approaches to study neuropathology in the living, intact brain, 1700 nm OCM provides a unique combination of label-free, minimally invasive, deep, and high-resolution imaging.

4.3. Methods and Materials

4.3.1. System Design and Characterization

As shown in **Figure 4-1A**, light from a near-infrared (NIR) supercontinuum light source (L15077-C7-Y001, Hamamatsu, Corp., NJ, USA) is split into reference and sample arms by a 50/50 SMF-28 customized fiber

coupler (Haphit, Inc., Shanghai, China). In both arms, the beam is collimated by a 15 mm effective focal length (EFL) reflective collimator (RC04APC-P01, Thorlabs, Inc., NJ, USA). In the sample arm, the beam is scanned by a 2D galvanometer (6215H, Cambridge Technology, Inc., MA, USA), magnified by a scan lens and tube lens pair (SL50-3P & TL200-3P, Thorlabs, Inc.), and then focused onto the sample using a high numerical aperture (NA) water immersion objective (XLPLN25XWMP2, Olympus America, Inc., PA, USA). Sample translation is controlled by motorized stages in the transverse (X, Y, ILS50CC, Newport, Corp., CA, USA) and axial (Z, L-310, Physik Instrumente, L.P., MA, USA) directions. In the reference arm, the beam is magnified by two pairs of achromatic doublets (Thorlabs, Inc.), with 50 mm and 75 mm EFL. A glass block approximately matches dispersion in the sample arm and an adjustable iris controls reference power. The backscattered light from the sample and light reflected from the reference mirror are then combined by the fiber coupler and delivered to the spectrometer. In the spectrometer, light is collimated by an air-spaced achromatic doublet (ACA254-075-D, Thorlabs, Inc.), dispersed by a custom 1700 nm diffraction grating (600 lines per millimeter, Wasatch Photonics, Inc., UT, USA), focused by an achromatic doublet (150 mm EFL, Thorlabs, Inc.), and detected by an extended InGaAs line scan camera (SU1024LDH-2.2RT, Sensors Unlimited, Inc., NJ, USA). Data were collected via the frame grabber (PCIE-1427, National Instruments, Corp., TX, USA). Sensitivity roll-off and axial resolution degradation are insignificant over the first millimeter depth, which suffices for high NA, short depth-of-field, imaging (**Figure 4-2A-B**). The camera and 2D galvanometer scanner were synchronized using a custom LabVIEW program. As described in the subsequent sections, the system design was tailored to maximize sensitivity through reducing source excess noise and improving spectrometer efficiency, while minimizing aberrations and dispersion.

4.3.1.1. Reduced excess noise

To take full advantage of the entire 1700 nm water absorption optical window, which extends beyond the cutoff of standard InGaAs, an extended InGaAs camera was employed for detection. However, due to lattice mismatch, extended InGaAs exhibits higher detector noise than standard InGaAs. The elevated detector

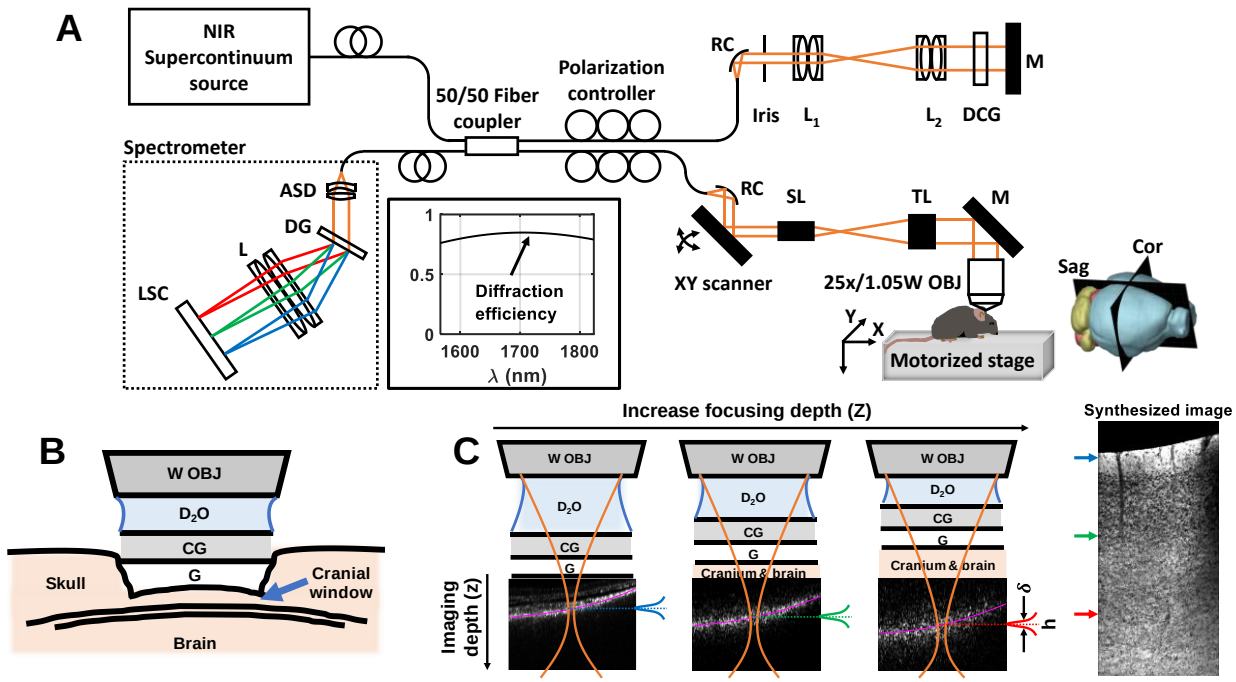

Figure 4-1. System design and experimental setup. (A) Schematic of the 1700 nm OCM system. RC: reflective collimator; $L_{1/2}$: lens (achromatic doublet pairs) in the reference arm; DCG: dispersion compensation glass; M: mirror; SL: scan lens; TL: tube lens; 25x/1.05W OBJ: 25x, NA 1.05 water immersion objective; Sag/Cor: sagittal/coronal plane; ASD: air-spaced doublet; DG: diffraction grating; L: lens; LSC: line scan camera. The 3D mouse brain rendering was obtained from the Brain Explorer 2 software (http://mouse.brain-map.org/static/brainexplorer). Inset (black box) shows the diffraction efficiency of the customized grating over the system spectral band. (B) Preparation for thinned-skull imaging. W OBJ: water immersion objective; D_2O: heavy water immersion medium; CG: cover glass; G: glue. (C) Dynamic focusing and image synthesis. The sample is translated stepwise towards the objective. As the focus translates deeper into the brain, the cranium and brain replace the immersion medium in the light path. The axial weighting function h, with width δ, multiplies each volume prior to image fusion and display.

noise, in conjunction with excess light source noise, compromises the ability to achieve shot noise limited (SNL) sensitivity[43]. To maximize the system sensitivity, three commercial prototype supercontinuum light sources (#1: Source 1; #2: SuperK Extreme, NKT Photonics, Inc., MA, USA; #3: L15077-C7-Y001, Hamamatsu Corp.) were characterized and compared (**Figure 4-2C**). The first two were photonic crystal fiber (PCF) based broadband supercontinuum sources, while the third was a Hamamatsu prototype, in which a pulse centered at 1690 nm was filtered from multiple soliton orders after fission in a single mode fiber, followed by further spectral broadening by self-phase modulation in a normal dispersion highly nonlinear fiber[207]. The repetition rates of the two PCF-based supercontinuum sources were 40 and 78 MHz, while the repetition rate of the Hamamatsu source was 50 MHz. The Hamamatsu source was found to

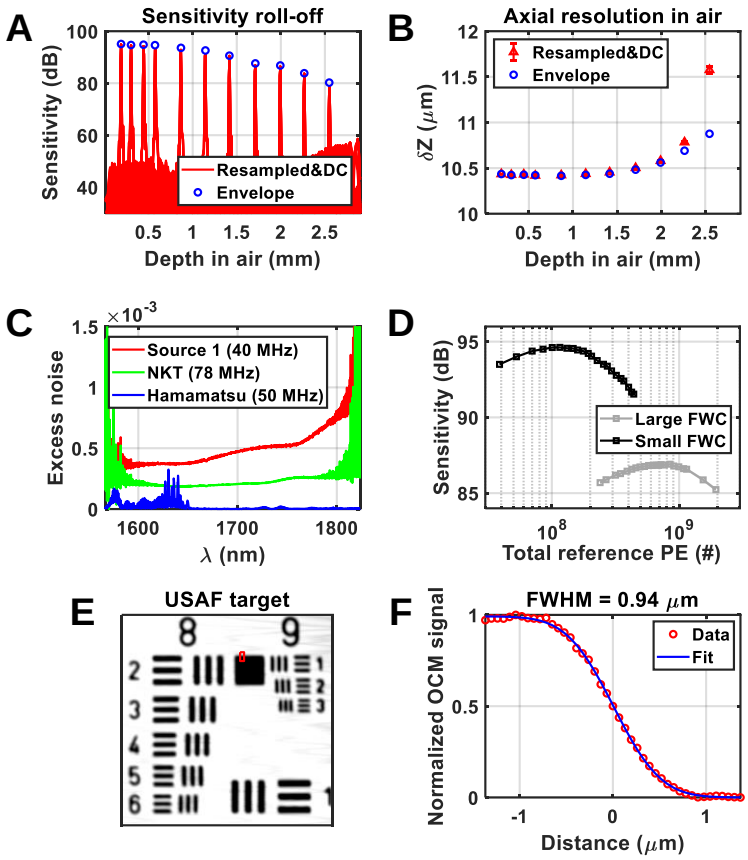

Figure 4-2. 1700 nm OCM system characterization. (A) Sensitivity roll-off and (B) axial resolution versus depth. To assess efficacy of resampling and dispersion compensation (DC), results (red) are compared with theoretical values from the envelope (blue circles). (C) Excess noise coefficient measurements of three light sources. (D) System sensitivity using Hamamatsu light source with large (12.5 Me^-) / small (1.25 Me^-) full well capacity (FWC) camera settings. (E) *En face* image of groups 8 and 9 of a negative USAF 1951 target. (F) Measured edge response (red circles), from the red box in (E), are fitted with an error function (blue line) to yield the transverse resolution.

provide the highest system detection sensitivity (94.6 dB with 3.5 mW sample power and an exposure time of 14.1 μs), and was chosen for this study (**Figure 4-2D**).

4.3.1.2. Focal shifting

A tightly focused spot favors cellular resolution in the *en face* plane. In the sample arm, an optimized scan and tube lens pair is used, which achieves an Airy disk confined spot diagram based on the ray tracing simulation. The experimentally measured transverse resolution of 0.94 μm is near the theoretically calculated value of 0.77 μm (**Figure 4-2E-F**). The corresponding confocal-gated depth-of-field of 3.2 μm (intensity FWHM in tissue), together with the coherence gate of 5.6 μm (intensity FWHM in tissue), defines

the axial resolution. To perform volumetric imaging, the sample is translated stepwise towards the objective, in 5 μm intervals (**Figure 4-1C**). Relative to confocal microscopy, we improve sectioning by employing the path length resolution achieved by the coherence gate to filter ballistic or quasi-ballistic signal from the purported focus (**Figure 4-1C**).

4.3.2. Surgical Preparation

Six adult wild type mice (four 2-4 month old C57BL/6 males, as well as 3.3 month old and 12.5 month old C57BL/6 females, from Charles River), one five-familial Alzheimer's disease (5xFAD) transgenic mouse, and its WT littermate (both 14 month old males) were imaged. Mice were anesthetized continuously with isoflurane (1-2.5% v/v), vaporized in a gas mixture of 80% medical air and 20% oxygen. Mice were immobilized in a stereotactic frame (Stoelting Co., IL, USA), while head fixed by ear pins and a bite bar. As shown in **Figure 4-1B**, the scalp was then removed carefully, and a thinned-skull cranial window centered near the posterior somatosensory cortex was created with a dental drill under saline cooling. The skull was not thinned aggressively, leaving a residual thickness of 49.3 ± 11.6 μm (mean ± std. dev.) to minimize possible mechanical trauma to the superficial cortex. Next, a coverslip was attached to the skull with superglue (Vibra-Tite, FL, USA). D_2O, with a lower absorption than H_2O, was added as the objective immersion medium.

For an imaging session that acquired at foci from the cortical surface ($Z = 0$ mm) to a cortical depth of $Z = 1.5$ mm, 301 volumes were acquired with a translation step D_Z of 5 μm. A total of 22 minutes was required for stage translation, scanning, and data saving [1024 (z) x 640 (X) x 320 (Y) voxels per volume]. This constitutes a four-dimensional (z, X, Y, Z) data set. The incident sample power was 3.5 mW. Note that to achieve similar imaging depths, state-of-the-art nonlinear techniques such as multi-photon microscopy[203,208] or third-harmonic-generation microscopy[209] require an order-of-magnitude higher power, even with more invasive preparations. All the experimental procedures and setup were approved by UC Davis Institutional Animal Care and Use Committee.

4.3.3. Dynamic Focusing and Image Fusion

OCM image reconstruction consisted of background subtraction, fringe resampling, spectral shaping, dispersion compensation, and Fourier transformation. Volumetric complex OCM data at each focusing depth Z_i, indexed by i, are denoted as $A_i(z,X,Y)$, where z,X,Y are OCM coordinates. Note that z, the OCM depth, is determined as the path length divided by 2, divided by an assumed refractive index of 1.33. The synthesized image volume $I(z,X,Y)$ is given by (**Figure 4-1C**):

$$I(z,X,Y)=\sum_{i=1}^{N}|A_i(z-S_i,X,Y)|^2 h[z-F_i(X,Y)-S_i], \tag{4.1}$$

where $S_i=(i-1)D_S$ represents the depth shift of the volumetric data, with depth shift D_S being related to the sample translation interval D_Z (they are equal if the group index of the immersion medium is assumed for OCM reconstruction). The axial weighting function, h, suppresses out-of-focus and multiply scattered light. It was chosen as the convolution ($*$) of rectangular and Gaussian functions, $h(z)=Rect[z/(10.6\ \mu m)]*exp[-z^2/(14.2\ \mu m^2)]$. The FWHM of h ($\delta=11.4\ \mu m$) was carefully optimized to both suppress unwanted light, while also reducing speckle (**Figure 4-3**). $F_i(X,Y)$ denotes the estimated focus along the depth (z) axis. The approximate physical focusing depth is denoted by Z_i or Z in plots. Sub-pixel shifting in the axial direction was performed on the complex data A_i via the Fourier shift theorem. Image reconstruction and fusion in post processing took 15.4 hours in Matlab (R2020a, MathWorks, Inc., MA, USA) on a workstation with the Xeon W-2135 Processor @3.7 GHz (Intel, Corp., CA, USA). This time can be improved by optimizing the code for parallel processing.

4.3.3.1. Focus detection

To detect the focus, first, the maximum intensity location at each (X,Y) position is taken as a coarse approximation of the focus. This first estimate is noisy due to speckle. Next, a two-dimensional surface fit [up to second order with (X,Y) as variables] generates the smoother curve. Next, the OCM focus depths at each (X,Y) coordinate are fitted by piecewise linear fitting versus physical depth Z. The slope in layer I is

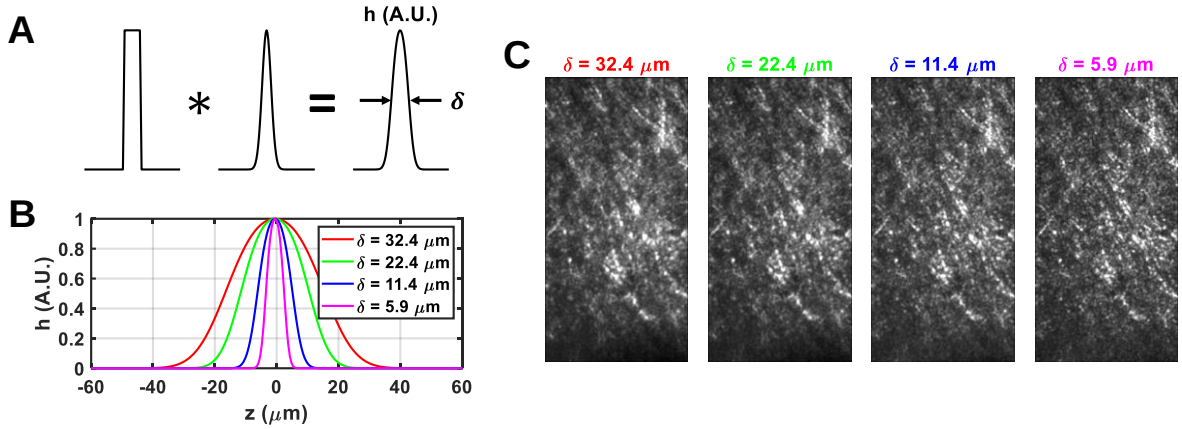

Figure 4-3. Optimization of axial weighting function (h). (A) The shape of h is given by convolution of rectangular and Gaussian functions. (B) Axial weighting functions with different full-widths-at-half-maximum (FWHMs) (δ). (C) *En face* images at the same nominal cortical depth, derived from different weighting functions, exemplify the tradeoff between speckle reduction (large δ) and out-of-focus light suppression (small δ).

presumed to be different from that of other layers. This fit or interpolation also corrects for focus detection errors caused by anatomical features (for instance, highly scattering white matter biases the OCM depth of the focus inferred from the maximum intensity alone).

4.3.3.2. Despeckle vs. out-of-focus light rejection

By combining coherence and confocal gates, optical coherence microscopy rejects multiply scattered and out-of-focus light. Image fusion in depth (z) is intended to average structures in adjacent data volumes to reduce speckle. However, a structure that is in focus in one volume is slightly out-of-focus in the next. Therefore, a weighting function, h, which balances speckle reduction against out-of-focus light suppression (**Figure 4-3A-B**), multiplied each data volume prior to image fusion. The weighting function is determined as the convolution ($*$) of rectangular and Gaussian functions:

$$h(z) = rect[z/(2z_w)] * e^{-2z^2/z_w^2}, \tag{4.2}$$

where z_w adjusts the width of h. As shown in **Figure 4-3C**, when h gets narrower, the contrast of myelinated axons against the background neuropil is enhanced due to better rejection of multiply scattered light, however, less averaging leads to an image that is more corrupted by speckle. A weighting function FHWM (δ) of 11.4 μm was chosen to balance the two effects.

4.3.4. Display

Before display, the synthesized image volume was first normalized in depth (z) to account for tissue attenuation. Then 2D averaging (3.0 μm) in X and Y, together with image fusion in z, generates the 3D averaged image volume.

4.3.4.1. Cytoarchitecture

Hypo-reflective neuronal cell bodies are distinguished from the surrounding neuropil by lower backscattering[60]. Thus, minimum intensity projections were taken across slabs within the image volume for *in vivo* visualization of cytoarchitecture in sagittal, coronal, or transverse planes.

4.3.4.2. Myeloarchitecture

Axons with a high refractive index, lipid-rich myelin sheath are distinguished from the surrounding neuropil by higher backscattering[60,210]. Thus, maximum intensity projections were taken across slabs within the image volume for *in vivo* visualization of myeloarchitecture in sagittal, coronal, or transverse planes.

4.3.4.3. Plaques

Insoluble Aβ aggregates or plaques are highly scattering compared to background neuropil in the mouse cerebral cortex[211]. To visualize highly scattering clusters corresponding to plaques, 3D imaging volumes were summed over the imaging projection direction.

4.3.5. Fitting Laminar Signal Characteristics

In addition to visualizing cytoarchitecture and myeloarchitecture, laminar variations in optical properties may relate to tissue composition. Layer-by-layer tissue attenuation coefficients, taken as the change with focal depth (i.e. slope) of the OCM signal around the estimated focus, were quantified by piecewise linear fitting. Spectroscopic analysis of attenuation was performed, and interpreted in terms of water and lipid content.

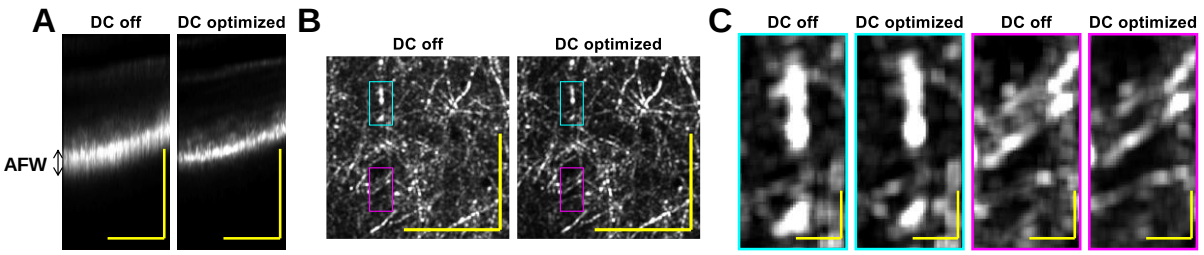

Figure 4-4. Minimally-invasive 1700 nm optical coherence microscopy (OCM) with optimized dispersion compensation. (A) The apparent focal width (AFW) in cross-section is found to be narrowed by numerical dispersion compensation (DC). A method of dispersion optimization based on this observation was devised (Fig. S1) and validated (Fig. S2). Optimized dispersion compensation results in sharper myelin features in layer I *en face* maximum intensity projections (B-C). Notably, the dispersion optimization method was found to work even when OCM volumes did not contain clear image features, enabling optimization of dispersion compensation at each focal depth (Fig. S1). Scalebars represent 0.1 mm and 10 μm in (A-B) and (C), respectively.

4.4. Results

To achieve three-dimensional and minimally invasive optical biopsy, OCM volumes were acquired through the skull, which was lightly thinned to ~50 μm to minimize potential damage to the cerebral cortex. A coverglass was affixed to the skull with superglue and heavy water (D_2O) was employed as the immersion medium for the objective (**Figure 4-1B**). The measured OCM transverse resolution was sub-micron, while the nominal coherence-gated axial resolution was 5.6 μm in tissue, and axial sectioning was further aided by the confocal gate. Dynamic focusing was achieved by translating the sample towards the objective in 5 μm intervals (**Figure 4-1C**). An OCM volume with a narrow depth-of-field, leading to a narrow range of imaging depths in **Figure 4-1C**, was acquired at each focal position, yielding a 4-dimensional data set. To synthesize these data into a single volume while suppressing out-of-focus and multiply scattered light, an axial weighting function, h, was employed.

4.4.1. Optimization of Dispersion Compensation in the 1700 nm Optical Window

Chromatic dispersion must be compensated, either physically or numerically, to maintain optimal axial resolution in OCM[212]. As the focus is translated deeper into the brain, brain tissue [mostly water (H_2O)[213]] replaces the D_2O immersion medium along the sample optical path (**Figure 4-1C**). This possibly leads to a focal depth-dependent chromatic dispersion; however, chromatic dispersion measurements of H_2O and D_2O

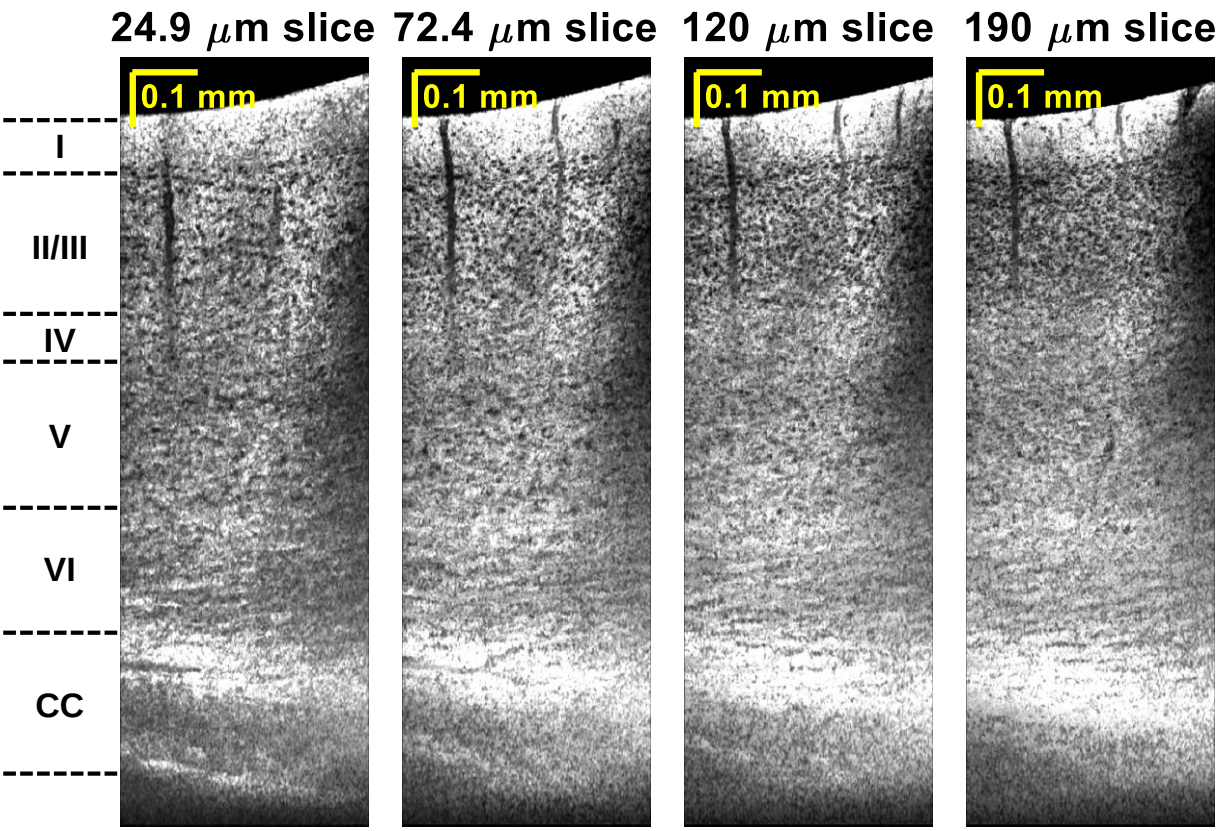

Figure 4-5. ***In vivo*** **minimally invasive optical biopsy of the mouse brain. Minimum intensity sagittal images, with different projection thicknesses in the coronal direction, show cytoarchitecture across cortical depth, without requiring tissue slicing. Cortical layers and corpus callosum (CC) are labelled.**

in the 1700 nm window are sparse in the literature[214-216], making this possibility challenging to assess. At the same time, conventional empirical image-based numerical dispersion optimization methods[217] are not always applicable for shallow depth-of-field OCM images which lack clear features to aid optimization, particularly in deep tissue.

These limitations led us to develop a simple and robust way of optimizing numerical dispersion compensation for *in vivo* OCM (see **Supplementary Note 7.1**). We first noticed that the shallow depth-of-field of the OCM system confines the path length distribution of detected light (**Figure 4-4A**). Then, to optimize numerical dispersion compensation, we sought to minimize the apparent focal width, defined as the axial width of the OCM intensity distribution, at each focal depth (**Figure 4-4A, Fig. S1B-C**). As this

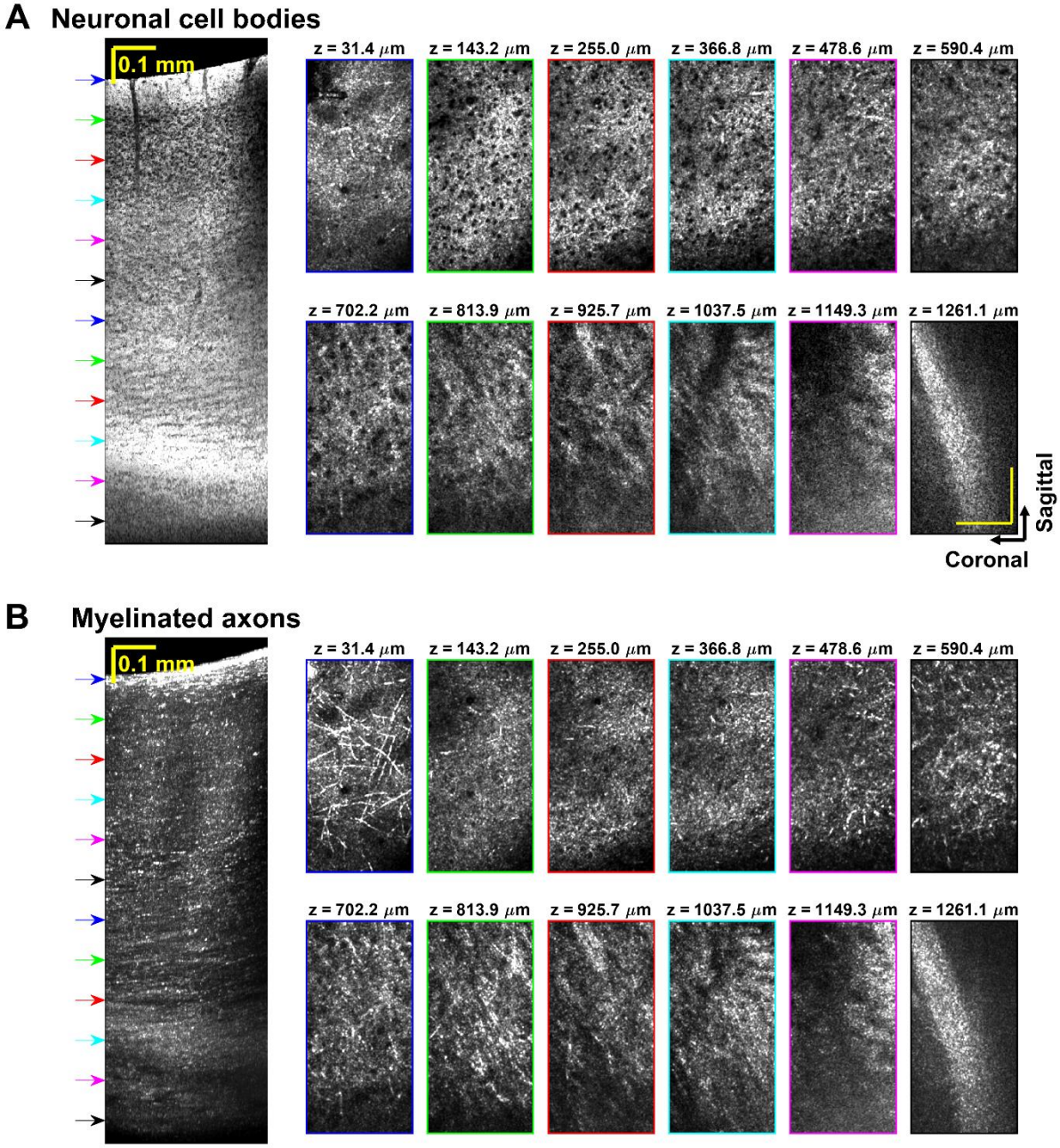

Figure 4-6. ***In vivo*** **visualization of neuronal cell bodies (A) and myelinated axons (B) in transverse planes. Outline colors of** ***en face*** **images correspond to arrow colors on the sagittal images on the left, indicating projection locations. Sagittal slice projection thickness: 190 μm. Axial projection depth: 11.2 μm. Scalebars represent 0.1 mm and apply to all the** ***en face*** **images.**

approach relies on the path length profile caused by tight light focusing, it is valid even if raw OCM images lack well-defined structures. As shown in **Fig. S1D-F**, the optimal second-order dispersion compensation coefficient increased about 507 fs^2 as the focus shifted from the brain surface to 900 μm depth, though

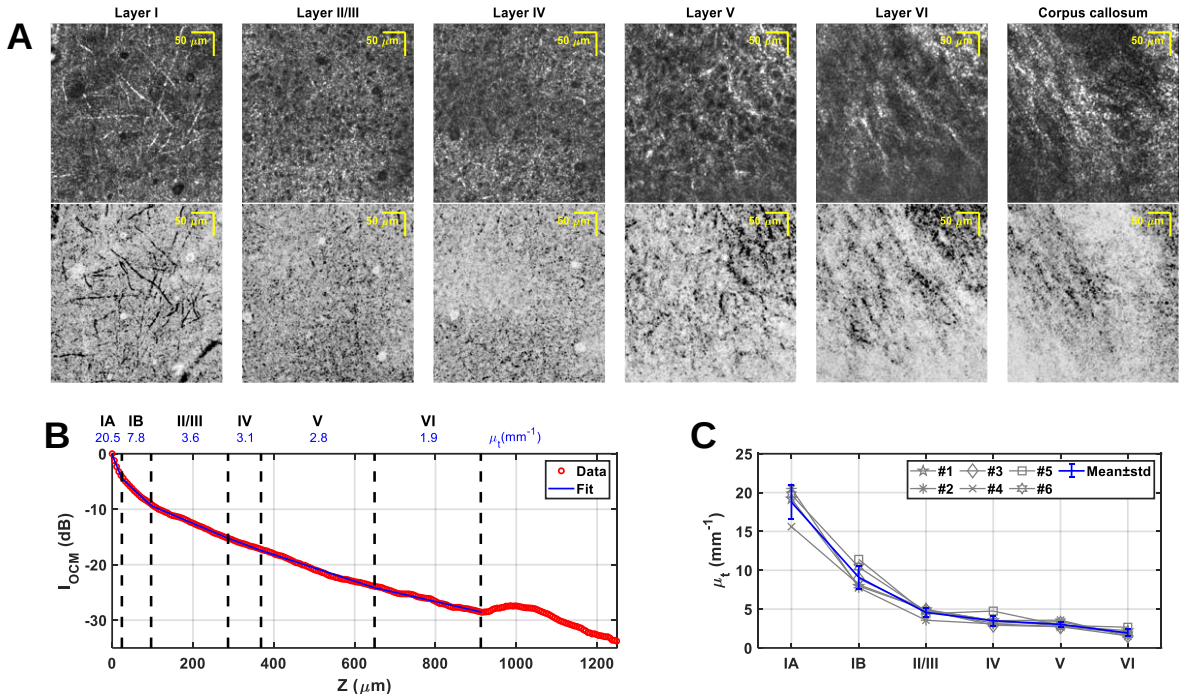

Figure 4-7. Analysis of cortical lamination. (A) *En face* images of neuronal cell bodies (top row) and myelinated axons (inverted gray scale, bottom row) from the cortex and corpus callosum exhibit laminar trends of cytoarchitecture and myeloarchitecture, respectively. (B) Layer-by-layer attenuation coefficients are quantified with piecewise linear fitting (blue line) of background corrected OCM signal (red circles) versus depth. (C) Total attenuation coefficients of six animals (gray), with mean ± std (blue).

systematic changes in the third-order coefficient were undetectable. Furthermore, even though the apparent focal width increased with deep focusing due to multiple scattering (**Figure 4-1C**, **Fig. S1D**), the method still provided consistent results.

To validate this method, in view of the previously-noted dearth of chromatic dispersion data in the 1700 nm wavelength range, we undertook our own measurements of H_2O and D_2O dispersion (**Fig. S2**). We found that dispersion changes with focal depth, derived by our empirical *in vivo* approach, agreed with independent *ex vivo* measurements of the dispersion difference between H_2O and D_2O (**Fig. S2F**). Therefore, as the sample replaces the immersion medium during focus translation, the change in dispersion along the path to the focus can be reliably quantified and corrected.

4.4.2. Volumetric Imaging

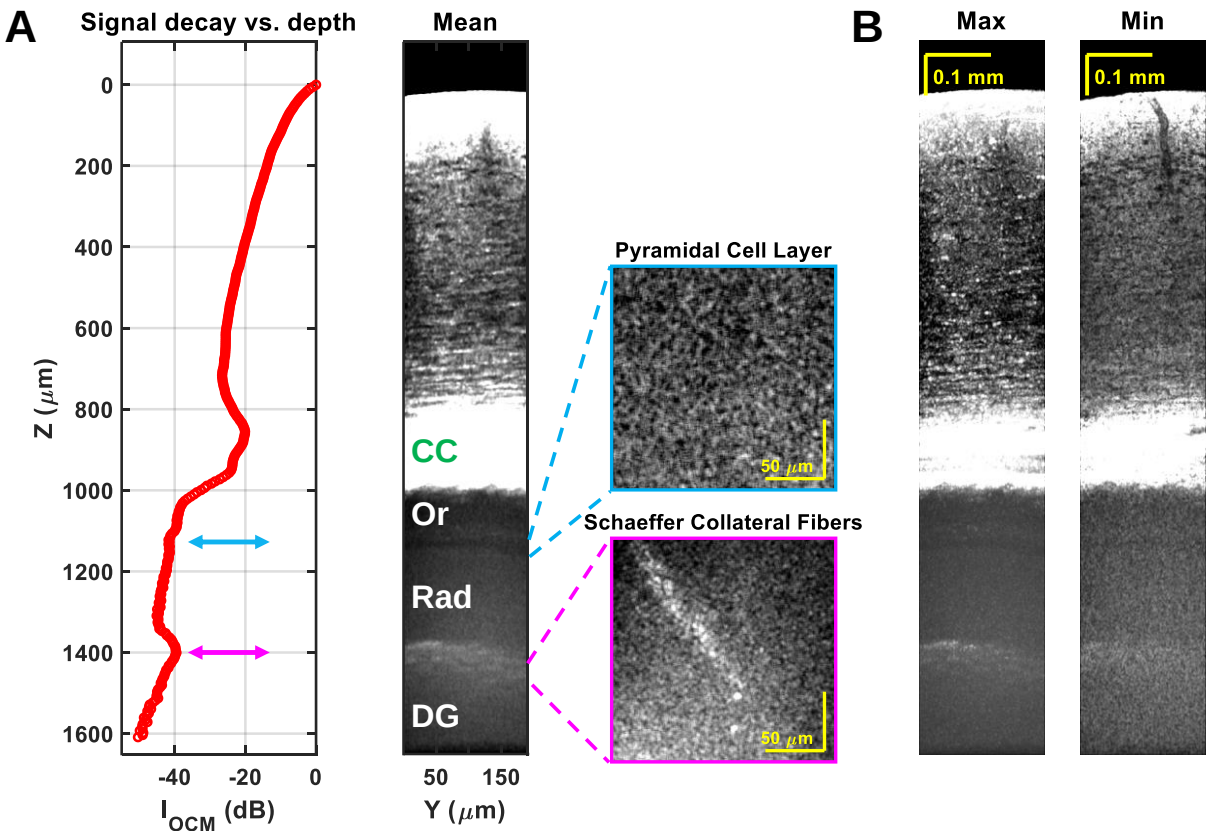

Figure 4-8. ***In vivo*** **minimally invasive sub-cortical imaging. (A) OCM signal decay vs. depth (left panel) shows layered features in the sub-cortical region, as seen in the corresponding averaged coronal image (middle panel). CC: corpus callosum; Or: stratum oriens; Rad: stratum radiatum; DG: dentate gyrus.** ***En face*** **images of the Pyramidal cell layer and Schaeffer collateral fiber layer are shown in the right panel.** ***En face*** **image projection depth: 11.2 µm. (B) Maximum and minimum intensity projection coronal images, projected across a slab thickness of 60.0 µm.**

Sagittal minimum intensity projection images highlight neuronal cell bodies (**Figure 4-5**) without cutting the brain. Laminar variations in the cell body distribution consistent with granular cortex[218] are observable. Cytoarchitecture and myeloarchitecture trends are also visualized in transverse planes (**Figure 4-6**). As might be expected, bulk tissue OCM attenuations (signal slopes) also differ across cortical layers (**Figure 4-7**), with neurite-rich layer I showing a much larger attenuation coefficient than the layers underneath with higher cell density. While OCM signal slope is related to the ballistic attenuation coefficient, OCM signal slope is generally smaller in magnitude than ballistic attenuation due to detection of multiply scattered light[29]. OCM signal slope can also be affected by depth-dependent backscattering. For instance, the increase in backscattering due to increasing myelination with cortical depth across layer IV-VI[219] likely contributes

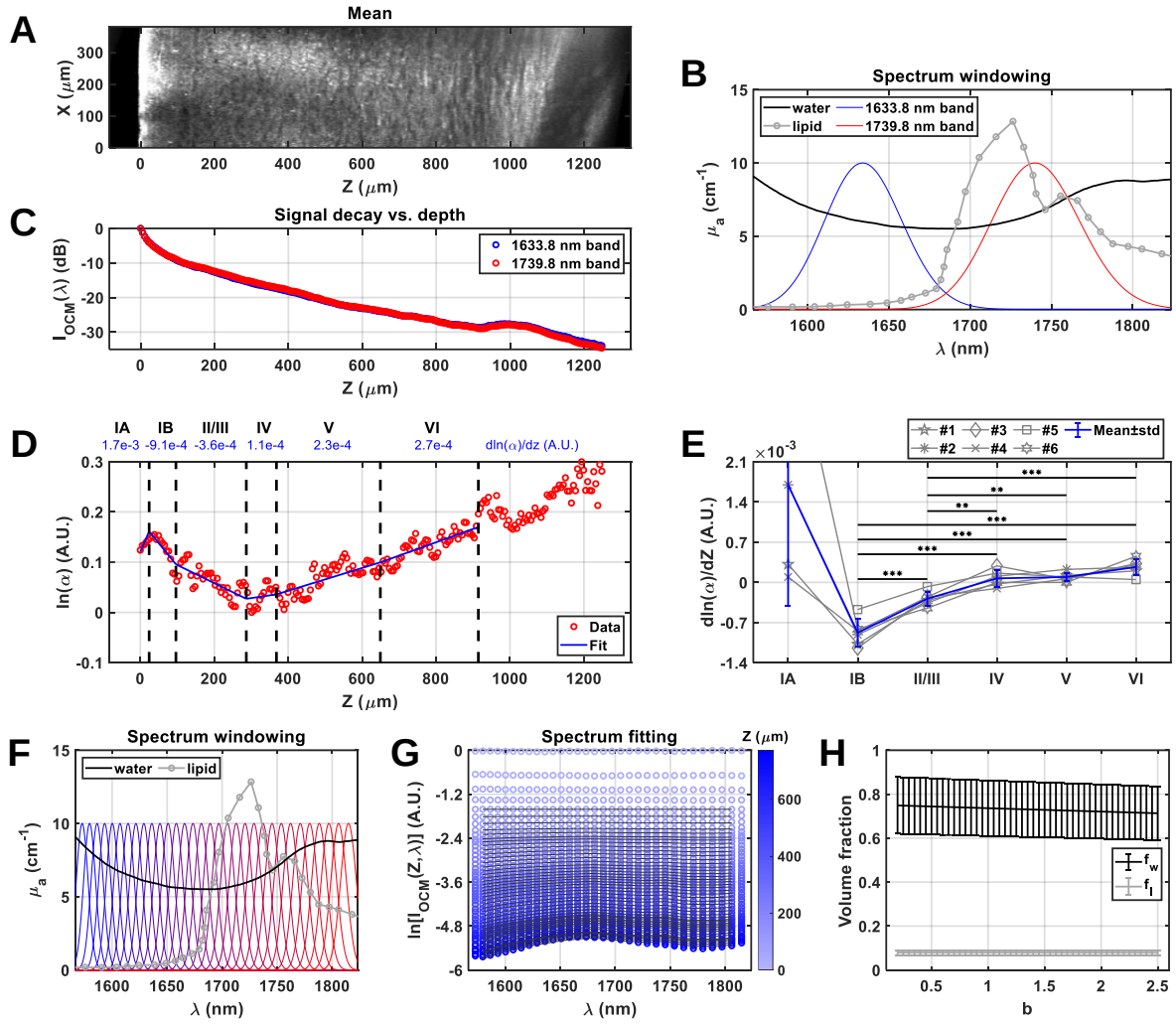

Figure 4-9. Spectroscopic tissue composition analysis. (A) Sagittal image, averaged over a 59.3 µm thick slab, showing morphological changes with depth (*Z*). Spectroscopic analysis was performed with either two wide subbands (B-E) or thirty-two narrow subbands (F-H). (B) Water absorption (black) is nearly identical between the two wide subbands, while lipid absorption (gray) is weighted towards longer wavelengths. (C) Background-corrected subband signal decay profiles exhibit slight differences. (D) The signal ratio between short and long wavelength subbands, analyzed according to layer. Natural logarithm of the signal ratio (α, red circles) versus depth is quantified using piecewise linear fitting (blue line) for each cortical layer. (E) Log signal ratio slopes of six animals (gray), with mean ± std (blue), reveals that signal ratio increases from layer IV to layer VI. (F) Subband windows for higher spectral resolution analysis. (G) Exemplary data from one animal showing OCM spectrum (logarithm scale) varies with depth (from shallower to deeper into cortex: light to dark blue, circles), and the corresponding fitting results (dark solid lines). Fitting ranges in *Z* and λ are covered by the dark solid lines. (H) Mean ± std of water (f_w) and lipid (f_l) volume fraction estimates from six animals as the assumed b value (scattering power) changes.

to a lower signal slope. A similar flattening of the three-photon excited fluorescence signal versus depth in deeper cortical layers was not observed[202,220]. These differences may arise from the physical mechanisms responsible for signal generation; fluorescence in three-photon microscopy and backscattering in OCM.

Overall, in agreement with an earlier Optical Coherence Tomography (OCT) study[76], OCM signal in the 1700 nm optical window attenuates gradually with brain depth (**Figure 4-7**), enabling imaging of sub-cortical regions (**Figure 4-8**). Image volumes depict cellular detail in three dimensions. Changes in the orientation and size of myelinated fibers from the mid-cortical to sub-cortical regions, more than 1 mm deep, are clearly visualized (**Fig. S3**).

4.4.3. Evidence for Lipid Absorption

In addition to imaging of brain architecture (**Figure 4-9A**), OCM potentially quantifies tissue composition through spectroscopic analysis of attenuation. Within the water absorption window[41], lipid absorption[31] is significantly higher beyond 1700 nm (**Figure 4-9B**). The OCM signal at focal depth Z and wavelength λ is defined as:

$$I_{OCM}(Z,\lambda) = \mu_b(Z,\lambda) I_0(\lambda) e^{-2\int_0^Z \mu_t(u,\lambda)du}, \tag{4.3}$$

where μ_b represents the backscattering coefficient and I_0 is the reference OCM spectrum. The total tissue attenuation coefficient is defined as: $\mu_t(Z,\lambda) = \mu_{t,s}(Z,\lambda) + f_w(Z)\mu_{a,w}(\lambda) + f_l(Z)\mu_{a,l}(\lambda)$, where $\mu_{t,s}$ is the tissue scattering attenuation, $\mu_{a,w}(\lambda)$ and $\mu_{a,l}(\lambda)$ are water and lipid absorption coefficients, respectively. f_w and f_l represent water and lipid volume fractions. Due to the uncertainty principle inherent in the short time Fourier transform[49], we performed two complementary analyses that trade depth resolution for spectral resolution. First, in a high depth resolution analysis, we investigated local lipid content changes with depth, employing the signal ratio (α) of the $\lambda_1 = 1633.8$ nm subband to the $\lambda_2 = 1739.8$ nm subband [subband window full-width-at-half-maximum (FWHM) in wavenumber: 1.3×10^5 rad/m, **Figure 4-9C**]:

$$\alpha = I_{OCM}(Z,\lambda_1) / I_{OCM}(Z,\lambda_2). \tag{4.4}$$

With the assumption that the backscattering ratio of the two subbands is invariant with depth, the derivative of the signal ratio can be approximated by (see **Supplementary Note 7.4**):

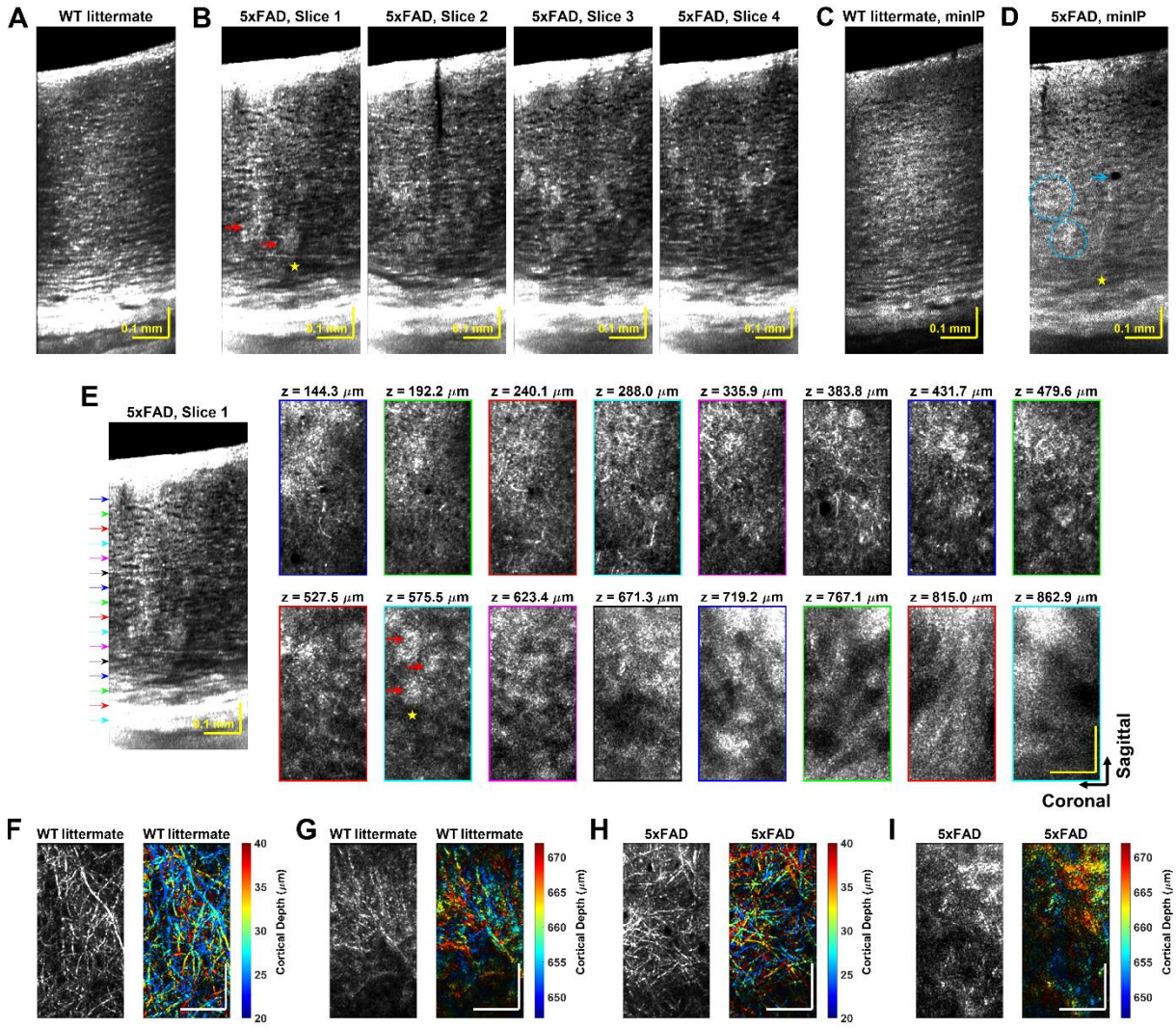

Figure 4-10. OCM of Alzheimer's disease mouse model. Compared to the WT littermate (A), the 5xFAD transgenic mouse (B) has distinct highly scattering clusters (red arrows) and wide hyporeflective regions (yellow asterisk). Corresponding histology (Fig. S6) suggests that the highly scattering clusters are plaques. Minimum intensity projection (minIP) image in the WT littermate (C) depicts clear cytoarchitecture, which is lacking in the AD mouse in deeper cortical layers (D, cyan circles). Hyporeflective voids, potentially related to tissue loss, are also noted (cyan arrow). (E) AD-associated plaques (red arrows) and regions of possible demyelination (yellow asterisk) are visualized in the *en face* plane. Outline colors of *en face* images correspond to arrow colors on the sagittal image on the left, indicating projection locations. Sagittal slice summation thickness: 17.8 µm. Depth color-coded *en face* images of myelinated axons and corresponding grayscale images illustrate intact myeloarchitecture in the WT littermate (F-G), while suggesting demyelination in deeper layers of the AD mouse (H-I). Taken together, OCM depicts a higher incidence of abnormal findings in layers IV-VI, consistent with the higher disease burden (Fig. S6). Axial projection depth of 16.0 µm and scalebar size of 0.1 mm apply to all the *en face* images in (E-I).

$$\frac{d\ln(\alpha)}{dZ} = 2[\mu_t(Z,\lambda_2) - \mu_t(Z,\lambda_1)]. \tag{4.5}$$

Note that if scattering were the main source of attenuation, short wavelengths would be attenuated more, and α would decrease with depth. Higher absorption, and hence, attenuation, in the longer wavelength (λ_2) subband would increase α with depth. As seen in **Figure 4-9D-E**, α clearly increases with depth in the deeper cortical layers. This suggests higher lipid absorption in the λ_2 subband.

Gaining confidence from this preliminary evidence of a lipid absorption signal, a second, high spectral resolution analysis was conducted. To estimate bulk volume fractions of cortical water and lipid, the OCM spectrum was analyzed with 32 subbands (subband window FWHM in wavenumber: 3.2×10^4 rad/m, **Figure 4-9F**) and fitted by the following model (**Figure 4-9G**):

$$\ln[\frac{I_{OCM}(Z,\lambda)}{I_0(\lambda)}] = \mu_b(Z) - 2[\mu_{t,s}(\lambda) + f_w\mu_{a,w}(\lambda) + f_l\mu_{a,l}(\lambda)]Z, \quad (4.6)$$

with the assumption that μ_b varies with Z. Scattering attenuation is assumed to be described as $\mu_{t,s}(\lambda) = A(\lambda/500)^{-b}$, where b is the scattering power[33]. As b changes from 0.1 to 2.5, the mean recovered water volume fraction of six animals varies from 0.75 to 0.71, and the mean lipid volume fraction has a relatively consistent value of 0.08 (**Figure 4-9H**), which are in agreement with the reported *ex vivo* measurements[213,221,222].

4.4.4. Neuropathology

To further demonstrate the utility of our approach for neuropathological studies in older mice, we proceeded to image a transgenic (5xFAD) model of Alzheimer's disease. In this model, amyloid pathology in the cortex develops earliest in deeper layers[223,224]. Imaging the resulting variations with cortical depth presents a challenging test for any *in vivo* microscopic technique. Notably, the OCM approach does not require the common but artificial approaches of transgenic expression of a fluorescent protein or injection of a contrast agent[225], greatly facilitating such studies. OCM images from a 14-month old 5xFAD transgenic mouse and its wild type (WT) littermate are compared in **Figure 4-10**, **Fig. S4 and Fig. S5**. Highly scattering clusters (indicated by red arrows) were observed in the AD volumes but not in WT volumes (**Figure 4-10A-B**, and

Fig. S4), and corresponded with FSB-labelled amyloid plaques in histology (**Fig. S6A**). Large hyposcattering regions in deeper cortical layers (example indicated by the yellow asterisk) were observed in AD volumes (**Figure 4-10B** and **Fig. S6A**). As NeuN was present in these regions (**Fig. S6A**), we must invoke an explanation other than neuronal loss. One possible explanation for these hyposcattering regions is demyelination, which has been reported before[226,227]. Hyposcattering voids (one example indicated by the cyan arrow) are also seen in the AD minimum intensity projection (minIP) image (**Figure 4-10D**). These voids, with lower reflectivity than surrounding neuropil, are spheroids with well-demarcated boundaries and present at shallower cortical depths in OCM. In minIP images, laminar cytoarchitectural trends are intact in the WT littermate (**Figure 4-10C**), yet are disrupted in deeper layers of the AD mouse by plaques (**Figure 4-10D**, cyan circles). Features of plaques, tissue loss, and degeneration, displayed in transverse planes of an AD mouse (**Figure 4-10E**), are absent in the WT (**Figure 4-10F-G**, **Fig. S4 and Fig. S5**). Notably, single myelin fibers are visualized in layer I of the 5xFAD mouse (**Figure 4-10H**), as in the WT (**Figure 4-10F**). However, relative to the WT (**Figure 4-10G**), myelin contrast is lost in deeper cortical layers of the 5xFAD mouse where large plaques appear (**Figure 4-10I**), consistent with above hypothesis of demyelination. The increasing disease burden with cortical depth[223], as quantified by histological plaque count (**Fig. S6B**), seems to be manifested in the increased incidence of abnormal OCM findings in layers IV-VI. Notably, minimal differences between the WT and 5xFAD mouse were observed in the superficial cortex, highlighting the importance of deep imaging in this model.

4.5. Discussion

Neuroimaging techniques must strike a compromise between minimal invasiveness, resolution, imaging depth, and the use of exogenous contrast. The 1700 nm OCM approach introduced here achieves a unique balance between these competing goals. Here we explore two key aspects of the approach: the coherence gate and the long wavelength excitation.

4.5.1. Benefits Over Confocal Microscopy: the Coherence Gate

One advantage of OCM is the synergy between confocal and coherence gating to improve imaging depth. Confocal gating, achieved here by illumination and detection through a single mode optical fiber that acts as a pinhole[228], provides depth sectioning in highly scattering tissue[229]. However, with deeper focusing, confocal performance degrades markedly due to multiple scattering. In this study, by filtering light according to path length[28], the coherence gate enabled us to partially reject multiply scattered light.

Can we observe degradation of the confocal gate and quantitatively assess the benefits of the coherence gate? Referring to **Fig. S7A-B**, the theoretical FWHM of the system confocal gate (red curve) is narrower than that of the coherence gate (blue curve). However, as the focusing depth increases, the range of light path lengths that pass the confocal gate broadens due to multiple scattering (**Fig. S7C-D**). To answer the above question, we employ our multidimensional data set to digitally broaden the coherence gate, and thereby assess its benefits. As the effective, digitally broadened, coherence gate width (δz_{eff}) increases (**Fig. S7C-D**), we find that the signal decays more slowly with focal depth (Z). It has previously been suggested that the signal decay with depth (μ_t) should approach the ballistic attenuation coefficient ($\mu_s + \mu_a$) as rejection of multiply scattered light improves[29], where a steeper signal slope indicates better rejection of multiply scattered light. Therefore, since a narrower coherence gate (i.e., finer OCM axial resolution) steepens the signal slope (**Fig. S7C**), we infer that it aids selective removal of multiply scattered light. Thus, the use of the entire 1700 nm window bandwidth with an extended InGaAs detector, as opposed to only a portion of this window with standard InGaAs, aids deeper imaging.

4.5.2. Longer Wavelengths Enable Deeper OCM Imaging

It is instructive to compare the performance of the 1700 nm window with the more popular 1300 nm window for deep OCT imaging. Previously 1300 nm OCM was shown to provide images of the deep cortical layers, but not subcortical regions, in rats, through invasive cranial windows[60]. The OCM signal slope at 1700 nm was estimated to be 35.3% lower than that at 1300 nm[76]. Approximating signal slope as a summation of terms corresponding to tissue scattering and absorption, and since water and lipid absorption are known to be higher at 1700 nm than at 1300 nm, we infer that attenuation due to scattering must be lower at 1700

nm. This points to a reduction in the scattering coefficient, though possible differences in scattering anisotropy cannot be ruled out[29,33]. Nonetheless, the minimally invasive, high quality and deep brain imaging achieved here by 1700 nm OCM provide empirical data to support the benefits of longer wavelength OCM.

In optical coherence tomography (OCT) and OCM, moving to longer wavelength has been considered as a dual-edged sword, since, though attenuation is reduced, backscattering may be reduced too. The observed performance of longer wavelengths for deep imaging in this work comports with results of brain tissue clearing studies[219,230], where the benefits of a reduction in multiply scattered light far outweigh the reduction in backscattering cross-section, aiding deeper imaging. Nevertheless, the ability to resolve features *in vivo* does degrade slightly across the cortical depth (**Fig. S8**). While the technical challenges of the 1700 nm wavelength range are significant, improvements in light sources and detector technology are on the horizon. The demonstrated capabilities of 1700 nm OCM for imaging deep in the brain suggest promise for deep imaging in other highly scattering, water-rich tissues as well.

4.6. Acknowledgements

This work was supported by National Institutes of Health grants NS094681, NS105043, EB029747, EB023591, and EY031469. The authors would like to thank Dr. Fumitsugu Fukuyo, Tomohiko Yabe, and Ryota Kakei from Hamamatsu Photonics K.K., and Masakazu Kawazu from Hamamatsu Corporation for their valuable discussions and help with the light source.

Chapter 5 Non-invasive, *in vivo* rodent brain Optical Coherence Tomography at 2.1 microns

5.1. Abstract

In biological tissue, longer near-infrared wavelengths generally experience less scattering and more water absorption. Here we demonstrate an optical coherence tomography (OCT) system centered at 2.1 microns, whose bandwidth falls in the 2.2 micron water absorption optical window, for *in vivo* imaging of the rodent brain. We show *in vivo* that at 2.1 microns, OCT signal is actually attenuated less in cranial bone than at 1.3 microns, and is also less susceptible to multiple scattering tails. We also show that the 2.2 micron window enables direct spectroscopic OCT assessment of tissue water content. We conclude that with further optimization, 2.2 micron OCT will have advantages in low water content tissue such as bone, as well as applications where extensive averaging is possible to compensate absorption losses.

5.2. Introduction

Looking deeper into biological tissue with high resolution is a fundamental goal of biophotonics. Yet, tissue scattering and absorption[33] limit the achievable imaging depth. While the scattering coefficient (μ_s) decreases at longer wavelengths, the absorption coefficient (μ_a) generally increases[40]. Water absorption locally drops within near-infrared (NIR) optical windows located around 1.05, 1.3, 1.7, and 2.2 μm[41]. The ballistic attenuation coefficient (μ_s+μ_a) is also locally minimized within each of these windows. In Optical Coherence Tomography (OCT), longer wavelengths are of particular interest, even though water absorption is higher, since less scattering implies that a higher fraction of the detected OCT signal comprises single backscattering paths, as opposed to multiply scattered paths. The window at 1.3 μm is often used in OCT due to the availability of high-performance telecommunication components. Though used less often, the 1.7 μm optical window has even lower scattering, and attains the lowest attenuation coefficient for deep microscopy in tissues such as the brain[40,76,77,202]. The NIR optical window around 2.2 μm is even more rarely used for tissue imaging because of light source limitations[45] and high water absorption[30]. However, the

benefits of 2.2 μm for *in vivo* imaging through bone, a biological tissue with moderate water mass content (12%[231]) compared to other tissues (>70%[42]), have not been investigated, to our knowledge.

Here, we describe 2.1 μm spectral domain optical coherence tomography (OCT) for non-invasive *in vivo* rodent brain imaging. Importantly, we show that attenuation in the skull is actually lower at 2.1 μm than at 1.3 μm, a conventional NIR window. We further demonstrate cortical OCT angiography in rats through the intact skull at 2.1 μm. In addition to the anticipated reduction in multiply scattered light, our results highlight additional advantages of the 2.2 μm spectral window for *in vivo* OCT: lower attenuation in bone and direct spectroscopic assessment of water content.

5.3. Methods and Materials

The 2.1 μm OCT system configuration is shown in **Figure 5-1A**. A supercontinuum light source (SuperK Extreme EXR20, NKT Photonics) was filtered by two band pass filters (BBP-1615-2280, Spectrogon; FB2250-500, Thorlabs, Inc.), and coupled by a reflective collimator (RC02, Thorlabs, Inc.) into a customized 50/50 SM2000 fiber coupler (Thorlabs, Inc.). In the sample arm, the beam was collimated by a reflective collimator (RC04, Thorlabs, Inc.), scanned by a 2D galvanometer (GVS002, Thorlabs, Inc.) and then focused onto the sample by a scan lens (LSM02 or LSM03, Thorlabs, Inc.). In the reference arm, an adjustable iris varied the reference power and a glass slab compensated the sample arm dispersion. The backscattered light from the sample and light reflected from the reference mirror were recombined by the fiber coupler and relayed to a custom spectrometer. In the spectrometer, the beam was collimated by a 90° off-axis parabolic mirror (MPD249-P01, Thorlabs, Inc.), dispersed by a diffraction grating (600 lines per millimeter, Wasatch Photonics), focused by a 150 mm effective focal length achromatic doublet pair (Thorlabs, Inc.), and detected by an extended InGaAs line scan camera (SU1024LDH-2.2RT, Sensors Unlimited). The camera was externally triggered and synchronized with 2D galvanometer scanning. Data was collected via the frame grabber (PCIe-1427, National Instruments Corp.). All the hardware control were performed by a custom LabVIEW program. The spectrometer spectral range was 1990-2210 nm (**Figure 5-1B**). The sensitivity roll-off was less than 5 dB over the first half of the imaging range (**Figure**

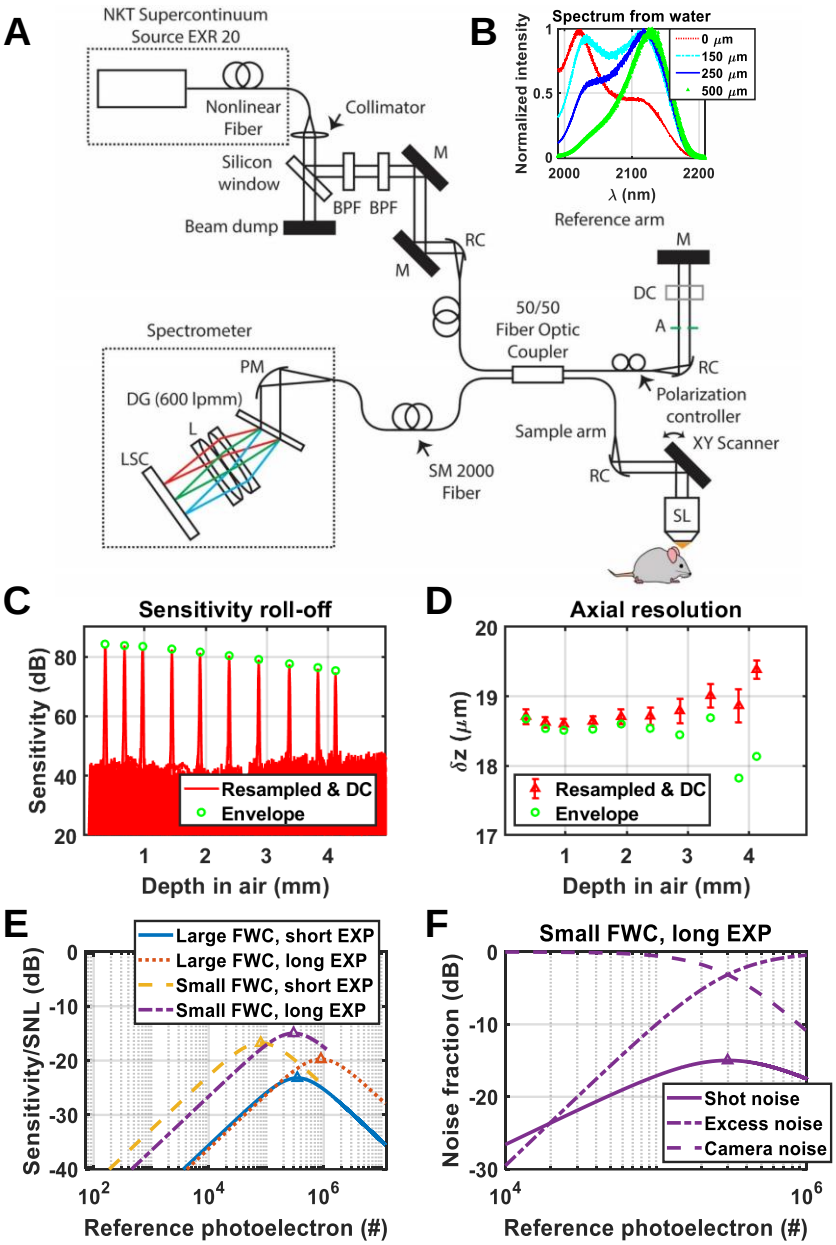

Figure 5-1. (A) Schematic of the 2.1 µm OCT system (BPF: band pass filter; M: mirror; RC: reflective collimator; SL: scan lens; A: aperture; DC: dispersion compensation glass; PM: parabolic mirror; DG: diffraction grating; L: lens; LSC: line scan camera). (B) Spectra from different depths in water with the reference spectrum at 0 µm. Sensitivity roll-off (C) and axial resolution (D) versus depth with dispersion compensation (DC), compared to values obtained from the fringe envelope (circles). (E) System sensitivity, relative to the shot noise limit, using different operation modes of the camera (SNL: shot noise limit; FWC: full well capacity; EXP: camera exposure time). (F) Fractional contributions of different noise sources using the small FWC, long EXP mode.

5-1C). The measured axial resolution in air was 18.6 µm (14.0 µm in water) (**Figure 5-1D**). A $1/e^2$ transverse resolution of 16/32 µm (LSM02/LSM03) on the sample was achieved. The maximum sensitivity was ~84 dB with 4.3 mW incident power and a 14.1 µs (47 kHz line rate) camera exposure time.

System noise sources were characterized by varying the reference power/photoelectron number captured by the camera[20]. For each pixel in the line scan camera, total noise versus detected photoelectron number was fitted with a quadratic function, and the second-order nonlinear term, first-order linear term, and the constant term were assigned to excess noise, shot noise, and detector noise, respectively. System sensitivity relative to the shot noise limit (SNL) was analyzed when the camera was operated with small (1.25 Me^-) / large (12.5 Me^-) full well capacity (FWC) and short (14.1 µs, 47 kHz line rate) / long (79.9 µs, 12 kHz line rate) exposure (EXP) time modes (**Figure 5-1E**). The maximum system sensitivity relative to SNL was around 3.2%, limited by high detector noise and light source excess noise (**Figure 5-1F**).

Despite the limited system performance, we proceeded to investigate the potential benefits of the 2.2 µm window by comparing rodent brain imaging with our 2.1 µm system and a previously-described 1.3 µm system[64], through the intact skull.

Long-Evans (rat #1-2) and Sprague-Dawley (rat #3-5) rats (male, 200-300 g, Charles River) were anesthetized with isoflurane (1.5-2.5% v/v) in a gas mixture of 80% medical air and 20% oxygen, delivered continuously during the experiments. After anesthesia induction, rats were fixed in a stereotactic frame (Stoelting Co.). The scalp was removed carefully with the skull intact. A coverslip was affixed to the skull with superglue (Vibra-Tite®), and the imaged field-of-view was 2 × 2 mm^2 / 2.5 × 2.5 mm^2. All experimental procedures and setup were approved by UC Davis Institutional Animal Care and Use Committee. The incident sample power was 3.5 / 4.3 mW with scan lens LSM02 / LSM03. Volumes, denoted as X × Y, were acquired with X axial scans × Y frames, with frame repeats for averaging and angiography. The acquired fringes were resampled, dispensation compensated, and Fourier Transformed to yield the complex OCT data. To provide an intrinsic comparison of the two optical windows, irrespective of OCT system performance, intensity (modulus squared of complex data) images were corrected for the depth-dependent noise background and sensitivity roll-off. Volumetric data within each sub location were flattened based on the segmented skull surface and then averaged transversally to yield line profiles.

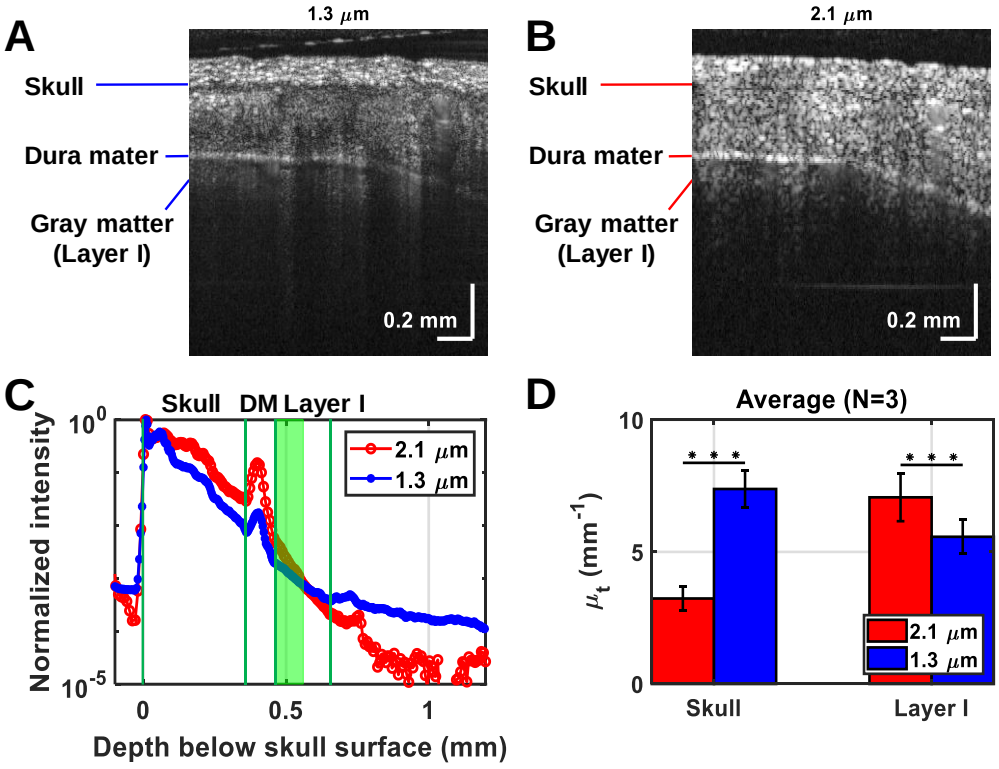

Figure 5-2. Cross-sectional images of the rat cranium and cortex with 1.3 μm (A) and 2.1 μm (B) systems. (C) Tissue OCT signal line profiles, with boundaries of skull, dura, and cortical layer I delimited by green lines (DM: dura mater). The green shaded area represents fitted range of cortical layer I. (D) Average tissue attenuation coefficients (mean ± standard deviation) of rat #1-3. Horizontal lines indicate statistically significant differences determined by two-way ANOVA. P <0.001 (***).

Refractive indices of n_{skull} = 1.5 and n_{cortex} = 1.33 were assumed for quantitative attenuation coefficient analysis.

Cross-sectional images of the same rat cranium and cortex, acquired by sequential 1.3 μm [512 × 512 (19 repeats)] and 2.1 μm [640 × 640 (19 repeats)] OCT (**Figure 5-2A-B**, respectively, n = 1.33 used for image display), illustrate different attenuation characteristics in skull versus brain (**Figure 5-2C**). The field-of-view was then divided into 9 sub-regions for total attenuation coefficient measurements and confocal gating[232] was accounted for as follows:

$$I(z,\lambda) = C\left\{\left[\frac{z - z_{cf}(\lambda)}{z_0(\lambda)}\right]^2 + 1\right\}^{-1} e^{-2\mu_t(\lambda)z}, \tag{5.1}$$

where z is depth, $I(z,\lambda)$ represents OCT line profile, $z_0(\lambda)$ is the Gaussian beam Rayleigh range, $z_{cf}(\lambda)$ denotes the depth location of the beam waist, set to the approximate focus location. The OCT signal attenuation was described by an exponential decay term, where the factor of 2 accounts for double pass attenuation, and C is a constant.

We further noticed that water absorption decreases significantly across our spectral range (1990-2210 nm). This feature might enable the spectroscopic assessment of water volume fraction (proportional to water content), provided that scattering is treated properly. Thus, we divided the spectrum into 7 sub-bands, with central wavelengths of 2009, 2037, 2065, 2094, 2123, 2154 and 2186 nm and full-width-half-maximum of ~36 nm. In each sub-region of the imaged field-of-view, the background and sensitivity roll-off corrected, locally flattened, and transversally averaged OCT signal, $I(z,\lambda)$, was then fitted with a combined model of confocal gating and single scattering:

$$I(z,\lambda) = C\left\{\left[\frac{z - z_{cf}(\lambda)}{z_0(\lambda)}\right]^2 + 1\right\}^{-1} e^{-2\left[A\left(\frac{\lambda}{500}\right)^{-b} + f_w\mu_{a,w}(\lambda)\right]z}. \tag{5.2}$$

Here, the chromatic focal shift between sub-bands was included in $z_{cf}(\lambda)$. The attenuation coefficient $\mu_t(\lambda)$ is the sum of scattering attenuation [$\mu_{t,s}(\lambda) = A(\lambda/500)^{-b}$, which, unlike μ_s, includes multiple scattering effects][33] and water absorption [$f_w\mu_{a,w}(\lambda)$], where b is the scattering power and f_w is water volume fraction. As b is sample-dependent and unknown a priori, it was sequentially fixed at values from 0 to 1.5, while C, f_w, and A were fitted using nonlinear least squares regression for each assumed b.

5.4. Results

Attenuation coefficients in superficial cortical layer I (green shaded area in **Figure 5-2C**) across 27 sub-regions among the 3 rats were compared (**Figure 5-2D**). Statistical significance was determined by two-way ANOVA, treating wavelength and subject as effects. In the skull, the OCT signal attenuates less rapidly at 2.1 μm than at 1.3 μm ($P<0.001$) due to lower scattering, while in cortical layer I, which has high water content, absorption is more severe, and the attenuation coefficient at 2.1 μm is larger ($P<0.001$).

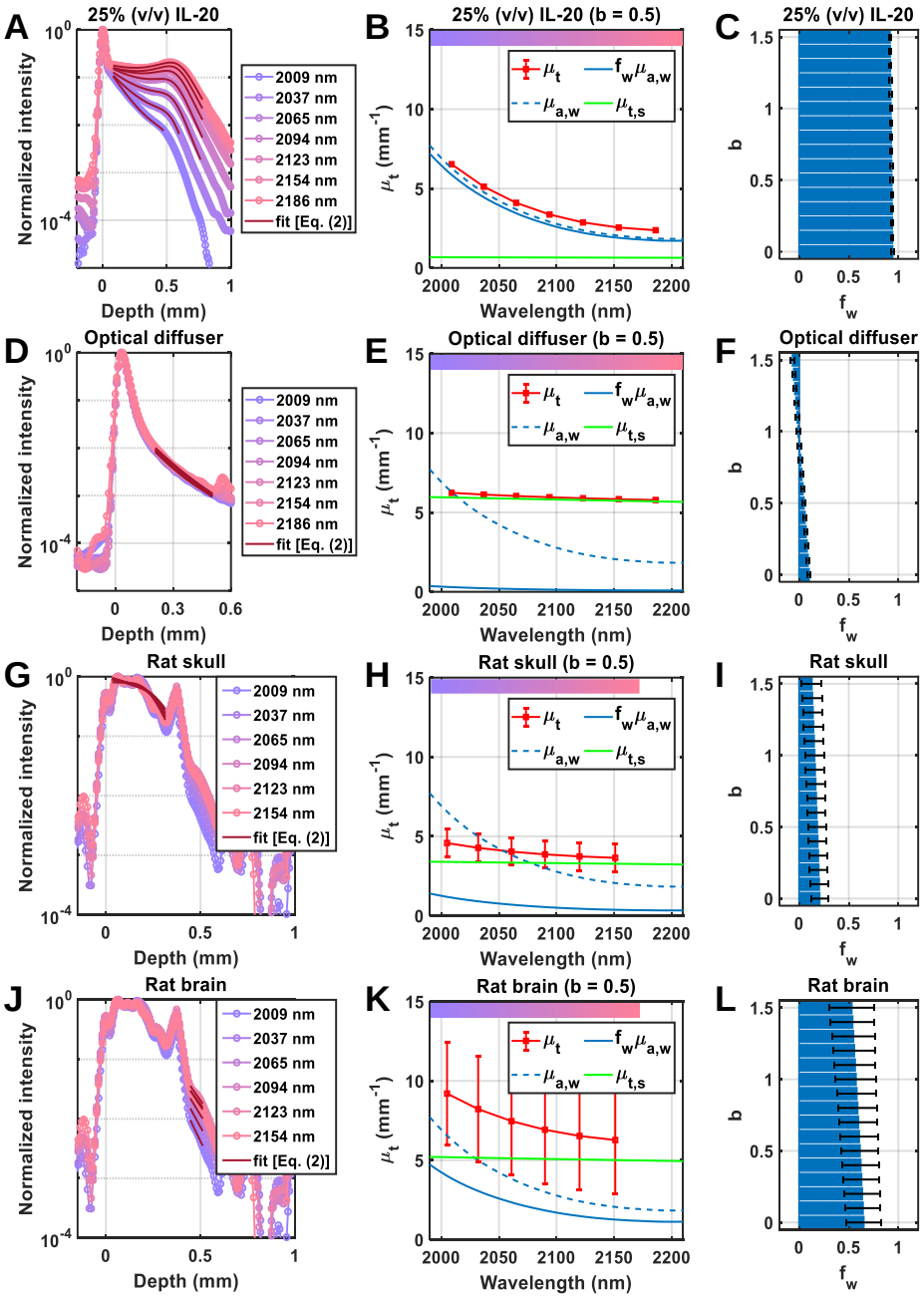

Figure 5-3. Spectroscopic measurements of water volume fraction based on absorption. (A, D, G, J) Normalized OCT sub-band line profiles for 25% (v/v) IL-20 solution, dry optical diffuser, skull, and brain (rat #2). Line profile fits (dark solid lines) are based on Equation (5.2). (B, E, H, K) Wavelength-dependent fitted attenuation coefficients (μ_t) (red) are determined as the sum of fitted absorption attenuation ($f_w\mu_{a,w}$) (blue) and fitted scattering attenuation ($\mu_{t,s}$) (green), assuming a scattering power, *b*, of 0.5. Pure water absorption ($\mu_{a,w}$) is shown for reference (blue dashed line). (C, F, I, L) Estimated water volume fraction (f_w) depends weakly on assumed *b*. Error bars indicate standard deviations.

Based on the model in **Equation (5.2)**, water volume fraction (f_w) was estimated (**Figure 5-3**). To first assess the methodology, *ex vivo* phantom experiments were performed. **Figure 5-3A** shows fitting of the

normalized OCT signal in each sub-band of a 25% (v/v) Intralipid-20 (IL-20) solution (diluted by deionized water). Assuming a scattering power of 0.5, fitted total attenuation coefficients (red in **Figure 5-3B**) follow water absorption (blue dashed line) across the spectrum, suggesting high water content. Attenuation is dominated by absorption $[f_w \mu_{a,w}(\lambda)]$ (blue), not scattering $[\mu_{t,s}(\lambda) = A(\lambda/500)^{-b}]$ (green). As the assumed b value varies from 0 to 1.5, the estimated f_w of the IL-20 solution varies from 94.1 to 91.5% (**Figure 5-3C**), which is close to the estimated value of 94.3% $[0.25 \times (1 - 22.7\%) + 0.75]$, assuming a 22.7% volume fraction of scattering particles in pure IL-20[233]. **Figure 5-3D** shows fitting of the normalized OCT signal in each sub-band of a dry optical diffuser (WS-1, Ocean Optics). Assuming a scattering power of 0.5, fitted attenuation coefficients (**Figure 5-3E**) change little across the spectrum, suggesting low water content. As the assumed b value varies from 0 to 1.5, the estimated f_w varies from 9.8 to -6.5% (**Figure 5-3F**). Non-physical negative f_w values are returned by the fitting routine to compensate large attenuation variations with larger assumed *b*.

Given these reasonable results in phantoms, we then segmented and analyzed the rat skull and brain cortical layer I *in vivo*, applying the model in **Equation (5.2)** and assuming that water is the main absorber in skull[234] and cortex in our wavelength range. For *in vivo* analysis, the longest wavelength sub-band was discarded due to poor cortical sensitivity, limited by detector quantum efficiency. Fitting of the normalized, *in vivo* OCT signal in the rat skull (**Figure 5-3G**) and superficial cortical layer I (**Figure 5-3J**) reveals that, assuming a scattering power of 0.5, fitted total attenuation coefficients across the spectrum change less in the skull (**Figure 5-3H**) than in layer I (**Figure 5-3K**), suggesting lower water content in skull. Accordingly, *in vivo* fitting (**Figure 5-3I** and **L**) estimates that cortical layer I has a higher water volume fraction (60-70%) compared to the skull (~20%).

En face angiograms (based on interframe complex OCT signal subtraction followed by intensity averaging) of the rat cranium and cortex acquired by the 1.3 [640 × 640 (9 repeats)] and 2.1 μm [640 × 640 (18 repeats)] systems (**Figure 5-4A-B**, respectively, n = 1.33 used for image display) were similar. As transverse resolutions (15 and 16 μm, respectively) were closely matched, the comparable image quality, in spite of

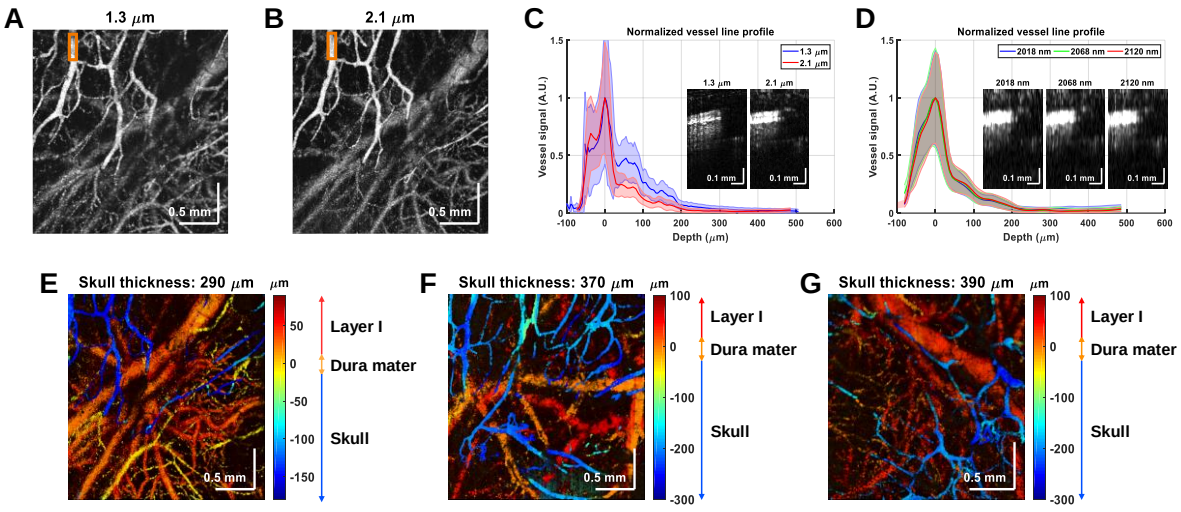

Figure 5-4. *En face* angiograms of rat cranium and cortex acquired by 1.3 µm (A) and 2.1 µm (B) OCT systems. (C) Skull vessel line profiles in an ROI (orange box) reveal diminished tails at 2.1 µm, as confirmed by cross-sectional angiograms within the ROI at the two wavelengths (insets). (D) Sub-band skull vessel line profiles within the ROI are similar from 2.02-2.12 µm, as seen in cross-sectional angiograms within the ROI (insets). (E-G) Depth (distance to the dura mater) color-coded *en face* angiograms of rats with different skull thicknesses (rat #2 and #4-5). Note that the assumed refractive index in (C)-(D) is n = 1.33, while in (E)-(G), n_{skull} = 1.5 and n_{cortex} = 1.33.

the sub-optimal 2.1 µm OCT system performance, is notable. To assess multiple scattering, after locally flattening and averaging the angiograms, normalized skull vessel line profiles from the orange ROI at 1.3 and 2.1 µm are compared in **Figure 5-4C** (example cross-sectional angiogram insets). In the line profiles, the vessel lumen is from -60-30 µm while the multiple scattering tails[54] start around 30 µm. Overall, across six similar ROIs, the magnitude of tails at 2.1 µm is 41±9% lower than at 1.3 µm. Moreover, the skull vessel line profiles of sub-band angiograms from 2.02-2.12 µm are similar (**Figure 5-4D**), indicating that water absorption is not the main factor in this finding. Rather, lower scattering around 2.1 µm likely explains the lower tail magnitude. Depth color-coded *en face* angiograms of rat #2 and #4-5 at 2.1 µm (**Figure 5-4E-G**) show skull vessels above the dura mater in blue, and cortical vessels in red (distance to dura mater calculated with n_{skull} = 1.5 and n_{cortex} = 1.33). Superficial cortical vasculature is resolved through the intact skull.

5.5. Discussion and Conclusion

Currently, system sensitivity is highly limited due to detector and light source noise. Also, the extended InGaAs camera used here had a cutoff at 2.2 μm, the center of the NIR optical window of interest. Furthermore, not all optical components used were optimized for 2.1 μm, further reducing sensitivity. For instance, the scan lens (LSM02/LSM03) in sample arm has 64%/42% double pass loss. Customized optics would improve the maximal sensitivity. The sensitivity could also be improved by a swept source system with lower losses and dual-balanced detection. A shot noise limited, low-loss system could achieve >100 dB sensitivity. For skull water content, the potential role of collagen absorption merits further investigation. Also, a cortical water volume fraction of 60-70% is slightly lower than expected. In the future, weighting of water absorption coefficients to account for the finite spectral width of each sub-band can improve quantitative accuracy. Better a priori information about scattering power would also improve accuracy.

In summary, a novel OCT microscope operating in the 2.2 μm spectral window was demonstrated for non-invasive *in vivo* imaging of the rodent brain. Though 2.2 μm is not often used for biological imaging due to high water absorption, we showed *in vivo* that for bone, a low water content biological tissue, 2.1 μm actually has lower OCT attenuation than 1.3 μm. Despite limited system performance, intrinsic benefits of the 2.2 μm window were identified, including lower cranial bone attenuation, more immunity to multiple scattering, and the ability to spectroscopically quantify tissue water content.

5.6. Acknowledgements

We acknowledge support from the National Institutes of Health (NIH) (NS094681, EB023591, NS105043, EY028287). We also thank Dr. Alfredo Dubra (Stanford University) for material support.

Chapter 6 Conclusions and Future Directions

6.1. Conclusions

Optical coherence tomography (OCT) has developed into a powerful tool and has been applied to many clinical and research areas such as ophthalmology, gastroenterology, cancer biology, neuroscience, as well as other fields. With a broadband spectrum, OCT achieves high spatial resolution, which enables it to resolve fine structures such as the capillary network, layers, neuronal cells, etc., noninvasively in tissue up to 1-2 mm deep. With a broadband spectrum, OCT can also obtain rich chromophore information such as hemoglobin concentration and water and lipid content, if appropriate wavelength ranges are used. Here, we focus on better understanding of light tissue interactions in different wavelength ranges or colors.

In the visible light range, we investigated novel ways of performing depth-resolved spectroscopic analysis of hemoglobin concentration and oxygen saturation. Rather than determining a depth-resolved spectrum, our method determined a depth-resolved autocorrelation function. This complex-valued autocorrelation function was then fit with a model that incorporates the spectral absorption characteristics of different chromophores assumed to be present in tissue. This method provided an alternative for obtaining the chromophore information within highly scattering vessels. This work benefits from the spectroscopic contrast of hemoglobin in the visible light range.

In the 1300 nm optical window, we investigated angular dependence of the retinal vessel visibility. We started from the optical coherence tomography angiography (OCTA) basics by taking a broader view of OCTA in the context of microvascular hemodynamics and light scattering. We then performed experimental investigation. A highly scattering plasma tracer that filled and visualized perfused retinal and choroidal vessels of rats in OCTA was injected to the rat tail vein. By comparing OCTA before and after tracer filling, we found that the OCTA signal from microvessels depended on angular orientation, making vertically-oriented vessels more difficult to visualize using intrinsic contrast alone. This work benefits from

reduced blood absorption and lower scattering in the 1300 nm window, which enables deeper penetration than shorter wavelength ranges.

In the 1700 nm window, we set a new standard for deep, minimally invasive, high resolution brain microscopy by reporting the first cellular-level *in vivo* optical coherence microscopy (OCM) system that spans the entire 1700 nm water absorption window. We showed *in vivo* optical biopsy of entire cortex and some sub-cortical regions of the mouse brain, performed through a thinned skull preparation. We presented direct data on chromatic dispersion at >1600 nm, and the first dispersion comparison of D_2O and H_2O (potentially important for three photon microscopy), as well as the first report of a new dispersion compensation method in high NA OCM that works by narrowing the path length distribution. We also exhibited detailed spectroscopic signal analysis that supports the ability to quantify both brain water and lipid content. In an Alzheimer's disease model, we confirmed the appearance of severe pathology in deep cortex but not in superficial cortex, with corresponding histology. This work benefits from lower total attenuation and usage of the entire 1700 nm window.

In the 2200 nm window, contrary to conventional wisdom, we demonstrated an OCT system for *in vivo* imaging of the rodent brain. We showed *in vivo* that at 2100 nm (system central wavelength), OCT signal was actually attenuated less in cranial bone than at 1300 nm, a more common wavelength for brain microscopy. Both wavelengths generated OCT angiograms of comparable quality through the intact rat cranium, while multiple scattering tails beneath vessels were reduced at 2100 nm. We also presented that the 2200 nm optical window enabled direct spectroscopic OCT assessment of tissue water content. We conclude that with further optimization, 2200 nm OCT will have distinct advantages in low water content tissue such as bone, and potentially also in applications where extensive averaging is possible to compensate absorption losses. This work benefits from further reduced scattering in low water content tissue.

Implementation of OCT in one wavelength range is not simply transferrable to another, and here we provide our considerations and experience in system optimization and light tissue interaction when moving to a new wavelength range. In summary, this thesis has advanced chromophore quantification in the visible light

range, demonstrated orientation dependence of the vessel signal in the 1300 nm window, and presented a leap forward of emerging colors for rodent brain imaging in the 1700 nm and 2200 nm window.

6.2. Discussion and Future Directions

6.2.1. 1700 nm Optical Window

While the 1700 nm OCM system in this thesis has shown great potential for visualizing deep brain structures noninvasively in cellular level, it is not fully optimized. One limitation is the system sensitivity. Due to the light source and detector noise, the system is not operated in the shot noise limit. Future improvements can utilize balanced detection[235,236] with two spectrometers to suppress the light source noise further and double the signal detection. With higher sensitivity, we anticipate better visualization of mouse sub-cortical cellular features.

Currently, the system incorporates the coherence gate with the confocal gate to ensure cellular resolution in both axial and transverse directions. One disadvantage of tightly focused beam is the short depth-of-focus (DOF). Therefore, the sample needs to be scanned sequentially in depth and then the data needs to be combined to synthesize a whole imaging volume, which is not efficient enough for capturing dynamic information such as blood flow. Future improvements can alleviate this limitation by applying extended-DOF engineering techniques[211,237], or implementing the system in full field[238] regime to reduce the overall data acquisition cost.

The 1700 nm OCM system has shown Alzheimer's disease (AD) related features such as plaques and myelin degeneration deep in cortex, with the 14-month-old 5xFAD transgenic mouse. In the future, the system can be applied to answer disease related questions. For instance, it can be used to observe early start and changes of the brain cellular structure over age in AD mouse. Meanwhile, it can also observe disease treatment effects. With a lower NA sample objective or with extended-DOF techniques, then vascular dynamics in deep cortex and sub-cortical region can also be obtained for better understanding of the disease

progression. Deep imaging can also aid disease studies in other highly scattering and water-rich tissues, such as skin.

6.2.2. 2200 nm Optical Window

In this thesis, advantages of the 2200 nm optical window for *in vivo* imaging especially for those low water content tissue, has been demonstrated, but not to the full extent. The system uses a supercontinuum source, which is highly noisy in the wavelength range, and an extended InGaAs detector, which is noisy and has a cutoff at 2200 nm. In the future, when technical improvements are on the horizon, then this window should be revisited for its *in vivo* imaging benefits. Nevertheless, with the current unoptimized sensitivity, the system can still provide useful information of superficial cortical structures and vasculature map through the intact rat skull. In addition, water absorption varies significantly within the window, making water content quantification easily accessible. In the future, applications such as post traumatic brain injury (TBI) water content together with local vascular changes monitoring, might be of interest[239,240].

6.2.3. Emerging colors for broader *in vivo* tissue imaging applications

Newer contrast can be added. 1700 nm deep tissue imaging can be conducted in high water content tissue, but for the imaging objects which have low reflectivity than surrounding tissue, then exogenous contrast can be added to generate the OCT signal. For instance, Si et al.[241] and Keahey et al.[242] have added gold nanobipyramids to lymphatic vessels to study the tumor angiogenic lymphatic vessels and lymph nodes. Similarly, contrast agents can also be applied to the 1700 nm optical window.

Human subjects can be imaged. The 1700 nm deep tissue imaging technique can also be made into the probe form, so tubular structures of human organs can be imaged. Li et al.[37,80] used the window partially (due to the detector cutoff) and applied it to human subjects. With our OCM design which implements the entire 1700 nm window, we anticipate improvements in 3D resolution and image quality, for better understanding of clinical problems.

Engineering improvements can be incorporated. Deep tissue imaging is attractive but also challenging. As imaging depth increases, probability of multiple scattering increases for the 1700 nm window, though lower than shorter wavelengths. To suppress or correct the wavefront error, Wu et al.[243] and Liu et al.[244] presented computation adaptive optics (CAO) to recover field information in out-of-focus regions in *ex vivo* tissue, therefore the focal step and acquisition data size was reduced and the tissue induced lower-order aberration was corrected. When translating CAO to *in vivo* imaging, the challenge of animal motion induced phase instability arises, but the method still remains promising if phase registration methods[244] can be applied.

In conclusion, this thesis investigated new and emerging OCT "colors," or wavelength ranges, through a series of demonstrative studies in mice and rats. This thesis sets a new standard for deep, minimally invasive, high resolution brain microscopy by reporting the first cellular-level *in vivo* optical coherence microscopy system that spans the entire 1700 nm water absorption window. The unprecedented depth for cellular-scale brain imaging proves actual benefits of long wavelength for deep imaging. In addition, contrary to conventional wisdom, this thesis proves benefits of the 2200 nm window for *in vivo* imaging, for the first time. With emerging improvements in optical components, engineering techniques, and imaging methods, we look forward to better understanding of biological systems, and applications for clinical use.

Chapter 7 Appendix

7.1. Supplementary Note 1: Chromatic Dispersion Compensation

As the optical coherence microscopy (OCM) spectrum spanned a broad spectral range from 1560 to 1820 nm (**Fig. S1A**), chromatic dispersion must be addressed to optimize axial image resolution. Dispersion mismatch between the sample and reference arms induces a nonlinearity in the spectral phase, so the point spread function (PSF) is chirped and broadened (**Fig. S1B-C**). Numerical dispersion compensation in post-processing can remove this spectral phase and optimize the OCM image quality. Unfortunately, reliable published data for dispersion of heavy water (D_2O) and water (H_2O) in this wavelength range are lacking, and it is uncertain if dispersion changes during focus translation as D_2O is replaced by brain tissue along the optical path. Image-based metrics to optimize numerical dispersion compensation include image sharpness[19], local image contrast[245] and alignment of subband images[52]. However such approaches are challenging to implement in images that lack well-defined features.

We empirically observed that optimal dispersion compensation minimized the width of the distribution of path lengths around the nominal focus, which we called the "apparent focal width (AFW)". Remarkably, this observation held even when this distribution was significantly broadened due to light scattering while focusing deep into the sample (**Fig. S1D**). Based on this observation, we chose to optimize numerical dispersion compensation by minimizing the apparent focal width. The nonlinear spectral phase compensation ($\emptyset_{NL}$) is:

$$\phi_{NL} = \frac{1}{2} d_2 (\omega - \omega_0)^2 + \frac{1}{6} d_3 (\omega - \omega_0)^3, \tag{6.1}$$

where ω is the angular optical frequency, ω_0 represents the central optical frequency, and d_2 and d_3 are coefficients compensating the group delay dispersion and third-order dispersion mismatches between the sample and reference arms, respectively. Note that units of d_2 and d_3 are s^2/rad and s^3/rad^2,

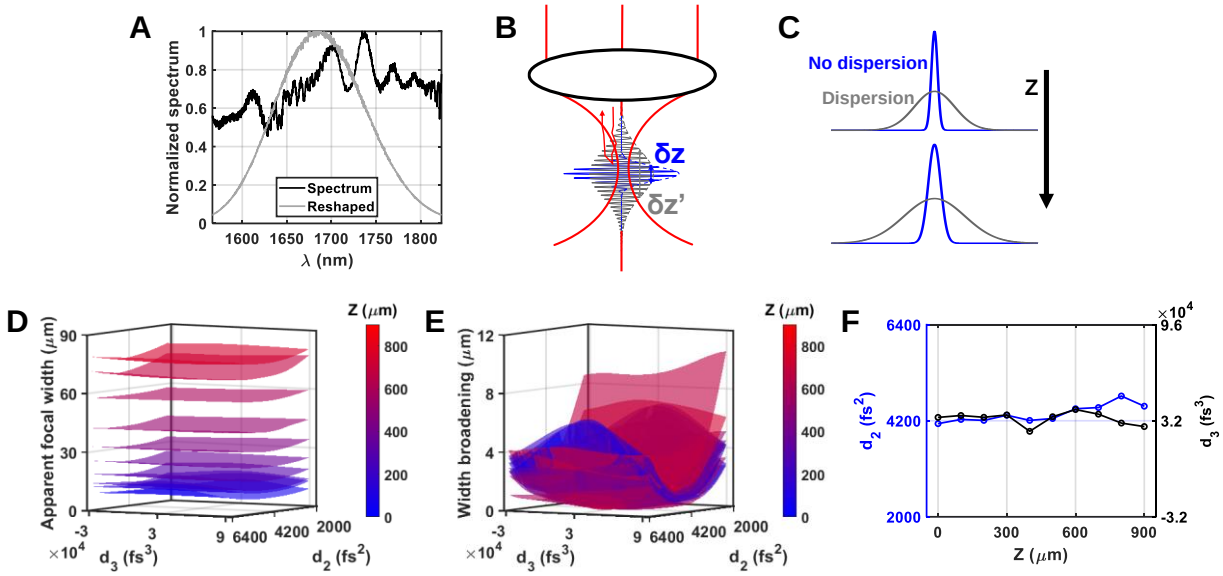

Fig. S1. Proposed method of numerical dispersion compensation in high numerical aperture (NA) OCM. (A) Registered reference spectrum (black). For mouse brain imaging, the spectrum is reshaped to be Gaussian (gray) with a 120 nm FWHM. (B) Chromatic dispersion induces a nonlinearity in the spectral phase, so the point spread function (PSF) is chirped and broadened (gray, $\delta z'$) compared to the ideal case with no dispersion (blue, δz). Multiply scattered paths (red) represent an additional source of broadening. (C) Thus, the width of the distribution of OCM depths (i.e., path length divided by 2) increases with focal depth (Z) due to multiple scattering (blue), and uncompensated dispersion results in further broadening (gray). The width of the distribution of OCM depths suggests optimal dispersion compensation coefficients, as seen from visualizations of the apparent focal width (D) and relative width broadening (E) at different focal depths. (F) The optimal second-order dispersion compensation coefficient (d_2) increases slightly with depth while changes in the third-order coefficient (d_3) are not detectable.

respectively, so $\emptyset_{NL}$ will be read as rad, but to be consistent with convention in the field, s^2 and s^3 were used.

For given values of d_2 and d_3, numerical calculation of the apparent focal width is:

$$AFW(d_2, d_3) = \frac{1}{M}\sum_{j=1}^{M} W_j, \tag{6.2}$$

where W_j is the full width at X_j% of the maximum PSF value. For this work, X_j values from 60% to 85% with 1% interval were used; therefore, $M = 26$. For each depth, width broadening (WB) is defined as:

$$WB = AFW(d_2, d_3) - AFW_0, \tag{6.3}$$

where minimum apparent focal width (AFW_0) is subtracted from all AFW values. Surface plots (grid search) indicate changes of AFW and WB with coefficients d_2 and d_3 at different focal depths (**Fig. S1D-**

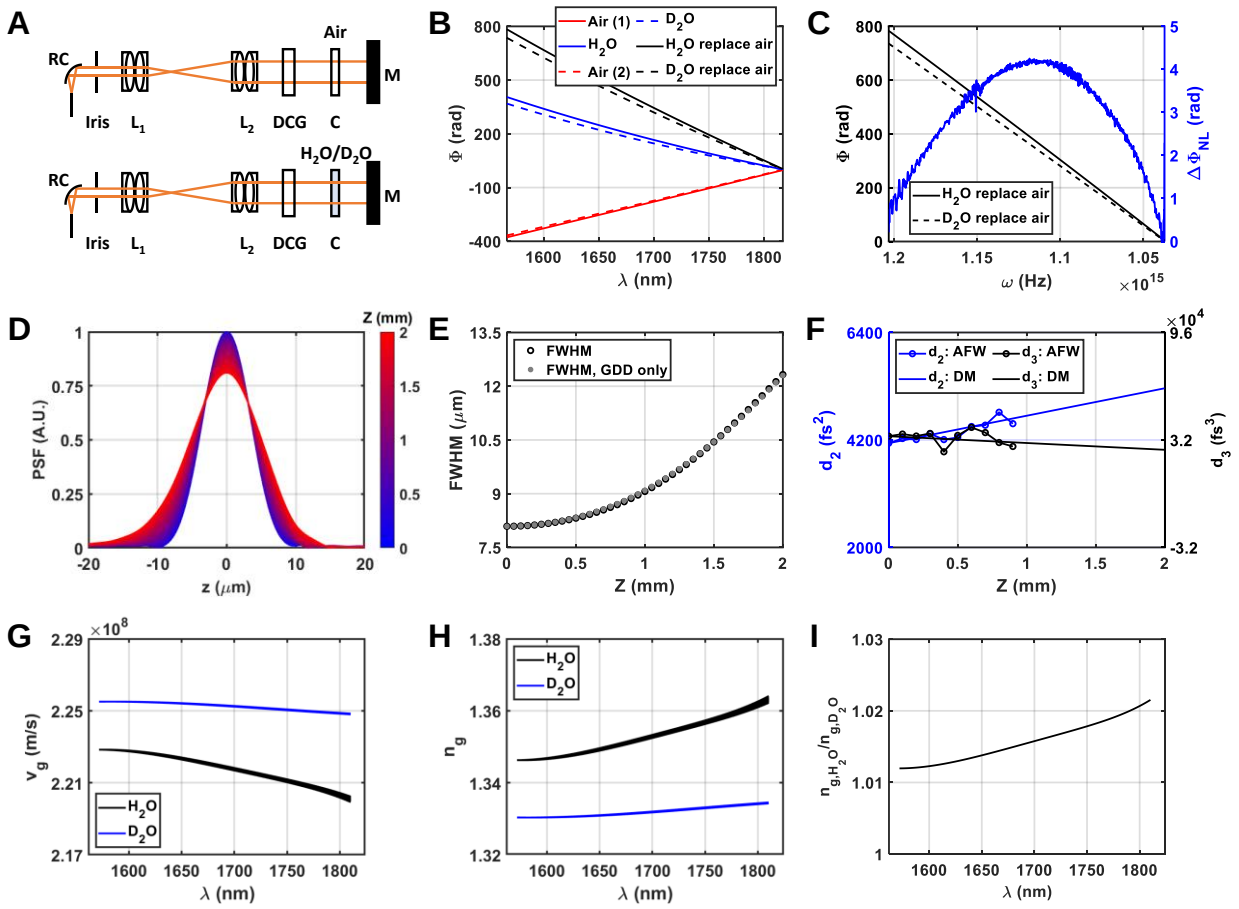

Fig. S2. Chromatic dispersion in the 1700 nm optical window. (A) Reference arm setup for dispersion measurements (sample arm not shown). The cuvette is either empty (filled with air, top panel) or filled with H_2O or D_2O (bottom panel). RC: reflective collimator; L_1, L_2: lenses (achromatic doublet pairs); DCG: dispersion compensation glass; C: cuvette; M: mirror. (B) Spectral phase (ϕ) of interferogram when a 2 mm cuvette in the reference arm is filled with H_2O (blue solid line), D_2O (blue dashed line) and air (red lines). Due to dispersion mismatch between arms, only phase changes between conditions are analyzed. Spectral phase changes when H_2O (black solid line) or D_2O (black dashed line) replaces 4 mm air (double pass path length), versus wavelength (B) and angular optical frequency (C), with the latter revealing a nonlinear spectral phase induced by replacing D_2O with H_2O [blue curve in (C)]. PSF axial profiles (D) and FWHMs (E) as H_2O replaces D_2O shows degradation of axial resolution up to 2 mm depth, as expected during deep focusing in OCM without compensating focus-dependent dispersion. GDD: group delay dispersion. (F) Optimized depth-dependent second (d_2) and third-order (d_3) dispersion compensation values obtained from dispersion measurement (DM) agree well with the apparent focal width (AFW) analysis (reproduced from Fig. S1f). Group velocity (G, v_g) and group refractive index (H, n_g) of H_2O (black) and D_2O (blue) obtained from spectral phase measurements. Calibrated limits of the system wavelength range are 1566.7 ± 2.1 and 1817.3 ± 2.8 nm. Shaded areas in (G)-(H) represent the range of solutions, accounting for wavelength calibration errors. (I) Group refractive index ratio of H_2O to D_2O.

E). Final optimized d_2 and d_3 values obtained by fminsearch[246] are consistent with grid search results. The fminsearch finds parameters to minimize AFW iteratively, requiring around 30 cycles to converge. As shown in **Fig. S1F**, optimum second-order dispersion compensation value increases by ~507 fs^2, while

systematic changes in the third-order value are undetectable, as focal depth increases from 0 to 900 μm. This suggests that second-order dispersion dominates PSF broadening as brain tissue replaces D_2O along the optical path. This empirical result is directly confirmed in the next section (**Fig. S2**).

7.2. Supplementary Note 2: Dispersion Measurements of H_2O and D_2O Over the Entire 1700 nm Optical Window

Besides empirically assessing the dispersion *in vivo* in brain tissue via the AFW in the previous section, we also used the 1700 nm OCM system to measure the dispersion generated as H_2O directly replaces D_2O in a cuvette. While this approach enabled a direct assessment of dispersion differences between H_2O and D_2O, without the complication of scattering tissue, it is important to keep in mind that brain tissue is only ~75% water and its chromatic dispersion may differ from pure H_2O.

Briefly, a 2 mm cuvette was inserted into the reference arm for dispersion measurements[247]. The spectral phase of the OCM interferogram was determined (**Fig. S2A**) when the cuvette was empty (filled with air, top panel) or filled with either H_2O or D_2O (bottom panel). The spectral phases were subtracted to yield:

$$\Phi = 2\left[k_{medium}(\omega) - k_{air}(\omega)\right]L + \Phi_{res.}, \tag{6.4}$$

where Φ is the spectral phase change between the medium (H_2O or D_2O) and air, k_{medium} and k_{air} are medium and air wavenumbers, respectively, ω is optical angular frequency, L is the cuvette length (2 mm), and $\Phi_{res.}$ is an unknown residual phase drift. As shown in **Fig. S2B-C**, the spectral phase change caused by replacing 2 mm (4 mm double pass) air with H_2O (black solid line) versus D_2O (black dashed line) are not the same. The nonlinear part of the spectral difference ($\Delta\Phi_{NL}$, blue curve), representing the difference between H_2O and D_2O, is essentially what causes PSF broadening (**Fig. S2C**). With this measured nonlinear phase, PSF broadening was predicted as the OCM focusing depth increases from 0 to 2 mm (4 mm double pass) deep in water (**Fig. S2D-E**). Second-order or group delay dispersion (GDD) was shown to be dominant (**Fig. S2E**). Importantly, the *ex vivo* measurements of dispersion when H_2O replacing D_2O agree with results of optimized *in vivo* dispersion correction (**Fig. S2F**). Also, as suggested by the larger optical

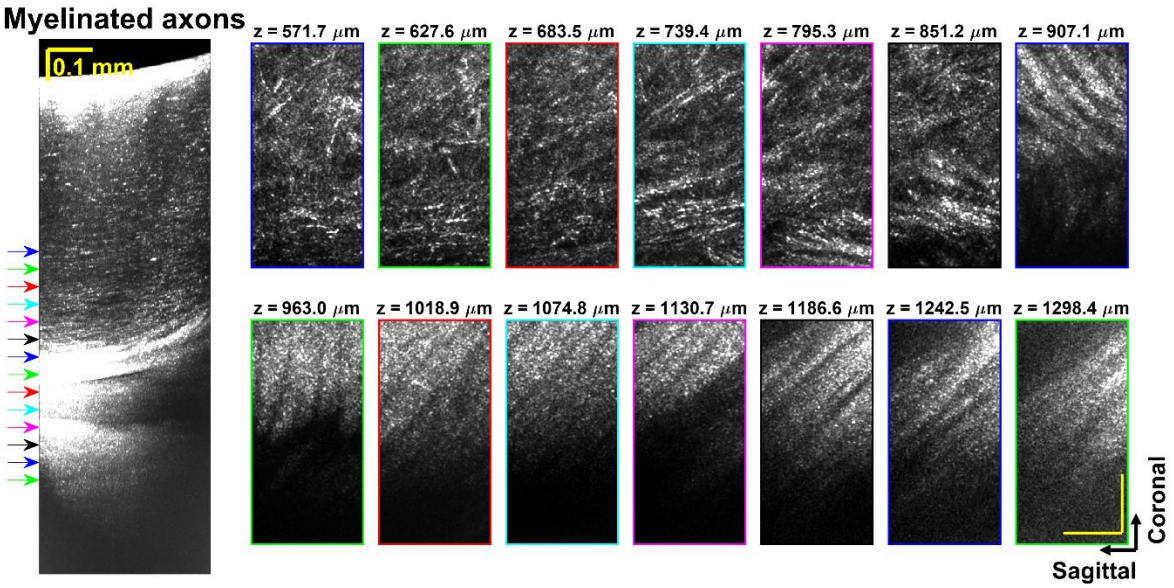

Fig. S3. *In vivo* visualization of myeloarchitecture. Outline colors of *en face* images correspond to arrow colors on the coronal image on the left, indicating projection locations. Axial projection depth: 11.2 µm. Coronal slice projection thickness: 190 µm. Scalebars represent 0.1 mm and apply to all the *en face* images.

phase change across the spectrum, the group refractive index ($c \times \partial k_{medium}/\partial\omega$, where c is the speed of light) of H_2O was found to be 1.012 to 1.022 times that of D_2O across the spectrum (**Fig. S2G-I**).

7.3. Supplementary Note 3: *In Vivo* Biopsy: Myeloarchitecture Pattern

Here, we also show variations of myeloarchitecture pattern from mid-cortical to sub-cortical regions using OCM *in vivo* biopsy. As shown in **Fig. S3**, many short, oblique axons present in mid cortex ($Z < 650\ \mu m$), therefore, they appear as individuals with different orientations in transverse planes; whereas in deeper cortical layer ($650\ \mu m < Z < 900\ \mu m$), axons orient in the antero-posterior direction, with few exceptions, therefore, they show up as parallel groups perpendicular to the coronal plane[248]. In corpus callosum and deeper regions ($Z > 900\ \mu m$), large fiber bundles form and their orientations vary with depth.

7.4. Supplementary Note 4: Estimation of Cortical Composition

Here, we show the derivation of subband OCM signal ratio for local lipid component change estimation. The OCM signal at focal depth Z and wavelength λ is given by:

$$I_{OCM}(Z,\lambda) = \mu_b(Z,\lambda) I_0(\lambda) e^{-2\int_0^Z \mu_t(u,\lambda)du}, \tag{6.5}$$

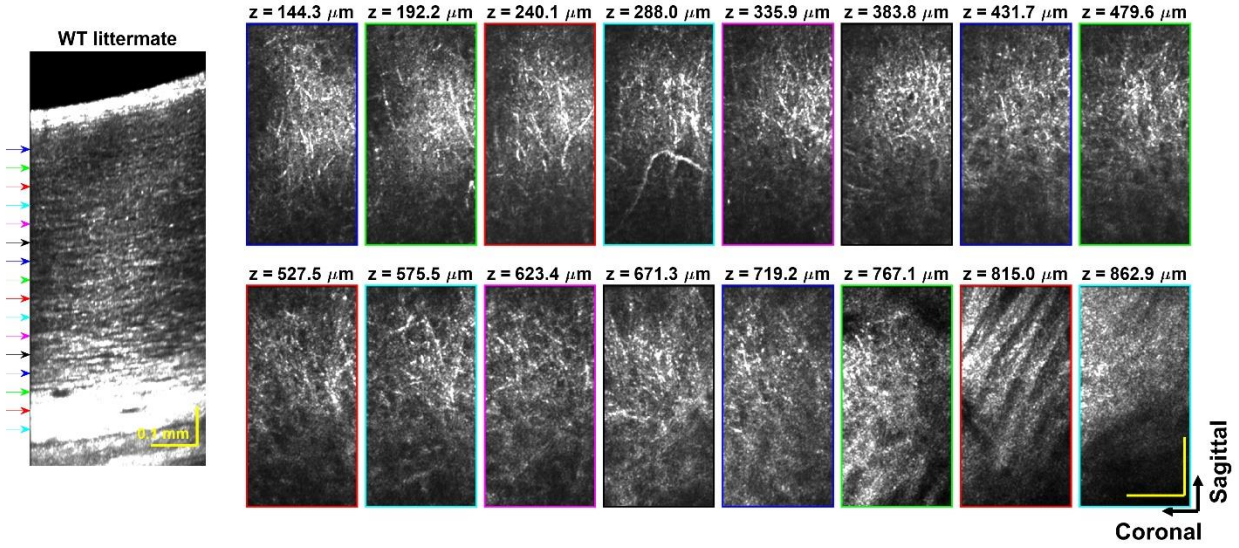

Fig. S4. 3D biopsy of the WT littermate. Transverse images formed by processing to enhance plaques, similar to Figure 4-10E. Outline colors of *en face* images correspond to arrow colors on the sagittal images on the left, indicating projection locations. Sagittal slice projection thickness: 17.8 µm. Axial projection depth: 16.0 µm. Scalebars represent 0.1 mm and apply to all the *en face* images.

where μ_b represents the backscattering coefficient, I_0 is the reference OCM signal which is typically set at the cortical surface, and μ_t is the total attenuation coefficient. The signal ratio of two subbands is:

$$\alpha = \frac{I_{OCM}(Z,\lambda_1)}{I_{OCM}(Z,\lambda_2)} = \frac{I_0(\lambda_1)\mu_b(Z,\lambda_1)}{I_0(\lambda_2)\mu_b(Z,\lambda_2)} e^{2\int_0^Z [\mu_t(u,\lambda_2)-\mu_t(u,\lambda_1)]du}. \tag{6.6}$$

The natural logarithm of the signal ratio is:

$$\ln(\alpha) = C_1 + \ln[\frac{\mu_b(Z,\lambda_1)}{\mu_b(Z,\lambda_2)}] + 2\int_0^Z [\mu_t(u,\lambda_2) - \mu_t(u,\lambda_1)]du, \tag{6.7}$$

where C_1 is the reference subband ratio constant. Assuming backscattering ratio of two subbands is fixed with depth, the derivative of ln (α) with respect to Z becomes:

$$\frac{d\ln(\alpha)}{dZ} = 2[\mu_t(Z,\lambda_2) - \mu_t(Z,\lambda_1)]. \tag{6.8}$$

We recall that $\mu_t(Z,\lambda)$ consists of scattering attenuation $[\mu_{t,s}(Z,\lambda)]$, water absorption $[f_w(Z)\mu_{a,w}(\lambda)]$, and lipid absorption $[f_l(Z)\mu_{a,l}(\lambda)]$:

$$\mu_t(Z,\lambda) = \mu_{t,s}(Z,\lambda) + f_w(Z)\mu_{a,w}(\lambda) + f_l(Z)\mu_{a,l}(\lambda), \tag{6.9}$$

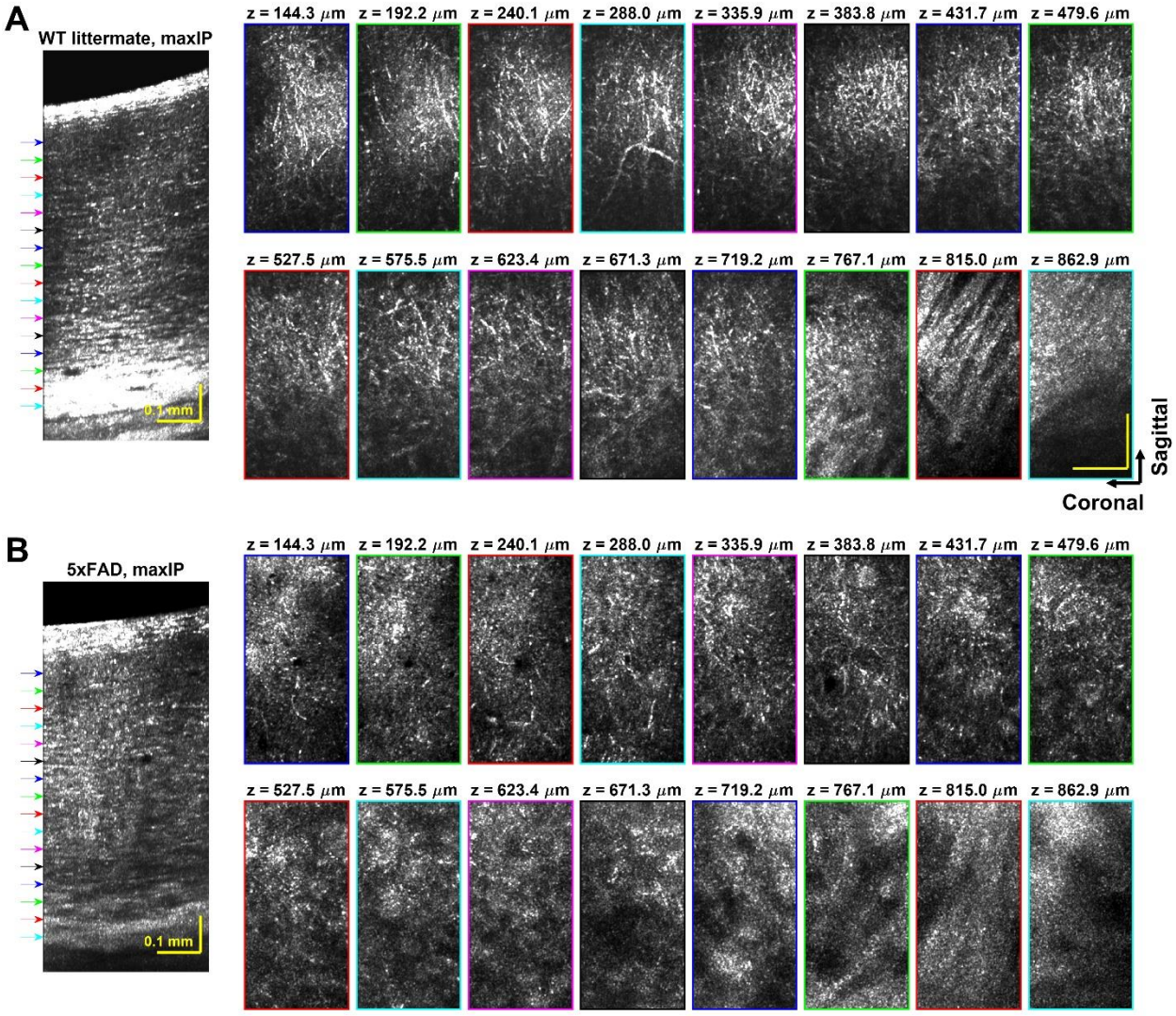

Fig. S5. Maximum intensity projection (maxIP) images of the WT littermate (A) and the 5xFAD mouse (B). Outline colors of *en face* images correspond to arrow colors on the sagittal images on the left, indicating projection locations. Sagittal slice projection thickness: 17.8 µm. Axial projection depth: 16.0 µm. Scalebars represent 0.1 mm and apply to all the *en face* images.

where f_w and f_l represent water and lipid volume fraction, and $\mu_{a,w}$ and $\mu_{a,l}$ are water and lipid absorption coefficient, respectively. In summary, the total attenuation difference between the two subbands determines slope of $\ln(\alpha)$, which can help infer changes in tissue components with cortical depth.

7.5. Supplementary Note 5: OCM Imaging of Wild Type Littermate versus AD Mouse

In contrast to the five-familial Alzheimer's disease (5xFAD) transgenic mouse, its wild type (WT) littermate does not present features such as plaques, tissue loss and myelin degeneration (**Fig. S4**).

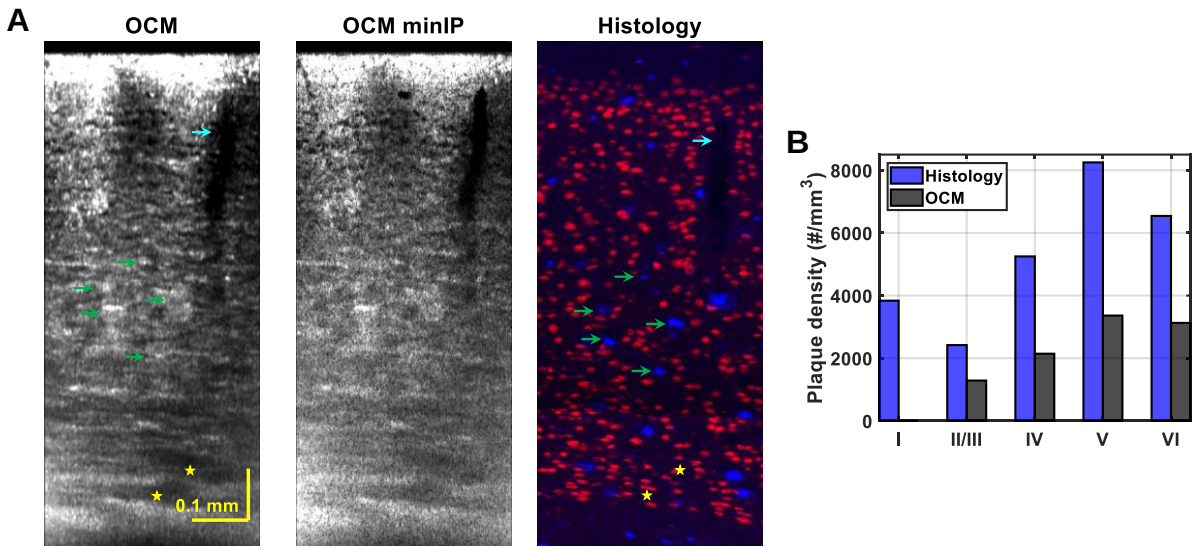

Fig. S6. Comparison of *in vivo* OCM imaging with *ex vivo* histology. (A) *In vivo* OCM imaging (left and middle) versus *ex vivo* histology (right). In the histological image, neuronal cell bodies are delineated by anti-NeuN staining (red), while amyloid plaques are highlighted by FSB staining (blue). Corresponding anatomical features include a blood vessel (cyan arrow), plaques (green arrows), and possible demyelination (yellow asterisks). OCM slice summation or minimum intensity projection (minIP) thickness: 17.8 µm. Histology slice thickness: 4 µm. Scalebars represent 0.1 mm and apply to all images. (B) Although differences are observed between OCM and histology, both modalities depict increasing plaque load in deep cortical layers.

Myelinated axons are clearly visible in the WT littermate (**Fig. S5A**), while appearing diminished in deeper layers of the AD mouse (**Fig. S5B**).

7.6. Supplementary Note 6: Comparison of *In Vivo* OCM Imaging with *Ex Vivo* Histology

A comparison between *in vivo* OCM and the corresponding anti-NeuN and FSB-stained histology was performed in the AD mouse. Briefly, after OCM imaging, the mouse was immediately sacrificed, and the brain was excised and fixed with 10% formalin. Then the fixed sample was embedded in Paraffin and sliced at 4 microns for imaging. Histology slices were co-stained with anti-NeuN (Abcam, MA, USA) and FSB (Sigma-Aldrich, MO, USA), and imaged with a commercial microscope (Nikon, NY, USA) at 10x magnification. Exposure time and gamma were adjusted to optimally visualize NeuN and FSB in individual images, which were combined as red and blue channels, respectively, of a single color image. Anatomical features depicted by the two modalities correspond (**Fig. S6A**). A hyporeflective shadow in OCM corresponds with a blood vessel (cyan arrow). Hyperscattering clusters in OCM correspond with FSB-labelled plaques (green arrows), though smaller FSB-labelled plaques are not always visualized on OCM.

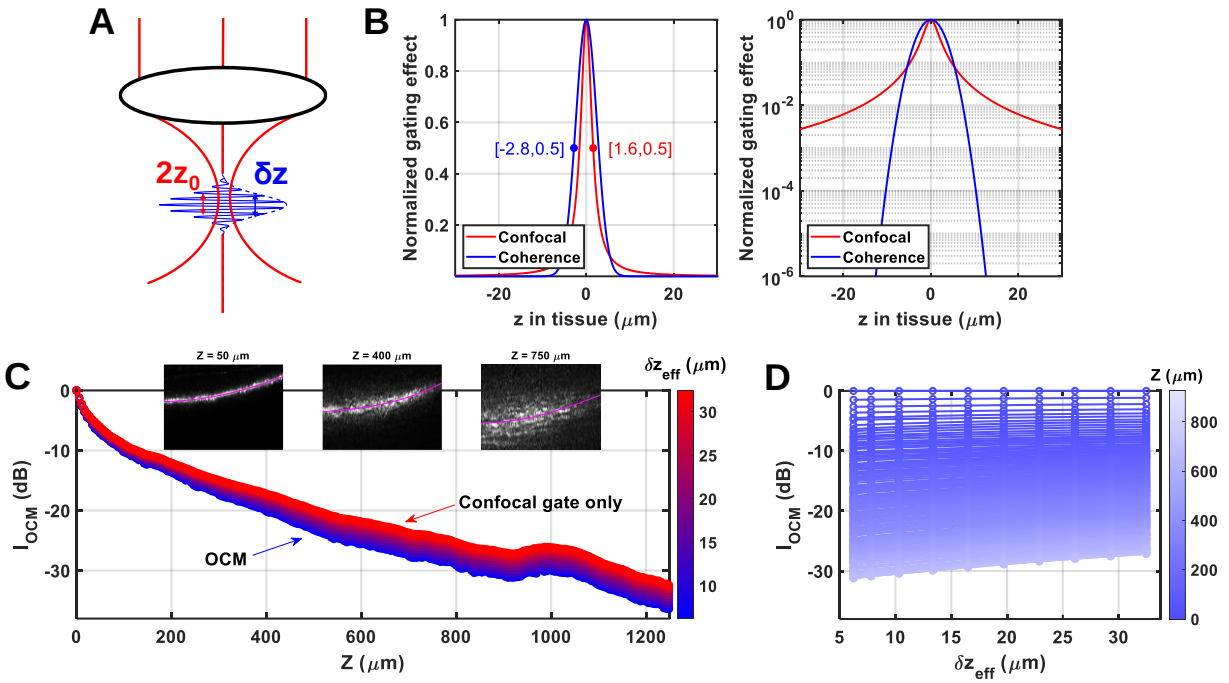

Fig. S7. Coherence gating complements confocal gating to reject multiply scattered light. (A) Coherence gate (blue, δz) and confocal gate (red, $2z_0$). (B) Intensity profiles of the two gates, shown in linear (left panel) and logarithmic (right panel) scales. (C-D) With a digitally-broadened coherence gate (δz_{eff}), the OCM signal decays slower with depth, suggesting inclusion of more multiply scattered light. Note that a large δz_{eff} compared to $2z_0$ results in only a confocal gate (red in C). Insets in (C) show broadening in OCM depth (proportional to path length) about the detected focus, suggesting that with a deep tissue focus, relatively more multiply scattered light passes the confocal gate.

NeuN is seen in regions corresponding to hyporeflective regions in OCM (yellow asterisks), therefore low scattering in OCM is proposed to be related with demyelination, rather than neuronal loss. Plaque density was estimated both from the OCM volume and from histology (**Fig. S6B**). OCM appears to underestimate the plaque density relative to histology, but does correctly depict the trend of increasing plaque load with cortical depth (**Fig. S6B**). Differences between plaque densities estimated by OCM and histology could be due to the imaging contrast[249,250]. In OCM, the ability to detect plaques is affected by local contrast between the plaque backscattering, determined by composition and morphology, and the surrounding tissue backscattering background. Therefore, it is possible that our OCM is detecting a subpopulation of the amyloid plaques highlighted by FSB.

7.7. Supplementary Note 7: Benefits Over Confocal

Compared to confocal microscopy[206], the OCM approach better rejects multiply scattered and out-of-focus light. Coherence gating is achieved by a broadband light source (**Fig. S7A**, blue, δz) and confocal gating is achieved by a high numerical aperture (NA) water immersion objective (**Fig. S7A**, red, $2z_0$). Intensity profiles of the two gating effects in tissue show that confocal gating has a narrower full-width-at-half-maximum (FWHM). However, we notice that the asymptotic decay of the confocal gate is more gradual than that of the coherence gate (**Fig. S7B**), suggesting that the coherence gate can further enhance the confocal gate.

The OCM approach provides a path length filter to selectively remove out-of-focus and multiply scattered light. Here, we demonstrate this concept by investigating the OCM signal slope as a function of the effective coherence gate width (δz_{eff}). At each focus location (Z), OCM intensity signal is 3D summed with different axial ranges, where δz_{eff} is the width of the coherence intensity profile convolved with a rectangular function that delineates the axial (depth) summation range. As δz_{eff} increases, OCM signal decays slower with depth (**Fig. S7C-D**), indicating increased detection of multiply scattered light[29]. This suggests that an OCM system that achieves high axial resolution by utilizing the entire water absorption window at 1700 nm rejects multiply scattered light more effectively than a system that only partially utilizes the 1700 nm window.

7.8. Supplementary Note 8: *In Vivo* Characterization of Resolution

While the system resolution was characterized *in vitro* in the main manuscript (**Figure 4-2**), resolution may degrade *in vivo* due to multiple scattering and aberrations. To assess lateral (transverse) resolution degradation *in vivo*, we relied on salient OCM features: cell bodies and myelinated axons. In the axial direction, we used broadening of the apparent focal width (AFW) as an indirect indicator of broadening due to multiple scattering, which is the main source of degradation of both the PSF and AFW when imaging deep, if dispersion is compensated (**Fig. S1**). For each focus location, AFW was estimated (**Fig. S8A-B**).

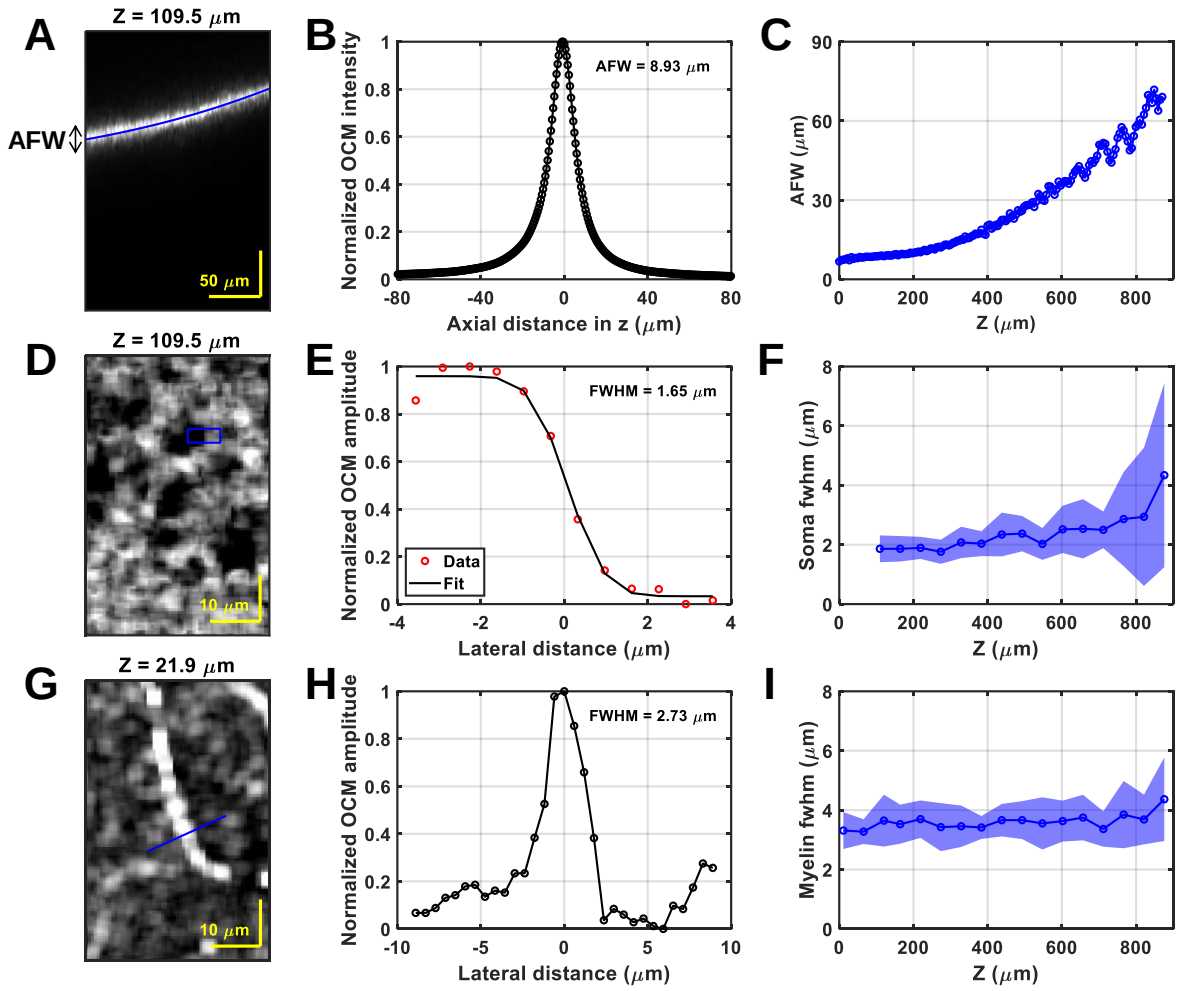

Fig. S8. Investigation of resolution degradation *in vivo*. Apparent focal width (AFW) (A-C), transverse FWHMs estimated from soma boundary profiles (D-F) and transverse FWHMs estimated from myelin profiles (G-I). The AFW (A), calculated similar to Fig. S1D based on the OCM intensity (B), shows a clear degradation with depth (C). To analyze the soma boundary, the amplitude in the blue boxed region in (D) is averaged along the vertical direction to generate the edge or step response (red circles, E), and then fitted with an error function (black line, E) to indirectly yield the lateral FWHM of the impulse response (E). The FWHM degradation with depth (F), with shaded regions representing standard deviations across 12 soma boundaries per depth, is subtle. To analyze myelin profiles, the amplitude profile perpendicular to the myelin axis (G) is calculated (H), and the lateral FWHM is determined directly (H). The degradation with depth (I), with shaded regions representing standard deviations across 92 axon cross sections per depth, is also subtle, consistent with (F).

AFW increases with a deeper focus (**Fig. S8C**). In the transverse direction, line profiles of neuronal cell body edges and myelin were used to indicate the lateral resolution. Neuronal cell bodies were emphasized by minimum intensity projection (**Fig. S8D**), while myelinated axons were emphasized by maximum intensity projection (**Fig. S8G**). Regions of interests (ROIs) from the cell body edges were selected (as shown in **Fig. S8D**) and averaged perpendicular to the cell body edge to generate the edge or step response.

Then, the data was fitted with an error function to indirectly yield the lateral FWHM of the point or impulse response (**Fig. S8E**). For myelin, FWHMs were extracted directly from line profiles perpendicular to the axon axis (**Fig. S8G-H**). For both the cell body and myelin, a slight increase with depth is observed (**Fig. S8F, I**), suggesting resolution degradation *in vivo*. Note that this analysis provides evidence of resolution degradation, not direct estimates of resolution, since minimum or maximum intensity projections were analyzed, and since the intrinsic widths of the myelinated axon and cell body edge were neglected.

References

1 Huang, D. *et al.* Optical coherence tomography. *Science* **254**, 1178-1181 (1991).

2 Fercher, A. F. Optical coherence tomography. *Journal of Biomedical Optics* **1**, 157-173 (1996).

3 Fercher, A. F., Drexler, W., Hitzenberger, C. K. & Lasser, T. Optical coherence tomography-principles and applications. *Reports on progress in physics* **66**, 239 (2003).

4 Vakoc, B. J. *et al.* Three-dimensional microscopy of the tumor microenvironment in vivo using optical frequency domain imaging. *Nat Med* **15**, 1219-1223 (2009).

5 Srinivasan, V. J. *et al.* Rapid volumetric angiography of cortical microvasculature with optical coherence tomography. *Optics letters* **35**, 43-45 (2010).

6 Wang, R. K. *et al.* Three dimensional optical angiography. *Optics express* **15**, 4083-4097 (2007).

7 Zhu, J., Merkle, C., Bernucci, M., Chong, S. & Srinivasan, V. Can OCT angiography be made a quantitative blood measurement tool? *Applied Sciences* **7**, 687 (2017).

8 Leitgeb, R. A., Werkmeister, R. M., Blatter, C. & Schmetterer, L. Doppler optical coherence tomography. *Prog Retin Eye Res* **41**, 26-43 (2014).

9 Srinivasan, V. J. *et al.* OCT methods for capillary velocimetry. *Biomedical optics express* **3**, 612-629 (2012).

10 Wang, Y. & Wang, R. Autocorrelation optical coherence tomography for mapping transverse particle-flow velocity. *Optics letters* **35**, 3538-3540 (2010).

11 Thouvenin, O. *et al.* Cell motility as contrast agent in retinal explant imaging with full-field optical coherence tomography. *Investigative ophthalmology & visual science* **58**, 4605-4615 (2017).

12 Lee, J. *et al.* Quantitative imaging of cerebral blood flow velocity and intracellular motility using dynamic light scattering–optical coherence tomography. *Journal of Cerebral Blood Flow & Metabolism* **33**, 819-825 (2013).

13 Liu, Z., Kurokawa, K., Zhang, F., Lee, J. J. & Miller, D. T. Imaging and quantifying ganglion cells and other transparent neurons in the living human retina. *Proceedings of the National Academy of Sciences* **114**, 12803-12808 (2017).

14 Robles, F. E., Wilson, C., Grant, G. & Wax, A. Molecular imaging true-colour spectroscopic optical coherence tomography. *Nat Photonics* **5**, 744-747 (2011).

15 Yi, J., Wei, Q., Liu, W., Backman, V. & Zhang, H. F. Visible-light optical coherence tomography for retinal oximetry. *Optics letters* **38**, 1796-1798 (2013).

16 Zhu, J., Freitas, H. R., Maezawa, I., Jin, L.-w. & Srinivasan, V. J. 1700 nm optical coherence microscopy enables minimally invasive, label-free, in vivo optical biopsy deep in the mouse brain. *Light: Science & Applications* **10**, 1-13 (2021).

17 Chong, S. P., Merkle, C. W., Leahy, C., Radhakrishnan, H. & Srinivasan, V. J. Quantitative microvascular hemoglobin mapping using visible light spectroscopic Optical Coherence Tomography. *Biomed Opt Express* **6**, 1429-1450 (2015).

18 Izatt, J. A., Choma, M. A. & Dhalla, A.-H. Theory of optical coherence tomography. *Optical Coherence Tomography: Technology and Applications*, 65-94 (2015).

19 Wojtkowski, M. *et al.* Ultrahigh-resolution, high-speed, Fourier domain optical coherence tomography and methods for dispersion compensation. *Optics express* **12**, 2404-2422 (2004).

20 Chong, S. P., Bernucci, M., Radhakrishnan, H. & Srinivasan, V. J. Structural and functional human retinal imaging with a fiber-based visible light OCT ophthalmoscope. *Biomedical optics express* **8**, 323-337 (2017).

21 Kho, A. M., Zhang, T., Zhu, J., Merkle, C. W. & Srinivasan, V. J. Incoherent excess noise spectrally encodes broadband light sources. *Light: Science & Applications* **9**, 1-9 (2020).

22 Zhang, T., Kho, A. M. & Srinivasan, V. J. In vivo morphometry of inner plexiform layer (IPL) stratification in the human retina with visible light Optical Coherence Tomography. *Frontiers in Cellular Neuroscience* **15** (2021).

23 Rubinoff, I. *et al.* Speckle reduction in visible-light optical coherence tomography using scan modulation. *Neurophotonics* **6**, 041107 (2019).
24 Beckmann, L. *et al.* In vivo imaging of the inner retinal layer structure in mice after eye-opening using visible-light optical coherence tomography. *Experimental Eye Research*, 108756 (2021).
25 Lichtenegger, A. *et al.* Spectroscopic imaging with spectral domain visible light optical coherence microscopy in Alzheimer's disease brain samples. *Biomedical optics express* **8**, 4007-4025 (2017).
26 Lichtenegger, A. *et al.* Assessment of pathological features in Alzheimer's disease brain tissue with a large field-of-view visible-light optical coherence microscope. *Neurophotonics* **5**, 035002 (2018).
27 Merkle, C. W. *et al.* Visible light optical coherence microscopy of the brain with isotropic femtoliter resolution in vivo. *Optics letters* **43**, 198-201 (2018).
28 Izatt, J. A., Hee, M. R., Owen, G. M., Swanson, E. A. & Fujimoto, J. G. Optical coherence microscopy in scattering media. *Optics letters* **19**, 590-592 (1994).
29 Jacques, S. L., Wang, B. & Samatham, R. Reflectance confocal microscopy of optical phantoms. *Biomedical optics express* **3**, 1162-1172 (2012).
30 Wieliczka, D. M., Weng, S. & Querry, M. R. Wedge shaped cell for highly absorbent liquids: infrared optical constants of water. *Applied optics* **28**, 1714-1719 (1989).
31 Hui, J. *et al.* Bond-selective photoacoustic imaging by converting molecular vibration into acoustic waves. *Photoacoustics* **4**, 11-21 (2016).
32 Nachabé, R. *et al.* Effect of bile absorption coefficients on the estimation of liver tissue optical properties and related implications in discriminating healthy and tumorous samples. *Biomedical optics express* **2**, 600-614 (2011).
33 Jacques, S. L. Optical properties of biological tissues: a review. *Physics in medicine and biology* **58**, R37 (2013).
34 Cuartas-Vélez, C., Veenstra, C., Kruitwagen, S., Petersen, W. & Bosschaart, N. Optical density based quantification of total haemoglobin concentrations with spectroscopic optical coherence tomography. *Scientific reports* **11**, 1-10 (2021).
35 Pi, S. *et al.* Retinal capillary oximetry with visible light optical coherence tomography. *Proc Natl Acad Sci U S A* **117**, 11658-11666 (2020).
36 Rubinoff, I. *et al.* Adaptive spectroscopic visible-light optical coherence tomography for human retinal oximetry. *bioRxiv* (2021).
37 Li, Y. *et al.* Intravascular optical coherence tomography for characterization of atherosclerosis with a 1.7 micron swept-source laser. *Scientific reports* **7**, 1-6 (2017).
38 Zhang, P. *et al.* In vivo optophysiology reveals that G-protein activation triggers osmotic swelling and increased light scattering of rod photoreceptors. *Proceedings of the National Academy of Sciences* **114**, E2937-E2946 (2017).
39 Lichtenegger, A. *et al.* Revealing brain pathologies with multimodal visible light optical coherence microscopy and fluorescence imaging. *Journal of biomedical optics* **24**, 066010 (2019).
40 Shi, L., Sordillo, L. A., Rodríguez-Contreras, A. & Alfano, R. Transmission in near-infrared optical windows for deep brain imaging. *Journal of biophotonics* **9**, 38-43 (2016).
41 Shi, L. & Alfano, R. R. *Deep imaging in tissue and biomedical materials: using linear and nonlinear optical methods*. (Pan Stanford, 2017).
42 Reinoso, R. F., Telfer, B. A. & Rowland, M. Tissue water content in rats measured by desiccation. *Journal of pharmacological and toxicological methods* **38**, 87-92 (1997).
43 Zhu, J., Chong, S. P., Zhou, W. & Srinivasan, V. J. Noninvasive, in vivo rodent brain optical coherence tomography at 2.1 microns. *Optics letters* **44**, 4147-4150 (2019).
44 Colley, C. S. *et al.* Mid-infrared optical coherence tomography. *Review of Scientific Instruments* **78**, 123108 (2007).
45 Liang, H., Lange, R., Peric, B. & Spring, M. Optimum spectral window for imaging of art with optical coherence tomography. *Applied Physics B* **111**, 589-602 (2013).
46 Povazay, B. *et al.* in *Coherence Domain Optical Methods in Biomedical Science and Clinical Applications VI.* 90-94 (International Society for Optics and Photonics).

47 Robles, F., Graf, R. N. & Wax, A. Dual window method for processing spectroscopic optical coherence tomography signals with simultaneously high spectral and temporal resolution. *Opt Express* **17**, 6799-6812 (2009).
48 Robles, F. E., Chowdhury, S. & Wax, A. Assessing hemoglobin concentration using spectroscopic optical coherence tomography for feasibility of tissue diagnostics. *Biomed Opt Express* **1**, 310-317 (2010).
49 Leitgeb, R. *et al.* Spectral measurement of absorption by spectroscopic frequency-domain optical coherence tomography. *Optics letters* **25**, 820-822 (2000).
50 Morgner, U. *et al.* Spectroscopic optical coherence tomography. *Opt Lett* **25**, 111-113 (2000).
51 Yi, J., Chen, S., Backman, V. & Zhang, H. F. In vivo functional microangiography by visible-light optical coherence tomography. *Biomedical optics express* **5**, 3603-3612 (2014).
52 Kho, A. & Srinivasan, V. J. Compensating spatially dependent dispersion in visible light OCT. *Optics letters* **44**, 775-778 (2019).
53 Srinivasan, V. *et al.* High-speed, high-resolution optical coherence tomography retinal imaging with a frequency-swept laser at 850 nm. *Optics letters* **32**, 361-363 (2007).
54 Bernucci, M. T., Merkle, C. W. & Srinivasan, V. J. Investigation of artifacts in retinal and choroidal OCT angiography with a contrast agent. *Biomedical optics express* **9**, 1020-1040 (2018).
55 Povazay, B. *et al.* Three-dimensional optical coherence tomography at 1050 nm versus 800 nm in retinal pathologies: enhanced performance and choroidal penetration in cataract patients. *Journal of biomedical optics* **12**, 041211 (2007).
56 Esmaeelpour, M. *et al.* Choroidal thinning in diabetes type 1 detected by 3-dimensional 1060 nm optical coherence tomography. *Investigative ophthalmology & visual science* **53**, 6803-6809 (2012).
57 Aneesh, A. *et al.* Multispectral in vivo three-dimensional optical coherence tomography of human skin. *Journal of biomedical optics* **15**, 026025 (2010).
58 Xu, J., Song, S., Men, S. & Wang, R. K. Long ranging swept-source optical coherence tomography-based angiography outperforms its spectral-domain counterpart in imaging human skin microcirculations. *Journal of biomedical optics* **22**, 116007 (2017).
59 Lee, K.-S. *et al.* Three-dimensional imaging of normal skin and nonmelanoma skin cancer with cellular resolution using Gabor domain optical coherence microscopy. *Journal of biomedical optics* **17**, 126006 (2012).
60 Srinivasan, V. J., Radhakrishnan, H., Jiang, J. Y., Barry, S. & Cable, A. E. Optical coherence microscopy for deep tissue imaging of the cerebral cortex with intrinsic contrast. *Optics express* **20**, 2220-2239 (2012).
61 Li, Y., Baran, U. & Wang, R. K. Application of thinned-skull cranial window to mouse cerebral blood flow imaging using optical microangiography. *Plos one* **9**, e113658 (2014).
62 Srinivasan, V. J. *et al.* Quantitative cerebral blood flow with optical coherence tomography. *Optics express* **18**, 2477-2494 (2010).
63 Li, Y. *et al.* Aging-associated changes in cerebral vasculature and blood flow as determined by quantitative optical coherence tomography angiography. *Neurobiology of aging* **70**, 148-159 (2018).
64 Merkle, C. W., Leahy, C. & Srinivasan, V. J. Dynamic contrast optical coherence tomography images transit time and quantifies microvascular plasma volume and flow in the retina and choriocapillaris. *Biomed Opt Express* **7**, 4289-4312 (2016).
65 Drexler, W. & Fujimoto, J. G. State-of-the-art retinal optical coherence tomography. *Progress in retinal and eye research* **27**, 45-88 (2008).
66 Proskurin, S. & Frolov, S. Visualization of blood vessels using optical coherence tomography. *Biomedical Engineering* **46**, 96-99 (2012).
67 Carrion, L. *et al.* Comparative study of optical sources in the near infrared for optical coherence tomography applications. *Journal of Biomedical Optics* **12**, 014017 (2007).

68 Sordillo, L. A., Pu, Y., Pratavieira, S., Budansky, Y. & Alfano, R. R. Deep optical imaging of tissue using the second and third near-infrared spectral windows. *Journal of biomedical optics* **19**, 056004 (2014).
69 Sharma, U., Chang, E. W. & Yun, S. H. Long-wavelength optical coherence tomography at 1.7 μm for enhanced imaging depth. *Optics express* **16**, 19712-19723 (2008).
70 Ishida, S., Nishizawa, N., Ohta, T. & Itoh, K. Ultrahigh-resolution optical coherence tomography in 1.7 μm region with fiber laser supercontinuum in low-water-absorption samples. *Applied physics express* **4**, 052501 (2011).
71 Ishida, S. & Nishizawa, N. Quantitative comparison of contrast and imaging depth of ultrahigh-resolution optical coherence tomography images in 800–1700 nm wavelength region. *Biomedical optics express* **3**, 282-294 (2012).
72 Jiao, Y. *et al.* InAs/InP (100) quantum dot waveguide photodetectors for swept-source optical coherence tomography around 1.7 μm. *Optics express* **20**, 3675-3692 (2012).
73 Tilma, B. W. *et al.* Integrated Tunable Quantum-Dot Laser for Optical Coherence Tomography in the 1.7 μm Wavelength Region. *IEEE Journal of Quantum Electronics* **48**, 87-98 (2011).
74 Kawagoe, H. *et al.* Development of a high power supercontinuum source in the 1.7 μm wavelength region for highly penetrative ultrahigh-resolution optical coherence tomography. *Biomedical optics express* **5**, 932-943 (2014).
75 Tanaka, M. *et al.* 1.7-μm spectroscopic spectral-domain optical coherence tomography for imaging lipid distribution within blood vessel. *Optics express* **23**, 6645-6655 (2015).
76 Chong, S. P. *et al.* Noninvasive, in vivo imaging of subcortical mouse brain regions with 1.7 μm optical coherence tomography. *Optics letters* **40**, 4911-4914 (2015).
77 Yamanaka, M., Teranishi, T., Kawagoe, H. & Nishizawa, N. Optical coherence microscopy in 1700 nm spectral band for high-resolution label-free deep-tissue imaging. *Scientific reports* **6**, 31715 (2016).
78 Kawagoe, H., Yamanaka, M., Makita, S., Yasuno, Y. & Nishizawa, N. Full-range ultrahigh-resolution spectral-domain optical coherence tomography in 1.7 μm wavelength region for deep-penetration and high-resolution imaging of turbid tissues. *Applied Physics Express* **9**, 127002 (2016).
79 Kawagoe, H., Yamanaka, M. & Nishizawa, N. Axial resolution and signal-to-noise ratio in deep-tissue imaging with 1.7-μm high-resolution optical coherence tomography with an ultrabroadband laser source. *Journal of biomedical optics* **22**, 085002 (2017).
80 Li, Y. *et al.* 1.7 micron optical coherence tomography for vaginal tissue characterization in vivo. *Lasers in surgery and medicine* **51**, 120-126 (2019).
81 Park, K. S., Shin, J. G., Qureshi, M. M., Chung, E. & Eom, T. J. Deep brain optical coherence tomography angiography in mice: in vivo, noninvasive imaging of hippocampal formation. *Scientific reports* **8**, 11614 (2018).
82 Yamanaka, M., Hayakawa, N. & Nishizawa, N. Signal-to-background ratio and lateral resolution in deep tissue imaging by optical coherence microscopy in the 1700 nm spectral band. *Scientific reports* **9**, 1-8 (2019).
83 Yamanaka, M., Hayakawa, N. & Nishizawa, N. High-spatial-resolution deep tissue imaging with spectral-domain optical coherence microscopy in the 1700-nm spectral band. *Journal of biomedical optics* **24**, 070502 (2019).
84 Cheung, C., Daniel, J., Tokurakawa, M., Clarkson, W. & Liang, H. Optical coherence tomography in the 2-μm wavelength regime for paint and other high opacity materials. *Optics letters* **39**, 6509-6512 (2014).
85 Cheung, C., Daniel, J., Tokurakawa, M., Clarkson, W. & Liang, H. High resolution Fourier domain optical coherence tomography in the 2 μm wavelength range using a broadband supercontinuum source. *Optics express* **23**, 1992-2001 (2015).
86 Israelsen, N. M. *et al.* Real-time high-resolution mid-infrared optical coherence tomography. *Light: Science & Applications* **8**, 1-13 (2019).

87 Leitgeb, R. *et al.* Spectral measurement of absorption by spectroscopic frequency-domain optical coherence tomography. *Opt Lett* **25**, 820-822 (2000).
88 Faber, D. J., Mik, E. G., Aalders, M. C. & van Leeuwen, T. G. Light absorption of (oxy-)hemoglobin assessed by spectroscopic optical coherence tomography. *Opt Lett* **28**, 1436-1438 (2003).
89 Yi, J., Wei, Q., Liu, W., Backman, V. & Zhang, H. F. Visible-light optical coherence tomography for retinal oximetry. *Opt Lett* **38**, 1796-1798 (2013).
90 Yi, J., Chen, S., Backman, V. & Zhang, H. F. In vivo functional microangiography by visible-light optical coherence tomography. *Biomed Opt Express* **5**, 3603-3612 (2014).
91 Goodman, J. W. *Statistical optics*. (John Wiley & Sons, 2015).
92 Kim, D. Y. *et al.* Optical imaging of the chorioretinal vasculature in the living human eye. *Proceedings of the National Academy of Sciences* **110**, 14354-14359 (2013).
93 Jia, Y. *et al.* Quantitative optical coherence tomography angiography of vascular abnormalities in the living human eye. *Proceedings of the National Academy of Sciences* **112**, E2395-E2402 (2015).
94 Tan, A. C. *et al.* An overview of the clinical applications of optical coherence tomography angiography. *Eye* **32**, 262 (2018).
95 Kashani, A. H. *et al.* Optical coherence tomography angiography: A comprehensive review of current methods and clinical applications. *Progress in retinal and eye research* **60**, 66-100 (2017).
96 Tam, J., Tiruveedhula, P. & Roorda, A. Characterization of single-file flow through human retinal parafoveal capillaries using an adaptive optics scanning laser ophthalmoscope. *Biomedical optics express* **2**, 781-793 (2011).
97 Spaide, R. F., Klancnik, J. M. & Cooney, M. J. Retinal vascular layers imaged by fluorescein angiography and optical coherence tomography angiography. *JAMA ophthalmology* **133**, 45-50 (2015).
98 An, D. *et al.* Quantitative comparisons between optical coherence tomography angiography and matched histology in the human eye. *Experimental eye research* **170**, 13-19 (2018).
99 Cimalla, P., Walther, J., Mittasch, M. & Koch, E. Shear flow-induced optical inhomogeneity of blood assessed in vivo and in vitro by spectral domain optical coherence tomography in the 1.3 μm wavelength range. *Journal of Biomedical Optics* **16**, 116020-11602011 (2011).
100 Muraoka, Y. *et al.* Morphologic and functional changes in retinal vessels associated with branch retinal vein occlusion. *Ophthalmology* **120**, 91-99 (2013).
101 Duncan, D. D. & Kirkpatrick, S. J. Can laser speckle flowmetry be made a quantitative tool? *Journal of the Optical Society of America. A, Optics, image science, and vision* **25**, 2088-2094 (2008).
102 Fedosov, D. A., Noguchi, H. & Gompper, G. Multiscale modeling of blood flow: from single cells to blood rheology. *Biomechanics and modeling in mechanobiology* **13**, 239-258 (2014).
103 Secomb, T. W. Blood flow in the microcirculation. *Annual Review of Fluid Mechanics* **49**, 443-461 (2017).
104 Fung, Y.-c. *Biomechanics: motion, flow, stress, and growth*. (Springer Science & Business Media, 2013).
105 Choi, W. *et al.* Choriocapillaris and choroidal microvasculature imaging with ultrahigh speed OCT angiography. *PLoS One* **8**, e81499 (2013).
106 Jia, Y. *et al.* Quantitative optical coherence tomography angiography of choroidal neovascularization in age-related macular degeneration. *Ophthalmology* **121**, 1435-1444 (2014).
107 Jia, Y. *et al.* Quantitative optical coherence tomography angiography of vascular abnormalities in the living human eye. *Proc Natl Acad Sci U S A* **112**, E2395-2402 (2015).
108 Ishibazawa, A. *et al.* Optical Coherence Tomography Angiography in Diabetic Retinopathy: A Prospective Pilot Study. *Am J Ophthalmol* **160**, 35-44 e31 (2015).
109 Jia, Y. *et al.* Optical coherence tomography angiography of optic disc perfusion in glaucoma. *Ophthalmology* **121**, 1322-1332 (2014).

110 Spaide, R. F. Optical Coherence Tomography Angiography Signs of Vascular Abnormalization With Antiangiogenic Therapy for Choroidal Neovascularization. *Am J Ophthalmol* **160**, 6-16 (2015).
111 Talisa, E. *et al.* Spectral-domain optical coherence tomography angiography of choroidal neovascularization. *Ophthalmology* **122**, 1228-1238 (2015).
112 Tsai, T. H. *et al.* Endoscopic optical coherence angiography enables 3-dimensional visualization of subsurface microvasculature. *Gastroenterology* **147**, 1219-1221 (2014).
113 Lee, H. C. *et al.* Circumferential optical coherence tomography angiography imaging of the swine esophagus using a micromotor balloon catheter. *Biomed Opt Express* **7**, 2927-2942 (2016).
114 Jung, Y., Zhi, Z. & Wang, R. K. Three-dimensional optical imaging of microvascular networks within intact lymph node in vivo. *Journal of biomedical optics* **15**, 050501-050501-050503 (2010).
115 Srinivasan, V. J. *et al.* Optical coherence tomography for the quantitative study of cerebrovascular physiology. *J Cereb Blood Flow Metab* **31**, 1339-1345 (2011).
116 Kleinfeld, D., Mitra, P. P., Helmchen, F. & Denk, W. Fluctuations and stimulus-induced changes in blood flow observed in individual capillaries in layers 2 through 4 of rat neocortex. *Proc Natl Acad Sci U S A* **95**, 15741-15746 (1998).
117 Kamoun, W. S. *et al.* Simultaneous measurement of RBC velocity, flux, hematocrit and shear rate in vascular networks. *Nature methods* **7**, 655-660 (2010).
118 Santisakultarm, T. P. *et al.* In vivo two-photon excited fluorescence microscopy reveals cardiac- and respiration-dependent pulsatile blood flow in cortical blood vessels in mice. *American Journal of Physiology - Heart and Circulatory Physiology* **302**, H1367-H1377 (2012).
119 Desjardins, C. & Duling, B. R. Microvessel hematocrit: measurement and implications for capillary oxygen transport. *American Journal of Physiology - Heart and Circulatory Physiology* **252**, H494-H503 (1987).
120 Santisakultarm, T. P. *et al.* In vivo two-photon excited fluorescence microscopy reveals cardiac- and respiration-dependent pulsatile blood flow in cortical blood vessels in mice. *American Journal of Physiology-Heart and Circulatory Physiology* **302**, H1367-H1377 (2012).
121 Faber, D. J. *et al.* Oxygen saturation-dependent absorption and scattering of blood. *Physical review letters* **93**, 028102 (2004).
122 Meinke, M., Müller, G., Helfmann, J. & Friebel, M. Optical properties of platelets and blood plasma and their influence on the optical behavior of whole blood in the visible to near infrared wavelength range. *Journal of biomedical optics* **12**, 014024-014024-014029 (2007).
123 Sydoruk, O., Zhernovaya, O., Tuchin, V. & Douplik, A. Refractive index of solutions of human hemoglobin from the near-infrared to the ultraviolet range: Kramers-Kronig analysis. *Journal of biomedical optics* **17**, 115002-115002 (2012).
124 Bosschaart, N., Edelman, G. J., Aalders, M. C., van Leeuwen, T. G. & Faber, D. J. A literature review and novel theoretical approach on the optical properties of whole blood. *Lasers in medical science* **29**, 453-479 (2014).
125 Yaroslavsky, A. N., Yaroslavsky, I. V., Goldbach, T. & Schwarzmaier, H.-J. in *Photonics West'96.* 314-324 (International Society for Optics and Photonics).
126 Simon, J.-C. Dependent scattering and radiative transfer in dense inhomogeneous media. *Physica A: Statistical Mechanics and its Applications* **241**, 77-81 (1997).
127 Roggan, A., Friebel, M., Dörschel, K., Hahn, A. & Muller, G. Optical properties of circulating human blood in the wavelength range 400-2500 nm. *Journal of biomedical optics* **4**, 36-46 (1999).
128 Friebel, M., Roggan, A., Müller, G. & Meinke, M. Determination of optical properties of human blood in the spectral range 250 to 1100 nm using Monte Carlo simulations with hematocrit-dependent effective scattering phase functions. *Journal of biomedical optics* **11**, 034021-034021-034010 (2006).
129 Meinke, M., Müller, G., Helfmann, J. & Friebel, M. Empirical model functions to calculate hematocrit-dependent optical properties of human blood. *Applied optics* **46**, 1742-1753 (2007).

130 Henyey, L. G. & Greenstein, J. L. Diffuse radiation in the galaxy. *The Astrophysical Journal* **93**, 70-83 (1941).
131 Hammer, M., Yaroslavsky, A. N. & Schweitzer, D. A scattering phase function for blood with physiological haematocrit. *Physics in medicine and biology* **46**, N65 (2001).
132 Friebel, M., Helfmann, J., Müller, G. & Meinke, M. Influence of shear rate on the optical properties of human blood in the spectral range 250 to 1100nm. *Journal of biomedical optics* **12**, 054005-054005-054008 (2007).
133 Prati, F. *et al.* Expert review document on methodology, terminology, and clinical applications of optical coherence tomography: physical principles, methodology of image acquisition, and clinical application for assessment of coronary arteries and atherosclerosis. *European heart journal* **31**, 401-415 (2010).
134 Bigio, I. J. & Fantini, S. *Quantitative Biomedical Optics: Theory, Methods, and Applications*. (Cambridge University Press, 2016).
135 Chen, C.-L. & Wang, R. K. Optical coherence tomography based angiography [Invited]. *Biomedical Optics Express* **8**, 1056 (2017).
136 de Carlo, T. E., Romano, A., Waheed, N. K. & Duker, J. S. A review of optical coherence tomography angiography (OCTA). *Int J Retina Vitreous* **1**, 5 (2015).
137 Siegert, A. MIT Rad Lab Rep No 465. *Massachusetts Institute of Technology, Cambridge, MA* (1943).
138 Srinivasan, V. J., Chan, A. C. & Lam, E. Y. *Doppler OCT and OCT angiography for in vivo imaging of vascular physiology*. (INTECH Open Access Publisher, 2012).
139 Leitgeb, R. A., Werkmeister, R. M., Blatter, C. & Schmetterer, L. Doppler optical coherence tomography. *Progress in retinal and eye research* **41**, 26-43 (2014).
140 Schmitt, J. M., Xiang, S. & Yung, K. M. Speckle in optical coherence tomography. *Journal of biomedical optics* **4**, 95-105 (1999).
141 Barton, J. K. & Stromski, S. Flow measurement without phase information in optical coherence tomography images. *Optics express* **13**, 5234-5239 (2005).
142 Mariampillai, A. *et al.* Speckle variance detection of microvasculature using swept-source optical coherence tomography. *Optics letters* **33**, 1530-1532 (2008).
143 Mariampillai, A. *et al.* Optimized speckle variance OCT imaging of microvasculature. *Optics letters* **35**, 1257-1259 (2010).
144 Enfield, J., Jonathan, E. & Leahy, M. In vivo imaging of the microcirculation of the volar forearm using correlation mapping optical coherence tomography (cmOCT). *Biomedical optics express* **2**, 1184-1193 (2011).
145 Jia, Y. *et al.* Split-spectrum amplitude-decorrelation angiography with optical coherence tomography. *Optics express* **20**, 4710-4725 (2012).
146 Leitgeb, R. A. *et al.* Real-time assessment of retinal blood flow with ultrafast acquisition by color Doppler Fourier domain optical coherence tomography. *Optics Express* **11**, 3116-3121 (2003).
147 Leitgeb, R. A. *et al.* Real-time measurement of in vitro flow by Fourier-domain color Doppler optical coherence tomography. *Optics letters* **29**, 171-173 (2004).
148 Zhao, Y. *et al.* Doppler standard deviation imaging for clinical monitoring of in vivo human skin blood flow. *Optics Letters* **25**, 1358-1360 (2000).
149 Makita, S., Hong, Y., Yamanari, M., Yatagai, T. & Yasuno, Y. Optical coherence angiography. *Optics Express* **14**, 7821-7840 (2006).
150 Park, B. H. *et al.* Real-time fiber-based multi-functional spectral-domain optical coherence tomography at 1.3 μm. *Optics Express* **13**, 3931-3944 (2005).
151 Fingler, J., Schwartz, D., Yang, C. & Fraser, S. E. Mobility and transverse flow visualization using phase variance contrast with spectral domain optical coherence tomography. *Optics express* **15**, 12636-12653 (2007).
152 Kim, D. Y. *et al.* In vivo volumetric imaging of human retinal circulation with phase-variance optical coherence tomography. *Biomedical optics express* **2**, 1504-1513 (2011).

153 Lee, J., Srinivasan, V., Radhakrishnan, H. & Boas, D. A. Motion correction for phase-resolved dynamic optical coherence tomography imaging of rodent cerebral cortex. *Optics express* **19**, 21258-21270 (2011).
154 Zhang, A., Zhang, Q., Chen, C.-L. & Wang, R. K. Methods and algorithms for optical coherence tomography-based angiography: a review and comparison. *Journal of biomedical optics* **20**, 100901-100901 (2015).
155 An, L., Qin, J. & Wang, R. K. Ultrahigh sensitive optical microangiography for in vivo imaging of microcirculations within human skin tissue beds. *Optics express* **18**, 8220-8228 (2010).
156 Nam, A. S., Chico-Calero, I. & Vakoc, B. J. Complex differential variance algorithm for optical coherence tomography angiography. *Biomedical optics express* **5**, 3822-3832 (2014).
157 Wei, W. *et al.* Intervolume analysis to achieve four-dimensional optical microangiography for observation of dynamic blood flow. *J Biomed Opt* **21**, 36005 (2016).
158 Klein, T. *et al.* Multi-MHz retinal OCT. *Biomedical optics express* **4**, 1890-1908 (2013).
159 Choi, W. J. *et al.* Characterizing relationship between optical microangiography signals and capillary flow using microfluidic channels. *Biomed Opt Express* **7**, 2709-2728 (2016).
160 Kinnunen, M. & Myllylä, R. Effect of glucose on photoacoustic signals at the wavelengths of 1064 and 532 nm in pig blood and intralipid. *Journal of Physics D: Applied Physics* **38**, 2654 (2005).
161 Van Staveren, H. J., Moes, C. J., van Marie, J., Prahl, S. A. & Van Gemert, M. J. Light scattering in lntralipid-10% in the wavelength range of 400–1100 nm. *Applied optics* **30**, 4507-4514 (1991).
162 Su, J. P. *et al.* Calibration of optical coherence tomography angiography with a microfluidic chip. *J Biomed Opt* **21**, 86015 (2016).
163 Denk, W., Strickler, J. H. & Webb, W. W. Two-photon laser scanning fluorescence microscopy. *Science* **248**, 73-76 (1990).
164 Zipfel, W. R., Williams, R. M. & Webb, W. W. Nonlinear magic: multiphoton microscopy in the biosciences. *Nature biotechnology* **21**, 1369-1377 (2003).
165 Wang, H. *et al.* Does optical microangiography provide accurate imaging of capillary vessels?: validation using multiphoton microscopy. *Journal of biomedical optics* **19**, 106011-106011 (2014).
166 Ren, H., Du, C., Park, K., Volkow, N. D. & Pan, Y. Quantitative imaging of red blood cell velocity invivo using optical coherence Doppler tomography. *Appl Phys Lett* **100**, 233702-2337024 (2012).
167 Ren, H. *et al.* Cocaine-induced cortical microischemia in the rodent brain: clinical implications. *Mol Psychiatry* **17**, 1017-1025 (2012).
168 Chan, A. C., Merkle, C. W., Lam, E. Y. & Srinivasan, V. J. in *SPIE BiOS.* 89342J-89342J-89349 (International Society for Optics and Photonics).
169 Choi, W. *et al.* Ultrahigh-Speed, Swept-Source Optical Coherence Tomography Angiography in Nonexudative Age-Related Macular Degeneration with Geographic Atrophy. *Ophthalmology* **122**, 2532-2544 (2015).
170 Ploner, S. B. *et al.* TOWARD QUANTITATIVE OPTICAL COHERENCE TOMOGRAPHY ANGIOGRAPHY: Visualizing Blood Flow Speeds in Ocular Pathology Using Variable Interscan Time Analysis. *Retina* **36**, S118-S126 (2016).
171 Bonner, R. & Nossal, R. Model for laser Doppler measurements of blood flow in tissue. *Applied optics* **20**, 2097-2107 (1981).
172 Faber, D. J., van der Meer, F. J., Aalders, M. C. & van Leeuwen, T. G. in *Saratov Fall Meeting 2005: Optical Technologies in Biophysics and Medicine VII.* 61630Y-61630Y-61639 (International Society for Optics and Photonics).
173 Faber, D. J. & van Leeuwen, T. G. Are quantitative attenuation measurements of blood by optical coherence tomography feasible? *Opt Lett* **34**, 1435-1437 (2009).
174 Srinivasan, V. J. & Radhakrishnan, H. Optical Coherence Tomography angiography reveals laminar microvascular hemodynamics in the rat somatosensory cortex during activation. *NeuroImage* **102**, 393-406 (2014).

175 Tokayer, J., Jia, Y., Dhalla, A.-H. & Huang, D. Blood flow velocity quantification using split-spectrum amplitude-decorrelation angiography with optical coherence tomography. *Biomedical optics express* **4**, 1909-1924 (2013).
176 Choi, W. J., Li, Y., Qin, W. & Wang, R. K. Cerebral capillary velocimetry based on temporal OCT speckle contrast. *Biomedical Optics Express* **7**, 4859-4873 (2016).
177 Hartinger, A. E., Nam, A. S., Chico-Calero, I. & Vakoc, B. J. Monte Carlo modeling of angiographic optical coherence tomography. *Biomedical optics express* **5**, 4338-4349 (2014).
178 Pan, Y., You, J., Volkow, N. D., Park, K. & Du, C. Ultrasensitive detection of 3D cerebral microvascular network dynamics in vivo. *Neuroimage* **103**, 492-501 (2014).
179 Merkle, C. W. & Srinivasan, V. J. Laminar microvascular transit time distribution in the mouse somatosensory cortex revealed by Dynamic Contrast Optical Coherence Tomography. *Neuroimage* **125**, 350-362 (2016).
180 Assadi, H., Demidov, V., Karshafian, R., Douplik, A. & Vitkin, I. A. Microvascular contrast enhancement in optical coherence tomography using microbubbles. *Journal of Biomedical Optics* **21**, 076014-076014 (2016).
181 Barton, J. K., Hoying, J. B. & Sullivan, C. J. Use of microbubbles as an optical coherence tomography contrast agent. *Academic radiology* **9**, S52-S55 (2002).
182 Frangi, A. F., Niessen, W. J., Vincken, K. L. & Viergever, M. A. in *International conference on medical image computing and computer-assisted intervention.* 130-137 (Springer, 1998).
183 Leahy, C., Radhakrishnan, H., Weiner, G., Goldberg, J. L. & Srinivasan, V. J. Mapping the 3D connectivity of the rat inner retinal vascular network using OCT angiography. *Investigative ophthalmology & visual science* **56**, 5785-5793 (2015).
184 Zhou, W., Kholiqov, O., Chong, S. P. & Srinivasan, V. J. Highly parallel, interferometric diffusing wave spectroscopy for monitoring cerebral blood flow dynamics. *Optica* **5**, 518-527 (2018).
185 Secomb, T. W., Hsu, R. & Pries, A. Motion of red blood cells in a capillary with an endothelial surface layer: effect of flow velocity. *American Journal of Physiology-Heart and Circulatory Physiology* **281**, H629-H636 (2001).
186 Chaigneau, E., Oheim, M., Audinat, E. & Charpak, S. Two-photon imaging of capillary blood flow in olfactory bulb glomeruli. *Proceedings of the National Academy of Sciences* **100**, 13081-13086 (2003).
187 Li, B. *et al.* More homogeneous capillary flow and oxygenation in deeper cortical layers correlate with increased oxygen extraction. *Elife* **8** (2019).
188 Gorczynska, I., Migacz, J. V., Zawadzki, R. J., Capps, A. G. & Werner, J. S. Comparison of amplitude-decorrelation, speckle-variance and phase-variance OCT angiography methods for imaging the human retina and choroid. *Biomed Opt Express* **7**, 911-942 (2016).
189 Wax, A. & Backman, V. *Biomedical applications of light scattering*. (McGraw Hill Professional, 2010).
190 Zhou, K. C., Qian, R., Degan, S., Farsiu, S. & Izatt, J. A. Optical coherence refraction tomography. *Nature Photonics* **13**, 794-802 (2019).
191 Merkle, C. W., Zhu, J., Bernucci, M. T. & Srinivasan, V. J. Dynamic Contrast Optical Coherence Tomography reveals laminar microvascular hemodynamics in the mouse neocortex in vivo. *NeuroImage* **202**, 116067 (2019).
192 Meyer-Luehmann, M. *et al.* Rapid appearance and local toxicity of amyloid-β plaques in a mouse model of Alzheimer's disease. *Nature* **451**, 720 (2008).
193 Meyer, E. P., Ulmann-Schuler, A., Staufenbiel, M. & Krucker, T. Altered morphology and 3D architecture of brain vasculature in a mouse model for Alzheimer's disease. *Proceedings of the national academy of sciences* **105**, 3587-3592 (2008).
194 Jack Jr, C. R. *et al.* Hypothetical model of dynamic biomarkers of the Alzheimer's pathological cascade. *The Lancet Neurology* **9**, 119-128 (2010).
195 Jack Jr, C. R. *et al.* 11C PiB and structural MRI provide complementary information in imaging of Alzheimer's disease and amnestic mild cognitive impairment. *Brain* **131**, 665-680 (2008).

196 Yang, Y. *et al.* A prototype high-resolution small-animal PET scanner dedicated to mouse brain imaging. *Journal of Nuclear Medicine* **57**, 1130-1135 (2016).
197 Kim, K. *et al.* A novel depth-of-interaction rebinning strategy for ultrahigh resolution PET. *Physics in Medicine & Biology* **63**, 165011 (2018).
198 Badea, A. *et al.* The fornix provides multiple biomarkers to characterize circuit disruption in a mouse model of Alzheimer's disease. *Neuroimage* **142**, 498-511 (2016).
199 Fuhrmann, M. *et al.* Microglial Cx3cr1 knockout prevents neuron loss in a mouse model of Alzheimer's disease. *Nature neuroscience* **13**, 411 (2010).
200 Takasaki, K., Abbasi-Asl, R. & Waters, J. Superficial bound of the depth limit of Two-Photon imaging in mouse brain. *Eneuro* **7** (2020).
201 Wang, T. & Xu, C. Three-photon neuronal imaging in deep mouse brain. *Optica* **7**, 947-960 (2020).
202 Horton, N. G. *et al.* In vivo three-photon microscopy of subcortical structures within an intact mouse brain. *Nature photonics* **7**, 205 (2013).
203 Wang, T. *et al.* Three-photon imaging of mouse brain structure and function through the intact skull. *Nature methods* **15**, 789 (2018).
204 Yang, G., Pan, F., Parkhurst, C. N., Grutzendler, J. & Gan, W.-B. Thinned-skull cranial window technique for long-term imaging of the cortex in live mice. *Nature protocols* **5**, 201 (2010).
205 Drew, P. J. *et al.* Chronic optical access through a polished and reinforced thinned skull. *Nature methods* **7**, 981-984 (2010).
206 Xia, F. *et al.* In vivo label-free confocal imaging of the deep mouse brain with long-wavelength illumination. *Biomedical optics express* **9**, 6545-6555 (2018).
207 Nishizawa, N. & Takayanagi, J. Octave spanning high-quality supercontinuum generation in all-fiber system. *JOSA B* **24**, 1786-1792 (2007).
208 Ouzounov, D. G. *et al.* In vivo three-photon imaging of activity of GCaMP6-labeled neurons deep in intact mouse brain. *Nature methods* **14**, 388-390 (2017).
209 Redlich, M. J. & Lim, H. A method to measure myeloarchitecture of the murine cerebral cortex in vivo and ex vivo by intrinsic third-harmonic generation. *Frontiers in neuroanatomy* **13**, 65 (2019).
210 Schain, A. J., Hill, R. A. & Grutzendler, J. Label-free in vivo imaging of myelinated axons in health and disease with spectral confocal reflectance microscopy. *Nature medicine* **20**, 443-449 (2014).
211 Bolmont, T. *et al.* Label-free imaging of cerebral β-amyloidosis with extended-focus optical coherence microscopy. *Journal of Neuroscience* **32**, 14548-14556 (2012).
212 Marks, D. L., Oldenburg, A. L., Reynolds, J. J. & Boppart, S. A. Digital algorithm for dispersion correction in optical coherence tomography for homogeneous and stratified media. *Applied optics* **42**, 204-217 (2003).
213 Agrawal, H., Davis, J. & Himwich, W. Developmental changes in mouse brain: weight, water content and free amino acids. *Journal of neurochemistry* **15**, 917-923 (1968).
214 Kedenburg, S., Vieweg, M., Gissibl, T. & Giessen, H. Linear refractive index and absorption measurements of nonlinear optical liquids in the visible and near-infrared spectral region. *Optical Materials Express* **2**, 1588-1611 (2012).
215 Hale, G. M. & Querry, M. R. Optical constants of water in the 200-nm to 200-μm wavelength region. *Applied optics* **12**, 555-563 (1973).
216 Max, J.-J. & Chapados, C. Isotope effects in liquid water by infrared spectroscopy. III. H2O and D2O spectra from 6000 to 0 cm−1. *The Journal of chemical physics* **131**, 184505 (2009).
217 Yasuno, Y. *et al.* In vivo high-contrast imaging of deep posterior eye by 1-μm swept source optical coherence tomography and scattering optical coherence angiography. *Optics express* **15**, 6121-6139 (2007).
218 Tsai, P. S. *et al.* Correlations of neuronal and microvascular densities in murine cortex revealed by direct counting and colocalization of nuclei and vessels. *Journal of Neuroscience* **29**, 14553-14570 (2009).

219 Leahy, C., Radhakrishnan, H. & Srinivasan, V. J. Volumetric imaging and quantification of cytoarchitecture and myeloarchitecture with intrinsic scattering contrast. *Biomedical optics express* **4**, 1978-1990 (2013).
220 Wang, M. *et al.* Comparing the effective attenuation lengths for long wavelength in vivo imaging of the mouse brain. *Biomedical optics express* **9**, 3534-3543 (2018).
221 Li, X., Gao, J., Ding, J., Hu, G. & Xiao, M. Aquaporin-4 expression contributes to decreases in brain water content during mouse postnatal development. *Brain research bulletin* **94**, 49-55 (2013).
222 Matthieu, J.-M., Widmer, S. & Herschkowitz, N. Biochemical changes in mouse brain composition during myelination. *Brain research* **55**, 391-402 (1973).
223 Oakley, H. *et al.* Intraneuronal β-amyloid aggregates, neurodegeneration, and neuron loss in transgenic mice with five familial Alzheimer's disease mutations: potential factors in amyloid plaque formation. *Journal of Neuroscience* **26**, 10129-10140 (2006).
224 Ohno, M. *et al.* BACE1 gene deletion prevents neuron loss and memory deficits in 5XFAD APP/PS1 transgenic mice. *Neurobiology of disease* **26**, 134-145 (2007).
225 Spires, T. L. *et al.* Dendritic spine abnormalities in amyloid precursor protein transgenic mice demonstrated by gene transfer and intravital multiphoton microscopy. *Journal of Neuroscience* **25**, 7278-7287 (2005).
226 Gu, L. *et al.* Myelin changes at the early stage of 5XFAD mice. *Brain research bulletin* **137**, 285-293 (2018).
227 Papuć, E. & Rejdak, K. The role of myelin damage in Alzheimer's disease pathology. *Archives of Medical Science: AMS* **16**, 345 (2020).
228 Conchello, J.-A. & Lichtman, J. W. Optical sectioning microscopy. *Nature methods* **2**, 920-931 (2005).
229 Sheppard, C. J. & Shotton, D. M. *Confocal laser scanning microscopy*. (1997).
230 Zhu, D., Larin, K. V., Luo, Q. & Tuchin, V. V. Recent progress in tissue optical clearing. *Laser & photonics reviews* **7**, 732-757 (2013).
231 White, D., Widdowson, E., Woodard, H. & Dickerson, J. The composition of body tissues.(II) Fetus to young adult. *The British journal of radiology* **64**, 149-159 (1991).
232 Faber, D. J., Van Der Meer, F. J., Aalders, M. C. & van Leeuwen, T. G. Quantitative measurement of attenuation coefficients of weakly scattering media using optical coherence tomography. *Optics express* **12**, 4353-4365 (2004).
233 Aernouts, B. *et al.* Supercontinuum laser based optical characterization of Intralipid® phantoms in the 500-2250 nm range. *Optics express* **21**, 32450-32467 (2013).
234 Islam, M. N. Near-infrared super-continuum lasers for early detection of breast and other cancers. U.S. patent U.S. patent 9,993,159 (2018).
235 Kuo, W.-C., Lai, C.-M., Huang, Y.-S., Chang, C.-Y. & Kuo, Y.-M. Balanced detection for spectral domain optical coherence tomography. *Optics express* **21**, 19280-19291 (2013).
236 Kho, A. M. & Srinivasan, V. J. Proactive spectrometer matching for excess noise suppression in balanced visible light optical coherence tomography (OCT). *Optics Express* **29**, 42037-42054 (2021).
237 Marchand, P. J. *et al.* Imaging of cortical structures and microvasculature using extended-focus optical coherence tomography at 1.3 μm. *Optics letters* **43**, 1782-1785 (2018).
238 Stremplewski, P. *et al.* In vivo volumetric imaging by crosstalk-free full-field OCT. *Optica* **6**, 608-617 (2019).
239 Ates, O. *et al.* Neuroprotection by resveratrol against traumatic brain injury in rats. *Molecular and cellular biochemistry* **294**, 137-144 (2007).
240 Cheng, J. *et al.* Development of a rat model for studying blast-induced traumatic brain injury. *Journal of the neurological sciences* **294**, 23-28 (2010).
241 Si, P. *et al.* Gold nanobipyramids as second near infrared optical coherence tomography contrast agents for in vivo multiplexing studies. *Nano letters* **20**, 101-108 (2019).

242 Keahey, P. *et al.* Spectral-and Polarization-Dependent Scattering of Gold Nanobipyramids for Exogenous Contrast in Optical Coherence Tomography. *Nano Letters* (2021).
243 Wu, M., Small, D. M., Nishimura, N. & Adie, S. G. Computed optical coherence microscopy of mouse brain ex vivo. *Journal of biomedical optics* **24**, 116002 (2019).
244 Liu, S. *et al.* Closed-loop wavefront sensing and correction in the mouse brain with computed optical coherence microscopy. *Biomedical Optics Express* **12**, 4934-4954 (2021).
245 Xu, D., Huang, Y. & Kang, J. U. Compressive sensing with dispersion compensation on non-linear wavenumber sampled spectral domain optical coherence tomography. *Biomedical Optics Express* **4**, 1519-1532 (2013).
246 Lagarias, J. C., Reeds, J. A., Wright, M. H. & Wright, P. E. Convergence properties of the Nelder--Mead simplex method in low dimensions. *SIAM Journal on optimization* **9**, 112-147 (1998).
247 Zhang, T., Kho, A. M. & Srinivasan, V. J. Water wavenumber calibration for visible light optical coherence tomography. *Journal of Biomedical Optics* **25**, 090501 (2020).
248 Morrison, J. H., Grzanna, R., Molliver, M. E. & Coyle, J. T. The distribution and orientation of noradrenergic fibers in neocortex of the rat: an immunofluorescence study. *Journal of Comparative Neurology* **181**, 17-39 (1978).
249 Gesperger, J. *et al.* Comparison of intensity-and polarization-based contrast in amyloid-beta plaques as observed by optical coherence tomography. *Applied Sciences* **9**, 2100 (2019).
250 Lichtenegger, A. *et al.* Ex-vivo Alzheimer's disease brain tissue investigation: a multiscale approach using 1060-nm swept source optical coherence tomography for a direct correlation to histology. *Neurophotonics* **7**, 035004 (2020).